Dressed states
of a strain-driven spin in diamond

Inauguraldissertation

zur

Erlangung der Würde eines Doktors der Philosophie
vorgelegt der
Philosophisch-Naturwissenschaftlichen Fakultät
der Universität Basel

von

Johannes Kölbl

aus Altusried, Deutschland

Basel, 2020

b

Genehmigt von der Philosophisch-Naturwissenschaftlichen Fakultät
auf Antrag von
Prof. Dr. Patrick Maletinsky
Prof. Dr. Guido Burkard

Basel, den 17.03.2020

                                                    Prof. Dr. Martin Spiess
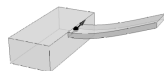   Dekan

Abstract

Emerging quantum technologies, such as quantum information processing and quantum metrology, require quantum systems that provide reliable toolsets for initialization, readout, and coherent manipulation as well as long coherence times. The coherence of these systems, however, is usually limited by uncontrolled interactions with the surrounding environment. In particular, innovations building on solid-state spin systems like the Nitrogen-Vacancy (NV) center in diamond ordinarily involve the use of magnetic field-sensitive states. In this case, ambient magnetic field fluctuations constitute a serious impediment that shortens the coherence time considerably. Thus, the protection of individual quantum systems from environmental perturbations constitutes a fundamentally important but also a challenging task for the further development of quantum appliances.

In this thesis, we address this challenge by extending the widely used approach of dynamical decoupling to protect a quantum system from decoherence. Specifically, we study three-level dressed states that emerge under continuous, 'closed-contour' interaction driving. To implement and investigate these dressed states, we exploit well-established methods for coherent microwave and strain manipulation of the NV center spin in a hybrid spin-mechanical system. Our results reveal that this novel continuous decoupling mechanism can overcome external magnetic fluctuations in a robust way. We demonstrate experimentally that the dressed states we created are long-lived and find coherence times nearly two orders of magnitude longer than the inhomogeneous dephasing time of the NV spin, even for moderate driving strengths.

To realize direct and efficient access to the coherence-protected dressed states under closed-contour driving, we further demonstrate the use of state transfer protocols for their initialization and readout. In addition to an adiabatic approach, we apply recently developed protocols based on 'shortcuts to adiabaticity' to accomplish the initialization process, which ultimately accelerates the transfer speed by a factor of 2.6 compared to the fastest adiabatic protocol with similar fidelity. Moreover, we show bidirectionality of the accelerated state transfer, which allows us to directly read out the dressed state population and to quantify the transfer fidelity of $\approx 99\,\%$.
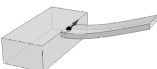
By employing the methods to prepare and read out the dressed states, we lay the foundation to meet the remaining key requirement for quantum systems – coherent quantum control. We present direct, coherent manipulation of the dressed states in their own manifold and exploit this for extensive characterization of the dressed states' properties. Thus, our results constitute an elementary step to establish the dressed states as a powerful resource in prospective quantum sensing applications.

Harnessing quantum systems like the dressed states as nanoscale sensors of external fields requires the detailed characterization of the local internal environment. In the final part of this thesis, we report on the determination of intrinsic effective fields of individual NV center spins. We study single NVs in high purity diamond and find that local strain dominates over local electric fields. In addition, we experimentally demonstrate and theoretically describe a new technique for performing single spin-based polarization analysis of microwave fields in a tunable, linear basis.

Contents

List of symbols and abbreviations

General symbols

t	Time
τ	Evolution time
T	Environmental temperature
S, I, $I^{(C)}$	Total electron and nuclear spin
m_s, m_I, $m_I^{(C)}$	Electron and nuclear spin quantum number
I_{Laser}	Laser intensity/laser pulse sequence

NV center

^{12}C, ^{13}C	Carbon isotopes
^{14}N	Nitrogen isotope
x, y, z	NV coordinates
X, Y, Z	Crystal coordinates
C_{3v}	Symmetry point group of the NV center
A_1, E	$S = 1$ ground state symmetries
$^3A_2$, ^3E	$S = 1$ ground and excited state manifolds
$^1A_1$, $^1E_{1,2}$	$S = 0$ ground state manifold
D_0	Zero-field splitting
P	Nuclear electric quadrupole parameter
A_{HF}, $A_{\text{HF}}^{\parallel}$, $A_{\text{HF}}^{\perp}$	Axial and transverse hyperfine parameters
$\underline{\mathbf{A}}$	^{13}C hyperfine tensor
A_{ij} with $i,j = x,y,z$	^{13}C hyperfine coupling constants
$A_{\text{HF}}^{(C)}$	Axial ^{13}C hyperfine coupling strength
T_1	Spin relaxation time
T_2^*	Spin dephasing time
T_2	Spin coherence time
T_{Rabi}	Rabi decay time
Γ, γ, Υ	Relaxation rates
$S_{i,j}$ with $i,j = 0,\pm 1$	Signal of relaxation measurement
n	Damping exponent
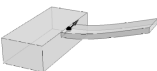
Static external fields

$\boldsymbol{B} = (B_x, B_y, B_z)$	Magnetic field in NV frame
B	Magnetic field amplitude
$B_\parallel$, $B_\perp$	Axial and transverse magnetic field amplitudes
φ_B	Azimuthal angle of transverse magnetic field
f	Flattening parameter
$\boldsymbol{E} = (E_x, E_y, E_z)$	Electric field in NV frame
E	Electric field amplitude
$E_\parallel$, $E_\perp$	Axial and transverse electric field amplitudes
$d_\parallel$, $d_\perp$, $d'_\perp$	Axial and transverse electric field susceptibilities
$\underline{\boldsymbol{\varepsilon}}$, $\underline{\boldsymbol{\sigma}}$	Strain and stress tensor
ε_{ij}, σ_{ij} with $i, j = X, Y, Z$	Strain and stress tensor components
$\sigma_\parallel$, $\sigma_\perp$	Parallel and transverse uniaxial stress amplitudes
$\mathcal{M}_{x,y,z}$, $\mathcal{N}_{x,y}$	Parameters of spin-stress interaction
a_1, a_2, b, c, d, e	Spin-stress coupling strength parameters
$\boldsymbol{\Pi} = (\Pi_x, \Pi_y, \Pi_z)$	Effective field in NV frame
Π	Effective field amplitude
$\Pi_\parallel$, $\Pi_\perp$	Axial and transverse effective field amplitudes
φ_Π	Azimuthal angle of transverse effective field
Δ_Z	Zeeman splitting
Δ_S	Stark splitting
$\Delta^{(C)}$	^{13}C hyperfine splitting
$\Delta_\Pi^{(C)}$	Combined effective field and ^{13}C hyperfine splitting

External manipulation fields

$\boldsymbol{B}^{\mathrm{mw}}(t)$	Time-dependent MW magnetic field
$\boldsymbol{B}^{\mathrm{mw}} = (B_x^{\mathrm{mw}}, B_y^{\mathrm{mw}}, B_z^{\mathrm{mw}})$	MW field amplitude in NV frame
$B_\parallel^{\mathrm{mw}}$, $B_\perp^{\mathrm{mw}}$	Axial and transverse MW field amplitudes
φ_{mw}	Azimuthal angle of transverse MW field
$\Omega_{i,f}$, Ω_{Rabi}	Rabi frequency of spin transition from $|i\rangle$ to $|f\rangle$
$\hat{\boldsymbol{\mu}}$	Magnetic dipole moment operator
$\boldsymbol{\mu}_{i,f} = (\mu_x, \mu_y, \mu_z)$	Magnetic dipole matrix elements
$\mathcal{A}_{i,f}$	Transition strength
$\mathcal{I}$, $\mathcal{I}^{(C)}$, $\mathcal{J}$	Transition imbalances
$\boldsymbol{\mathcal{S}} = (\mathcal{S}_0, \mathcal{S}_1, \mathcal{S}_2, \mathcal{S}_3)$	Stokes vector

ω_{mw}, ω_{man}	MW field frequency
Ω_{mw}, Ω_{man}	MW field amplitude/Rabi frequency
ω_{m}	Mechanical field frequency
Ω_{m}	Mechanical field amplitude/Rabi frequency
ω	Spin transition (angular) frequency
δ	Driving field detuning
$\tau_{\pi/2}$, τ_{π}	Pulse lengths for $\pi/2$- and π-pulses

Closed-contour physics

|	
$\omega_{1,2,3}$	Individual driving field frequency
$\Omega_{1,2,3}$, $\Omega_{1,2}(t)$	Individual driving field amplitude/Rabi frequency
$\delta_{1,2}$	Individual driving field detuning
$\phi_{1,2,3}$	Individual driving field phase
Φ	Total driving field phase (global phase)
Ω	Maximum driving field amplitude/Rabi frequency
φ_0	Constant phase factor
$\Delta_{m,n}$	Spin precession/transition frequency
$T_{m,n}^{\mathrm{dec}}$	Decay time under closed-contour interaction
t_{r}, $t_{\mathrm{r}}^{\mathrm{ad}}$	(Adiabatic) ramp time
t_0	Time-shift of ramp function
ε, ν	Discontinuity and slope parameter of ramp function
$\theta(t)$	Phase of ramp function
t'	Remapping time
N	Number of remapping cycles
$\mathcal{F}$	Transfer fidelity
ω_c	MW carrier frequency
$\omega_{\mathrm{IQ},1}$, $\omega_{\mathrm{IQ},2}$	IQ modulation frequencies
$M_{1,2}$	Multiplication signal
$\sigma_{T_2^*}$	Width of Gaussian noise distribution
$\beta(t)$	Parameter for dressed state correction
$\hat{\Lambda}_j$	Generators of SU(3)
$\varphi_j(t)$	Parametrization variable
$\mathcal{R}(t)$	Normalized shape of ramp function
$N_k(t)$	Normalization factor for instantaneous eigenstates
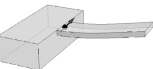
States and operators

$\lvert m_s \rangle$	Ground state fine structure state
$\lvert \pm \rangle$, $\lvert \tilde{\pm} \rangle$	Mixed ground state fine structure states
$\lvert m_s, m_I \rangle$	Ground state hyperfine state
$\lvert m_s, m_I, m_I^{(C)} \rangle$	^{13}C coupled ground state hyperfine state
E_i	Eigenenergy of state $\lvert i \rangle$
$P_{\lvert i \rangle}(t)$	Time-dependent population in state $\lvert i \rangle$
$\lvert \Psi_k \rangle$	Dressed state under closed-contour interaction
E_k	Eigenenergy under closed-contour interaction
$\lvert \xi(t) \rangle$, $\lvert \xi \rangle$	State in $\{\lvert m_s \rangle\}$ and adiabatic frame
$\lvert \psi_k(t) \rangle$, $\lvert \psi_k \rangle$	Adiabatic eigenstate in $\{\lvert m_s \rangle\}$ and adiabatic frame
$\lvert \tilde{\psi}_k \rangle$	Dressed adiabatic eigenstate in dressed frame
$\lvert \psi(t) \rangle$	State after time evolution t
c_j	Weighting factor
$\hat{\mathcal{H}}$	Ground state fine- and hyperfine Hamiltonian
$\hat{\mathcal{H}}_{\mathrm{mag}}$	Magnetic interaction Hamiltonian
$\hat{\mathcal{H}}_{\mathrm{el}}$	Electric interaction Hamiltonian
$\hat{\mathcal{H}}_{\mathrm{el},0}$, $\hat{\mathcal{H}}_{\mathrm{el},1}$, $\hat{\mathcal{H}}_{\mathrm{el},2}$	Components of the electric interaction Hamiltonian
$\hat{\mathcal{H}}_{\sigma}$	Stress interaction Hamiltonian
$\hat{\mathcal{H}}_{\sigma,0}$, $\hat{\mathcal{H}}_{\sigma,1}$, $\hat{\mathcal{H}}_{\sigma,2}$	Components of the stress interaction Hamiltonian
$\hat{\mathcal{H}}_{\mathrm{eff}}$	Effective field interaction Hamiltonian
$\hat{\mathcal{H}}_{\mathrm{HF}}^{(C)}$	^{13}C hyperfine interaction Hamiltonian
$\hat{\mathcal{H}}_{\mathrm{mw}}(t)$	Magnetic dipole interaction Hamiltonian
$\hat{\mathcal{H}}_0$, $\hat{\mathcal{H}}_0(t)$	Closed-contour interaction Hamiltonian
$\hat{\mathcal{H}}_0^{\mathrm{ad}}(t)$	Closed-contour Hamiltonian in adiabatic frame
$\hat{\mathcal{H}}_0^{\mathrm{dr}}(t)$	Closed-contour Hamiltonian in dressed frame
$\hat{\mathcal{H}}_{\mathrm{TD}}(t)$	Transitionless driving correction
$\hat{\mathcal{U}}(t)$	Unitary transformation to adiabatic frame
$\hat{\mathcal{U}}_{\mathrm{dr}}(t)$	Unitary transformation to dressed frame
$\hat{\mathcal{W}}(t)$	Dressed state control Hamiltonian
$W_{1,2}(t)$	Parametrization of control Hamiltonian
$\hat{\boldsymbol{S}} = (\hat{S}_x, \hat{S}_y, \hat{S}_z)$	Dimensionless $S = 1$ spin operators
$\hat{\boldsymbol{I}} = (\hat{I}_x, \hat{I}_y, \hat{I}_z)$	Dimensionless $I = 1$ nuclear spin operators
$\hat{\boldsymbol{I}}^{(C)} = (\hat{I}_x^{(C)}, \hat{I}_y^{(C)}, \hat{I}_z^{(C)})$	Dimensionless $I = 1/2$ nuclear spin operators

Constants

$h = 6.626 \cdot 10^{-34}\,\mathrm{m^2\,kg/s}$	Planck's constant
$\hbar = 1.055 \cdot 10^{-34}\,\mathrm{m^2\,kg/s}$	Reduced Planck's constant
$\mu_B = 9.274 \cdot 10^{-24}\,\mathrm{J/T}$	Bohr magneton
$\mu_N = 5.051 \cdot 10^{-27}\,\mathrm{J/T}$	Nuclear magneton
$g_e = 2.0028$	Isotropic electron g-factor
$g_N = 0.404$	Isotropic $^{14}\mathrm{N}$ nuclear g-factor
$\gamma_{\mathrm{NV}} = 2.80\,\mathrm{MHz/G}$	Gyromagnetic ratio of NV spin
$\gamma_N = 0.308\,\mathrm{kHz/G}$	Gyromagnetic ratio of $^{14}\mathrm{N}$ nuclear spin
$\gamma_C = 1.07\,\mathrm{kHz/G}$	Gyromagnetic ratio of $^{13}\mathrm{C}$ nuclear spin

Abbreviations

|	
AWG	Arbitrary waveform generator
CW	Continuous wave
ESR	Electron spin resonance
H.c.	Hermitian conjugate
Init	Initialization
IR	Infrared
MP	Multiplier
MW	Microwave
NV	Nitrogen-Vacancy
NV$^-$	Negatively charged NV center
Read	Readout
SATD	Superadiabatic transitionless driving
STA	Shortcuts to adiabaticity
STIRAP	Stimulated Raman adiabatic passage
TD	Transitionless driving
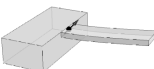
1. Introduction

Quantum physics is a cornerstone of modern natural sciences. Since its foundations were laid in the early 20th century, the quantum formalism has become essential for the understanding and description of systems at atomic length scales and smaller. A pedagogical and widely used abstraction of such complex systems relies on two-level quantum systems. These are the simplest non-trivial quantum models, whose dynamics can be solved analytically without approximation, which renders them an important pillar of quantum theory. Also experimentally, two-level systems have been established as the most common resource for exploring quantum properties, as they offer a large assortment of observable quantum effects, like Rabi oscillations, superposition states, and entanglement, while minimizing experimental challenges. Consequently, such quantum systems have been engineered in diverse host systems, e.g. in quantum dots [1–3], superconducting circuits [4–6], ultracold atoms [7–9], and solid-state spins and defects [10–12].

Three-level quantum systems extend the capabilities of two-level systems, which make them advantageous for various applications, ranging from faster quantum information processing [13–15], the study of entanglement in higher-dimensional systems [16, 17], and more robust quantum cryptography protocols [18, 19]. Typically, experiments studying three-level systems use two separate, coherent driving fields, which couple two different states to a common third one. This configuration gives rise to phenomena inaccessible in two-level systems, including novel population dynamics and coherent state transfer mediated by interference effects of simultaneously driven excitation pathways. Famous examples are Autler-Townes splitting [20], coherent population trapping [21, 22], electromagnetically induced transparency [23], and stimulated Raman adiabatic passage (STIRAP) [24, 25]. The sheer variety of physical effects renders two- and few-level quantum systems highly promising for future quantum technology developments.

Yet decoherence remains a major obstacle for quantum applications. The loss of quantum coherence is caused by the interaction of the system with its environment. In solid-state and atomic systems, ambient magnetic field fluctuations are a serious impediment, usually limiting the coherence time to a small fraction of the spin relaxation time. It is, therefore, imperative to protect a quantum system from these decohering effects while retaining the ability to control the dynamics of the system. There are several approaches to achieve quantum coherence protection. Pulsed dynamical decoupling is a widely used strategy, which has been studied extensively both theoretically [26–30] and experimentally [31–35]. These protocols are based on applying external pulses in a certain sequence to compensate for the effect of the environment, thereby preserving the coherence of the system at certain times. However, pulsed decoupling techniques suffer from pulse imperfections, potentially harmful pulse powers, and high repetition rates and are only severely compatible with desired quantum gate operations. Instead of using a sequence of pulses, continuously driving a two-level
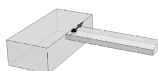
system with a 'dressing' field leads to continuous dynamical decoupling [36–40]. This approach offers another strategy to suppress environmental noise and to protect the system's coherence while being easily combined with quantum gate operations [41–43]. Continuous dynamical decoupling can be extended even further to the more complex concatenated continuous driving [44–47] or combined with the pulsed method to form mixed dynamical decoupling [48].

Three-level systems allow for a similar yet more sophisticated approach. By simultaneously and coherently addressing all three available transitions, a continuous driving scheme known as a 'closed-contour interaction' can be achieved [49]. Such a scheme increases the functionality of three-level systems even further as the three driving fields introduce complex interference dynamics. Additionally, the continuous closed-contour driving generates dressed states, i.e. the eigenstates of the driven system, that might provide a novel mechanism for efficient coherence protection beyond what is offered by driven two-level systems.

The Nitrogen-Vacancy (NV) center's electronic spin naturally provides a three-level system to implement and test such schemes [50]. Due to its fast response to resonant spin manipulation [51, 52], its long coherence time [53, 54], its room-temperature operation, and the host of well-established methods for optical spin initialization and readout [55, 56], the NV spin constitutes an attractive and powerful solid-state platform in quantum science. However, the long spin coherence time is usually diminished by unwanted magnetic interactions with the surrounding spin-bath inherent in the diamond lattice, making the full coherence potential not immediately accessible. Thus, to fully exploit the merits of the NV spin, it is crucial to decouple it from its magnetic environment. In this context, closed-contour dynamical decoupling in combination with full coherent quantum control of the dressed states may boost the NV's impact in quantum technologies even further and may pave the way for future applications.

Scope of this thesis

In this thesis, we report on the implementation and detailed characterization of the three-level dressed states emerging under closed-contour driving of the NV center's spin ground state. The major goals of our study are thereby to provide a thorough understanding of this novel type of dressed states and to lay the foundation for prospective operations in quantum sensing and quantum information processing.

We start with a theoretical description of the main aspects of the NV center in Chap. 2. In particular, we first outline the basic properties of the NV before explaining the interaction of the NV spin with static external fields and discussing their influence on the NV spin levels and transitions. Moreover, we describe the two essential coherent manipulation techniques for the NV spin, microwave (MW) spin control and manipulation with time-varying strain fields.

Combining the two spin manipulation toolsets allows us to realize the closed-contour interaction scheme in the NV ground state, where all three possible spin transitions are individually and coherently addressed. To that end, we briefly introduce the underlying experimental system, a hybrid spin-mechanical device, at the beginning of Chap. 3. We then present a detailed study of the system's dynamics under closed-

contour interaction and demonstrate its tunability through the relative phase of the involved driving fields. Additionally and most importantly, we show that this approach of dressing the spin states is highly effective for suppressing environmental perturbations that lead to spin dephasing.

Having revealed the remarkable coherence properties of three-level dressed states, we turn to the question of how to prepare our system in a particular single dressed state. In Chap. 4, we accomplish this by efficient state transfer protocols. A powerful class of such protocols is based on the adiabatic theorem, which we use as a starting point for our studies. In the underlying adiabatic evolutions, the gradual changes of the controls allow the system to adapt its configuration. However, these processes are intrinsically slow and, therefore, have limited effectiveness. To mitigate this drawback, we take advantage of approaches for speeding up adiabatic protocols, collectively known as 'shortcuts to adiabaticity' (STA). These general strategies aim to remedy the limitation of adiabatic approaches by designing fast dynamics that reproduce the results of a slow, adiabatic transition. We thereby realize accelerated, high-fidelity state transfer to the dressed state manifold and consequently enable direct and efficient access to the protected dressed states.

In Chap. 5, we make use of the methods to prepare and read out a particular dressed state and demonstrate coherent manipulation of the dressed states. We present an extensive characterization of the dressed states' properties, including the exploration of the driven and undriven system dynamics. The latter enables us to directly access the dressed state subspace that offers the most efficient coherence protection and to confirm its long coherence time. Hence, we provide full quantum control of our closed-contour dressed states, which is a primarily important feature for their prospective applications.

Due to their notable coherence properties, the three-level dressed states form an appealing resource for high sensitivity nanoscale sensing. As for the NV spin itself, harnessing such a quantum system as a sensor demands a comprehensive characterization of the local internal field environment. In Chap. 6, we present high-resolution electron spin resonance (ESR) spectroscopy on single NV spins at and around zero magnetic field to characterize the intrinsic effective field the NVs experience. We find that for our diamond sample, local strain dominates over the electric field and thereby constitutes the main contribution to the effective field. Furthermore, our experiments yield a method for MW polarization analysis in a tunable, linear basis.

In the final Chap. 7, we summarize our main results and discuss promising routes and exciting prospects that can be pursued with the system discussed in this thesis. We propose concrete applications of the three-level dressed states in sensing schemes and discuss interesting areas in which our three-level system will have a significant impact, e.g. in the exploration of fault-tolerant geometric quantum gates and in the investigation of quantum synchronization. Ultimately, we compile challenging, but feasible perspectives, which we advocate to aim for with our hybrid-spin mechanical system in the future.
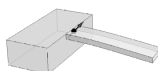
2. Influence of fields on the NV ground state

The NV center in diamond [50, 57] offers outstanding and versatile properties that render it a unique quantum system with auspicious prospects in a wide variety of applications, ranging from quantum information technology [12, 58, 59] to nanoscale quantum sensing of biological and condensed matter systems [60–62]. In particular, its electron spin degree of freedom has triggered an explosion of pioneering experimental demonstrations in these areas. This story of success is based on the convenient all-optical initialization and readout mechanisms the electronic spin of the NV center features. Additionally, the NV spin can be precisely and coherently manipulated with both MW magnetic [63, 64] and strain fields [65, 66] and thereby provides a highly coherent platform to explore a multitude of quantum phenomena, even at room temperature.

The remarkable characteristics of the NV center are to a great extent attributed to its host material [66]. Diamond has a large electronic bandgap, which makes it optically transparent. As the NV's electronic bound states reside deep within this bandgap, they are well isolated from the valence and conduction bands, which ultimately enables the optical NV readout. Moreover, diamond's high Debye temperature and weak spin-orbit interaction contribute to the NV's long coherence and relaxation times. Finally, its robustness and high Young's modulus provide diamond with excellent mechanical properties, allowing for high-quality resonators [67, 68].

To pool diamond's mechanical and the NV's spin capabilities, we exploit a hybrid spin-mechanical system comprising a diamond mechanical cantilever with embedded NV center spins. Crystal strain occurring upon cantilever displacement thereby affords a natural and intrinsic mechanism to couple both systems. The combination of mechanical manipulation and conventional MW control ultimately allows us individual and full coherent control of all NV ground state spin transitions and will be at the heart of our experimental studies.

In the first chapter of this thesis, we introduce the theoretical foundations for our subsequent experiments. We thereby focus on the physical background of the employed three-level system, the ground state of the NV center. We then discuss its response to static external fields, before turning to the aforementioned manipulation techniques based on time-dependent MW and strain fields.
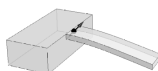
2.1. The NV center in diamond

2.1.1. Structural and electronic properties

The NV center is a paramagnetic lattice defect in diamond. It consists of a substitu-
tional nitrogen atom[1] next to a neighboring lattice vacancy (see Fig. 2.1a). As such
the NV exhibits a trigonal structure in the diamond lattice, which is described by the
C_{3v} symmetry group. The corresponding rotational symmetry axis joins the nitrogen
atom and the vacancy and points along diamonds [111] crystal direction.

  The electronic structure of the NV center comprises charge, orbital, and spin de-
grees of freedom. While there exist several charge states of the NV defect [50], the
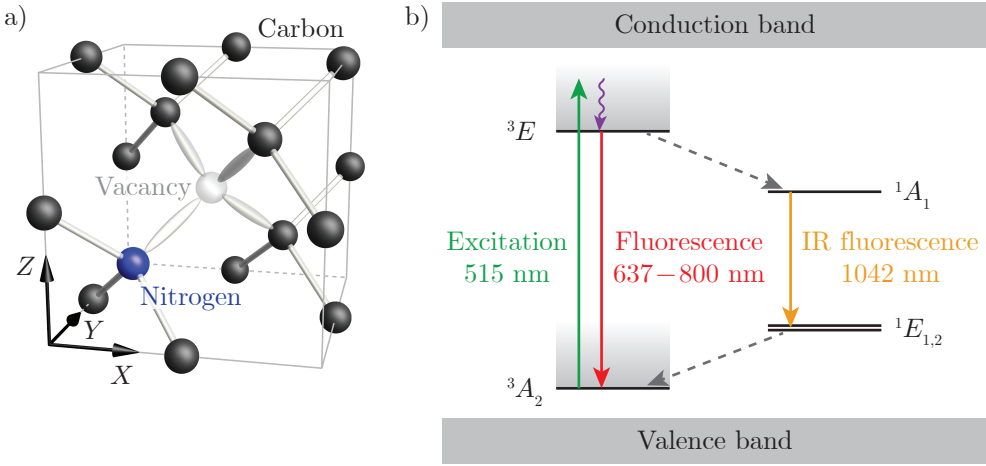negatively charged NV center (NV$^-$) [71], which is at the focus of this thesis, offers

Figure 2.1.: Atomic and electronic structure of the NV center in diamond. a) The
NV center is a point defect in the diamond lattice (black carbon atoms) comprising
a substitutional nitrogen atom (blue) adjacent to a lattice vacancy (transparent).
It has a trigonal structure, with the symmetry axis joining the nitrogen atom and
the vacancy. b) Simplified electronic orbital structure and optical properties of the
NV center at room temperature. The triplet ground state $^3A_2$ and triplet excited
state ^3E manifolds reside deep within the diamond bandgap. The singlet ground
state is located in between the two and consists of three levels $^1E_{1,2}$ and $^1A_1$. Off-
resonant excitation at 515 nm (green) pumps the system into vibronic levels of the
excited state in a spin-conserving transition. The vibronic excitations experience a
rapid, phonon-mediated, radiationless decay (purple), which brings the spin to the
bottom of ^3E. After a few ns (lifetime of the excited state $\approx 6 - 14$ ns [69, 70]) the
NV either relaxes back to the ground state by emitting a photon into the zero-phonon
line (637 nm) or into the phonon sideband (638 − 800 nm, red), or it decays via the
metastable singlet manifold. The latter process comprises both non-radiative decays
(dashed) and a fluorescent decay in the infrared (IR, orange).

---

[1]Nitrogen naturally occurs in two stable isotopes, ^{14}N and ^{15}N. As we solely work with ^{14}N in
this thesis, we will only focus on this isotope in the following.

the most attractive quantum properties. Therefore, we refer to the NV^- state as just NV hereafter. In this negative charge state, the NV center is associated with six electrons, five of which come from the dangling bonds of the nitrogen and carbon atoms, while one additional electron is trapped from a donor atom nearby. The electronic states can be calculated by *ab initio* theory [72, 73] or obtained via symmetry considerations [74]. From the occupation of the molecular orbital states, it follows that there remain two unpaired electrons. The Coulomb interaction between the two electrons is minimized when they are configured in an antisymmetric spatial configuration. The spin configuration, therefore, has to be symmetric (compare to Hund's rule) [74]. As a result, the electronic ground state consists of an orbital singlet, spin triplet state, which is denoted[2] as $^3A_2$. From the $^3A_2$ ground state the NV can be excited to an orbital doublet, spin triplet excited state ^3E via an optical electric dipole transition (see Fig. 2.1b). At room temperature, however, spin-conserving electron-phonon interactions within the excited state manifold mix the orbital states, causing an averaging of the orbital degree of freedom to an effective orbital singlet [75]. The resulting excited state structure strongly resembles the ground state spin triplet [74, 76, 77]. The spin singlet ground state (levels $^1E_{1,2}$ and $^1A_1$) is located in between the ground and excited state manifolds. All levels are deep within the 5.5 eV bandgap of diamond, such that valence and conduction bands are not involved in optical transitions between the NV states [50]. Thus, based on the electronic structure, one identifying feature of the NV is the optical zero-phonon line at 637 nm [78, 79], with an associated vibronic sideband extending to larger wavelengths in emission. Additionally, the separation of the singlet states give rise to an infrared (IR) transition at 1042 nm [80] (see Fig. 2.1b).

2.1.2. Ground state spin Hamiltonian

In our experiments, we focus on the NV's spin degree of freedom, in particular on the NV's electronic ground state triplet, which has been the subject of most NV-related research to date and exploited in diverse areas [12, 58, 60, 81]. The fine structure of this $S = 1$ spin system comprises the eigenstates $|m_s\rangle$ of the spin projection operator $\hat{S}_z$ with respect to the NV's symmetry axis. Here, $m_s = 0, \pm 1$ denote the corresponding spin quantum numbers. Spin-spin interactions split the degenerate $|-1\rangle$ and $|+1\rangle$ from $|0\rangle$ by the zero-field splitting $D_0 \approx 2.87$ GHz (see Fig. 2.2).

The fine structure levels are affected by interactions between the NV's electron spin density and the nuclear spin of the ^{14}N atom, giving rise to a hyperfine structure. As the ^{14}N nucleus possesses a nuclear spin $I = 1$ and a nuclear electric quadrupolar moment, the hyperfine interaction has both magnetic and electric components [82]. The magnetic component accounts for both the non-zero overlap of the electron spin density with the spatial position of the ^{14}N nucleus (Fermi contact contribution) and the dipolar contribution emerging from the interaction of the NV electron spin and ^{14}N nuclear spin. In contrast, the electric component describes the interaction of the electric field gradient arising from the NV's electronic charge distribution with the electric quadrupole moment associated with the finite charge distribution of the nucleus [83]. Due to the quadrupolar interaction the ^{14}N nuclear spin has the same quantization axis as the NV electronic spin.

---

[2] The label of the states indicate the orbital symmetry of the C_{3v} group (A_1, A_2 and E) and the spin multiplicity $2S + 1$, where $S = 1$ [74].
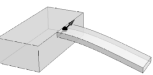
All fine and hyperfine interactions are described by the Hamiltonian of the NV's spin ground state [50, 73], which reads

$$\hat{\mathcal{H}}/h = D_0\left(\hat{S}_z^2 - 2/3\right) + A_{\mathrm{HF}}^{\parallel}\hat{S}_z\hat{I}_z + A_{\mathrm{HF}}^{\perp}\left(\hat{S}_x\hat{I}_x + \hat{S}_y\hat{I}_y\right) + P\left(\hat{I}_z^2 - 2/3\right) . \quad (2.1)$$

Here, $\hat{\boldsymbol{S}} = (\hat{S}_x, \hat{S}_y, \hat{S}_z)$ and $\hat{\boldsymbol{I}} = (\hat{I}_x, \hat{I}_y, \hat{I}_z)$ are the vectors of the dimensionless electronic $S = 1$ and nuclear $I = 1$ spin operators of the NV and ^{14}N spin, respectively, and h is Planck's constant. Expressions for the components of the electronic spin operator $\hat{\boldsymbol{S}}$ in the $\{\ket{+1}, \ket{0}, \ket{-1}\}$ basis (Zeeman basis) are

$$\hat{S}_x = \frac{1}{\sqrt{2}}\begin{pmatrix} 0 & 1 & 0 \\ 1 & 0 & 1 \\ 0 & 1 & 0 \end{pmatrix}, \quad \hat{S}_y = \frac{1}{\sqrt{2}\mathrm{i}}\begin{pmatrix} 0 & 1 & 0 \\ -1 & 0 & 1 \\ 0 & -1 & 0 \end{pmatrix}, \quad \hat{S}_z = \begin{pmatrix} 1 & 0 & 0 \\ 0 & 0 & 0 \\ 0 & 0 & -1 \end{pmatrix}.$$
$$(2.2)$$

Equivalent definitions hold for the components of the ^{14}N nuclear spin operator $\hat{\boldsymbol{I}}$ [82].

By considering Hamiltonian (2.1) we can evaluate the impact of the hyperfine interactions on the NV level structure (see Fig. 2.2). We denote the hyperfine states by $\ket{m_s, m_I}$, with $m_I = 0, \pm 1$ being the eigenvalues of the $\hat{I}_z$ nuclear spin operator. While the electric contribution shifts all levels with $m_I = \pm 1$ with respect to the $m_I = 0$ states by the nuclear electric quadrupole parameter $P = -4.95\,\mathrm{MHz}$ [84], the magnetic contribution induces a splitting of $\{\ket{-1,-1}, \ket{+1,+1}\}$ and $\{\ket{-1,+1}, \ket{+1,-1}\}$ from
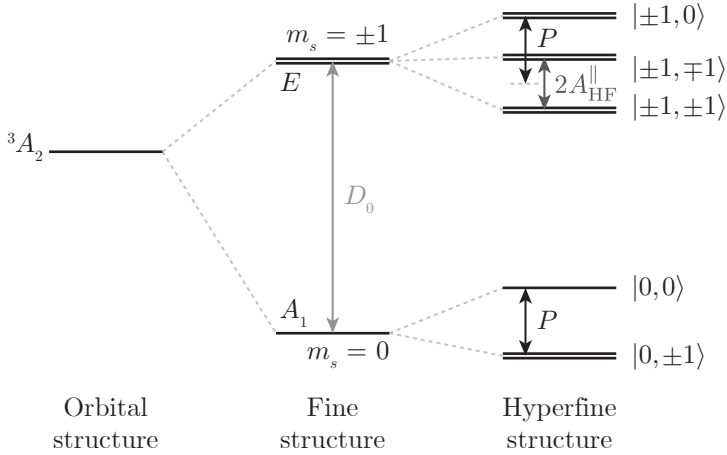
Figure 2.2.: Fine and hyperfine structure of the $S = 1$ ground state. Spin-spin interactions split the $^3A_2$ orbital state into $\ket{m_s = 0}$ and $\ket{m_s = \pm 1}$, which are separated by the zero-field splitting D_0. Electric and magnetic hyperfine interactions between the NV's electronic spin and the ^{14}N nucleus (nuclear spin $I = 1$) additionally split the levels by the nuclear quadrupole parameter P and the axial magnetic hyperfine parameter $A_{\mathrm{HF}}^{\parallel}$, respectively. The hyperfine levels are labeled by their spin projections on the NV's symmetry axis, $\ket{m_s, m_I}$. Note that around zero external magnetic field the effect of the non-axial hyperfine interaction $A_{\mathrm{HF}}^{\perp}$ is suppressed by D_0.

$\{|-1,0\rangle, |+1,0\rangle\}$ by the axial hyperfine parameter $A_{\mathrm{HF}}^{\|} = -2.14\,\mathrm{MHz}$ and a mixing of nearly degenerate states with a spin and nuclear projection difference of $\Delta m_s = \pm 1$ and $\Delta m_I = \mp 1$ by the non-axial hyperfine parameter $A_{\mathrm{HF}}^{\perp} = -2.7\,\mathrm{MHz}$ [85].

In the following, we will neglect several contributions of Hamiltonian (2.1), as they do not affect the spin states or spin transitions in the parameter regime of weak magnetic fields we consider in the experiments ($B \lesssim 30\,\mathrm{G}$). First, the terms of $2/3$ in the zero-field splitting and the quadrupolar coupling won't be considered as they only denote global energy shifts of all involved states. Second, we will disregard the non-axial hyperfine interaction, as it couples states with a spin quantum number difference of $\Delta m_s = \pm 1$ and is consequently suppressed by the zero-field splitting[3] ('secular approximation'). Lastly, the nuclear electric quadrupole interaction does not cause a mixing of states with different m_s and, therefore, does not affect the electron spin transition frequencies, so that it won't be relevant for our experimental results and will be disregarded as well.

We note that besides the internal coupling between the ^{14}N nucleus and the NV spin itself, the hyperfine interaction also gives rise to an extrinsic coupling of the NV spin to other nuclei in the diamond crystal lattice. Carbon naturally occurs with an abundance of $98.9\,\%$ as ^{12}C, which has zero nuclear spin ($I = 0$). In contrast, ^{13}C possesses a nuclear spin $I = 1/2$ and affects the NV spin properties in terms of an additional magnetic hyperfine interaction[4]. With a natural abundance of $1.1\,\%$ such ^{13}C isotopic impurities are randomly distributed in the diamond lattice. The resulting nuclear spin bath induces a fluctuating magnetic environment ultimately causing decoherence of the NV spin [86, 87]. If however, an individual ^{13}C atom is in the vicinity of the NV a discrete set of distinguishable hyperfine couplings is possible [88, 89]. We will discuss such an extrinsic hyperfine coupling in Sec. 2.2.4.

2.1.3. Optical properties and spin polarization

Besides its unique level structure, the NV offers the intriguing possibility to initialize and read out the ground state spin by purely optical means [55, 56, 90, 91]. The $^3A_2 \leftrightarrow {}^3E$ transition normally is a spin-conserving transition for both resonant and non-resonant optical excitation. Due to the presence of the metastable singlet states, however, exciting the NV spin with laser light (in our case non-resonantly with $515\,\mathrm{nm}$) does not necessarily result in a closed optical transition (see Fig. 2.1b). Specifically, after optical excitation into the ^3E manifold, two possible pathways compete with each other. On the one hand, direct optical decay to the ground state preserves the spin projection and gives rise to visible fluorescence. On the other hand, non-radiative decay to the intermediate singlet state is enabled by spin-orbit coupling. This 'intersystem crossing' is spin-selective and preferentially occurs for the $m_s = \pm 1$ spin states [92, 93]. The non-radiative transfer to the singlet state is followed by an immediate decay within the metastable singlet manifold causing the emission of an IR photon. Finally, the system decays back into the ground state with similar decay rates for all spin projections [91, 92].

---

[3] Hereafter we refer to the axial hyperfine interaction as just hyperfine interaction, $A_{\mathrm{HF}}^{\|} \equiv A_{\mathrm{HF}}$.

[4] As $I = 1/2$, ^{13}C has no electric quadrupole moment, since only nuclei with spin $I \geq 1$ may possess electric quadrupole moments [82].
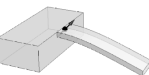
The longer lifetime of the metastable singlet state ($\approx 150\,\mathrm{ns}$ [91, 94]) compared to the triplet excited state ($\approx 6 - 14\,\mathrm{ns}$ [69, 70]) leads to an effective shelving of the spin population decaying via this pathway, thereby introducing a difference in the visible fluorescence. Accordingly, the NV exhibits a spin-dependent (initial) fluorescence intensity, with the $m_s = \pm 1$ spin levels exhibiting up to $\approx 30\,\%$ less fluorescence compared to the $m_s = 0$ states [50]. Additionally, the dynamics described above induce a spin polarization of up to $\approx 90\,\%$ into the $m_s = 0$ state of the ground state when the NV is optically excited for about $1\,\mathrm{\mu s}$ near saturation [95]. Thus, the initial fluorescence intensity allows for discrimination of the spin state, while spin polarization is achieved once the steady state under optical pumping has been reached.

2.2. Effect of static external and internal perturbations

The NV center has long shown promise as an excellent and versatile quantum sensor with nanoscale spatial resolution, even at ambient conditions. This applicability is based on the NV's exceptional sensitivity to external fields, including magnetic fields [96–99], electric fields [100, 101], strain [102–106], and temperature [107–110]. In this section, we discuss the response of the NV ground state to these external fields in detail [73]. Additionally, we explain the signatures of the extrinsic hyperfine coupling between an individual $^{13}\mathrm{C}$ nuclear spin and the NV spin within the ground state level structure.

2.2.1. Static magnetic fields

An external static magnetic field couples to the permanent magnetic moments of the NV's electron spin and the $^{14}\mathrm{N}$ nuclear spin. Both magnetic interactions are described by the Zeeman effect and the corresponding Hamiltonian, which adds to Hamiltonian (2.1), reads

$$
\begin{aligned}
\hat{\mathcal{H}}_{\mathrm{mag}}/h &= \gamma_{\mathrm{NV}}\boldsymbol{B} \cdot \hat{\boldsymbol{S}} + \gamma_{\mathrm{N}}\boldsymbol{B} \cdot \hat{\boldsymbol{I}} \\
&= \gamma_{\mathrm{NV}}\left(B_x\hat{S}_x + B_y\hat{S}_y + B_z\hat{S}_z\right) + \gamma_{\mathrm{N}}\left(B_x\hat{I}_x + B_y\hat{I}_y + B_z\hat{I}_z\right) .
\end{aligned}
\tag{2.3}
$$

Here, $\hat{\boldsymbol{S}} = (\hat{S}_x, \hat{S}_y, \hat{S}_z)$ and $\hat{\boldsymbol{I}} = (\hat{I}_x, \hat{I}_y, \hat{I}_z)$ are the spin operators as defined in Eq. (2.2) and $\boldsymbol{B} = (B_x, B_y, B_z)$ is the external magnetic field given in the coordinate frame (x, y, z) of the NV. Here, z denotes the NV's symmetry axis (quantization axis) and we choose y to lie in one of the NV's symmetry planes. The NV gyromagnetic ratio $\gamma_{\mathrm{NV}} = g_e\mu_B/h = 2.80\,\mathrm{MHz/G}$ is given by the NV's isotropic g-factor[5] $g_e = 2.0028$ [71, 83] and the Bohr magneton μ_B, whereas the $^{14}\mathrm{N}$ gyromagnetic ratio $\gamma_{\mathrm{N}} = g_{\mathrm{N}}\mu_{\mathrm{N}}/h = 0.308\,\mathrm{kHz/G}$ is defined by the isotropic $^{14}\mathrm{N}$ nuclear g-factor $g_{\mathrm{N}} = 0.404$ and the nuclear magneton μ_{N}. As the nuclear Zeeman coupling is four orders of magnitude smaller than the one for the electron, we won't take it into account in the following.

---

[5]A slight anisotropy of the g-factor was reported in [85], which results in an anisotropic g-tensor with components $g_\parallel = 2.0029$ and $g_\perp = 2.0031$ for axial and transverse magnetic field components, respectively. However, we will neglect this minute anisotropy.

By diagonalizing the sum of the NV ground state Hamiltonian (2.1) and the magnetic interaction Hamiltonian (2.3), the effect of an external magnetic field on the NV states can be illustrated. Applying a magnetic field parallel to the NV axis, $\boldsymbol{B} = (0, 0, B_\parallel)$, shifts each of the $m_s = \pm 1$ hyperfine states by $m_s \gamma_{\mathrm{NV}} B_\parallel$ (independent of m_I), whereas the $m_s = 0$ states are not affected. Consequently, the frequencies of the six possible hyperfine transitions from $|0\rangle$ to $|-1\rangle$ and $|0\rangle$ to $|+1\rangle$ vary linearly with $B_\parallel$ and show a Zeeman splitting of $\Delta_Z = 2\gamma_{\mathrm{NV}} B_\parallel$ (see Fig. 2.3a). In contrast, a transverse magnetic field with amplitude $B_\perp = (B_x^2 + B_y^2)^{1/2}$ mixes the electron spin states, which results in a quadratic dependence of the transition frequencies. In case of $m_I = 0$ the transition frequencies read $\omega_-/2\pi = D_0/2 + [D_0^2 + (2\gamma_{\mathrm{NV}} B_\perp)^2]^{1/2}/2$ and $\omega_+/2\pi = [D_0^2 + (2\gamma_{\mathrm{NV}} B_\perp)^2]^{1/2}$. For the states with $m_I = \pm 1$ the (axial) hyperfine coupling needs to be considered, which leads to a deviation from the given quadratic dependence for $\gamma_{\mathrm{NV}} B_\perp \lesssim A_{\mathrm{HF}} \approx 2\,\mathrm{MHz}$. Thereby, two hyperfine states with opposing nuclear spin projection always remain degenerate, ultimately resulting in four resolvable transition frequencies. As the coupling to perpendicular magnetic fields is of second order, we can neglect its effect when we work with parallel magnetic fields in our experiments, since we can carefully align the field to the NV axis with $< 0.2°$ mismatch (see App. A.1.1).

## 2.2.2. Effective electric and stress fields

Besides the response to external magnetic fields, the NV ground state is also susceptible to electric field and stress. We will see that both perturbations can be described by defining an effective electric and stress field, as the interaction Hamiltonians have similar form [82]. In general, electric field and stress couple only to the orbital degree of freedom and not to the spin [66]. In addition, spin-orbit interactions vanish to first order in the ground state, as the orbital wavefunction is antisymmetric (see Sec. 2.1.1) and thus has no orbital angular momentum [50]. Nevertheless, a non-zero coupling between the spin degree of freedom and stress or electric fields exists due to spin-orbit coupling between the ground and excited spin triplet states. Since this coupling is suppressed by the energy splitting between both manifolds, this effect is however small[6] [100].

We first focus on the interaction of the NV spin with an electric field. From a theoretical perspective, the coupling to an external electric field $\boldsymbol{E} = (E_x, E_y, E_z)$ is described by the linear Stark effect [82]. The corresponding interaction Hamiltonian is constrained by the C_{3v} symmetry of the NV [105] and reads

$$
\begin{aligned}
\hat{\mathcal{H}}_{\mathrm{el}}/h &= \hat{\mathcal{H}}_{\mathrm{el},0}/h + \hat{\mathcal{H}}_{\mathrm{el},1}/h + \hat{\mathcal{H}}_{\mathrm{el},2}/h \\
&= d_\parallel E_z \hat{S}_z^2 + \\
&\quad + d_\perp' E_x \left(\hat{S}_x \hat{S}_z + \hat{S}_z \hat{S}_x \right) + d_\perp' E_y \left(\hat{S}_y \hat{S}_z + \hat{S}_z \hat{S}_y \right) + \\
&\quad + d_\perp E_x \left(\hat{S}_y^2 - \hat{S}_x^2 \right) + d_\perp E_y \left(\hat{S}_x \hat{S}_y + \hat{S}_y \hat{S}_x \right) ,
\end{aligned}
\tag{2.4}
$$

where the subscripts 0, 1, and 2 refer to the difference of the electron spin quantum numbers m_s that are connected by the corresponding part of the Hamiltonian.

---

[6] Compared to the $^3A_2$ ground state the ^3E excited state is much more sensitive to the presence of electric field and stress as its orbital doublet structure offers an orbital degree of freedom [74, 111].
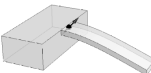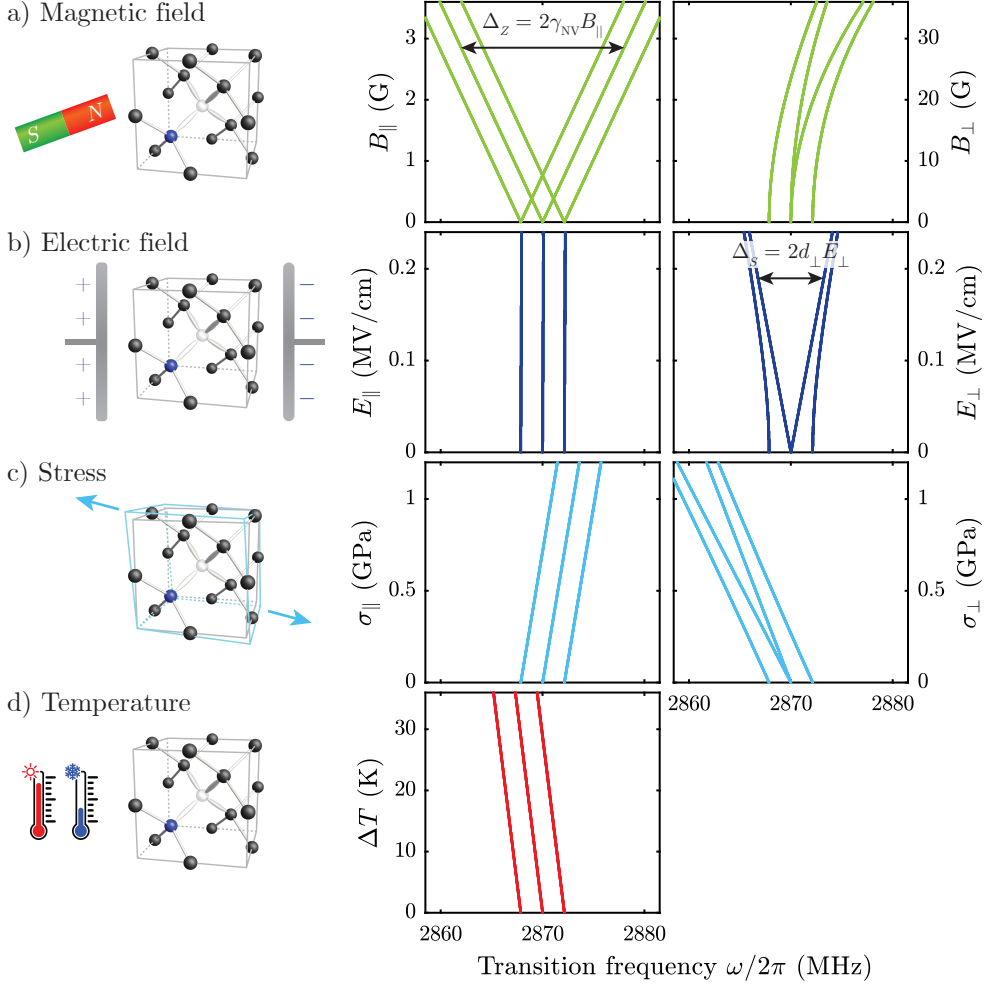
Figure 2.3.: Response of the NV ground state transition frequencies to static external fields. a) An axial magnetic field $B_\parallel$ causes a Zeeman splitting Δ_Z of the hyperfine states with $m_s = \pm 1$, leading to a linear dispersion of the six possible spin transitions from $|0\rangle$ to $|-1\rangle$ and $|0\rangle$ to $|+1\rangle$. Applying a transverse magnetic field $B_\perp$ mixes the hyperfine levels and results in a second-order shift of the transition frequencies. b) An axial electric field $E_\parallel$ slightly shifts $|-1\rangle$ and $|+1\rangle$ with respect to $|0\rangle$. Correspondingly, the transitions show a very weak linear response characterized by $d_\parallel$. In a transverse electric field $E_\perp$, $|-1\rangle$ and $|+1\rangle$ are mixed and split, resulting in a linear Stark splitting Δ_S of the hyperfine states. Note that for small electric fields the response of the $m_I = \pm 1$ states is suppressed by the hyperfine coupling, causing a second-order response. c) Applying uniaxial stress with amplitude $\sigma_\parallel$ along the NV's symmetry axis [111] induces a common-mode shift of $|-1\rangle$ and $|+1\rangle$ with respect to $|0\rangle$ similar to an axial electric field, but with larger susceptibility. However, uniaxial stress with amplitude $\sigma_\perp$ transverse to the NV axis (e.g. along [10$\bar{1}$]) induces both a splitting and a shift of $|-1\rangle$ and $|+1\rangle$. This is a direct consequence of the parameters of the spin-stress interaction (see Eq. (2.6)), which consider the tensor character of stress. d) Around $T \approx 300\,\mathrm{K}$ variations of the environmental temperature affect the zero-field splitting D_0 linearly, with $\mathrm{d}D_0/\mathrm{d}T = -74.2\,\mathrm{kHz/K}$.

The axial and transverse electric field susceptibilities are $d_\parallel = 0.35\,\mathrm{Hz\,cm/V}$ and $d_\perp = 17\,\mathrm{Hz\,cm/V}$ [112], whereas the susceptibility $d'_\perp$ has not been quantified experimentally or theoretically up to now, but is excepted to have the same order of magnitude as $d_\perp$ [82] and may be determined by the methods described in [105]. The electric field interaction Hamiltonian (2.4) is universal for defects with C_{3v} symmetry, but was derived specifically for the NV in [82, 105]. Note that we will disregard the effect of $\hat{\mathcal{H}}_{\mathrm{el},1}$ in the following, as it is suppressed by the zero-field splitting between the $m_s = 0$ and $m_s = \pm1$ states in the regime of weak magnetic fields we study within this thesis.

Considering the reduced interaction Hamiltonian (2.4) we find two different types of coupling mechanisms. First, there are symmetry-conserving interactions that only shift the spin states ($\hat{\mathcal{H}}_{\mathrm{el},0}$), whereas symmetry-breaking interactions may mix the spin levels ($\hat{\mathcal{H}}_{\mathrm{el},2}$). For example, an axial electric field, $\boldsymbol{E} = (0, 0, E_\parallel)$, gives rise only to the contribution of $\hat{\mathcal{H}}_{\mathrm{el},0}$, resulting in a common-mode shift of all $m_s = \pm1$ hyperfine states with respect to the $m_s = 0$ levels, which are not affected by $\hat{\mathcal{H}}_{\mathrm{el},0}$. Consequently, the transition frequencies experience a linear Stark shift of $d_\parallel E_\parallel$, while the two-fold degeneracy of the transitions is maintained (see Fig. 2.3b). On the other hand, in a transverse electric field with amplitude $E_\perp = (E_x^2 + E_y^2)^{1/2}$ the $|-1\rangle$ and $|+1\rangle$ hyperfine states are mixed and split according to $D_0 \pm [(d_\perp E_\perp)^2 + (m_I A_{\mathrm{HF}})^2]^{1/2}$. Thus, the $m_I = 0$ transition frequencies experience a linear Stark splitting of $\Delta_S = 2d_\perp E_\perp$, whereas for the $m_I = \pm1$ transitions the axial hyperfine coupling suppresses the effect of electric perturbations in first order, resulting in a quadratic response.

The interaction between the NV spin and stress is more complicated than for the electric field coupling. While the electric field has vector character, stress needs to be described as a tensor to account for normal and shear stress components [113, 114]. Thus, stress-coupling results in more coupling coefficients that need to be considered compared to electric field coupling. Indeed, the spin-stress interaction Hamiltonian in its most general form compatible with the C_{3v} symmetry requirements of the NV is represented in an analogous way to the electric interaction Hamiltonian (2.4)[7], but contains six independent real coupling parameters. This interaction Hamiltonian has been only recently derived completely [105] and reads

$$
\begin{aligned}
\hat{\mathcal{H}}_\sigma/h &= \hat{\mathcal{H}}_{\sigma,0}/h + \hat{\mathcal{H}}_{\sigma,1}/h + \hat{\mathcal{H}}_{\sigma,2}/h \\
&= \mathcal{M}_z \hat{S}_z^2 + \\
&\quad + \mathcal{N}_x \left(\hat{S}_x \hat{S}_z + \hat{S}_z \hat{S}_x \right) + \mathcal{N}_y \left(\hat{S}_y \hat{S}_z + \hat{S}_z \hat{S}_y \right) + \\
&\quad + \mathcal{M}_x \left(\hat{S}_y^2 - \hat{S}_x^2 \right) + \mathcal{M}_y \left(\hat{S}_x \hat{S}_y + \hat{S}_y \hat{S}_x \right) ,
\end{aligned}
\tag{2.5}
$$

where the parameters of the spin-stress interaction weight the components of the stress tensor $\boldsymbol{\sigma}$ (given in crystal coordinates) with the corresponding spin-stress coupling strength parameters (a_1, a_2, b, c, d, e) [105, 106].

---

[7]The Hamiltonians (2.4) and (2.5) represent both the most general form of the spin-electric and spin-stress interaction compatible with the C_{3v} symmetry. They satisfy the requirements of time-reversal symmetry, the spatial symmetries of the point group, and the linearity in the corresponding field [105].
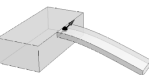
The resulting coupling parameters are given by

$$\mathcal{M}_z = a_1(\sigma_{XX} + \sigma_{YY} + \sigma_{ZZ}) + 2a_2(\sigma_{YZ} + \sigma_{ZX} + \sigma_{XY}) , \tag{2.6a}$$

$$\mathcal{N}_x = d(2\sigma_{ZZ} - \sigma_{XX} - \sigma_{YY}) + e(2\sigma_{XY} - \sigma_{YZ} - \sigma_{ZX}) , \tag{2.6b}$$

$$\mathcal{N}_y = \sqrt{3}\left[d(\sigma_{XX} - \sigma_{YY}) + e(\sigma_{YZ} - \sigma_{ZX})\right] , \tag{2.6c}$$

$$\mathcal{M}_x = b(2\sigma_{ZZ} - \sigma_{XX} - \sigma_{YY}) + c(2\sigma_{XY} - \sigma_{YZ} - \sigma_{ZX}) , \tag{2.6d}$$

$$\mathcal{M}_y = \sqrt{3}\left[b(\sigma_{XX} - \sigma_{YY}) + c(\sigma_{YZ} - \sigma_{ZX})\right] . \tag{2.6e}$$

Similar to the electric interaction Hamiltonian (2.4) the subscripts 0, 1, and 2 refer to the difference in the electron spin quantum numbers m_s connected by the corresponding part of the Hamiltonian. Note that the spin-stress interaction Hamiltonian (2.5) is given in the 'hybrid' representation, i.e. it is expressed in terms of the NV frame components of the spin vector ($\hat{S}_x$, $\hat{S}_y$, and $\hat{S}_z$) and the cubic frame components of the stress tensor (σ_{XX}, σ_{XY}, ...), which reference the diamond lattice (see Fig. 2.1a). For a representation of the spin-stress interaction Hamiltonian completely in the NV frame we refer the reader to [105]. Up to now, measurements have yielded four of the six spin-stress coupling strength parameters [104, 106], $a_1 = -4.4\,\text{MHz/GPa}$, $a_2 = 3.7\,\text{MHz/GPa}$, $b = 2.3\,\text{MHz/GPa}$, and $c = -3.5\,\text{MHz/GPa}$ in [104]. Using density functional theory it was found that the parameters d and e are in the same order of magnitude as the other four parameters, $d = -0.12\,\text{MHz/GPa}$ and $e = 0.66\,\text{MHz/GPa}$ [105]. Both parameters may be determined experimentally using similar methods as for $d'_{\perp}$ [105]. Note that we will neglect $\hat{\mathcal{H}}_{\sigma,1}$ from now on, as its effect is suppressed by the zero-field splitting for weak magnetic fields, in analogy to $\hat{\mathcal{H}}_{\text{el},1}$ from Eq. (2.4).

If the mechanical deformation is characterized in terms of a strain tensor $\underline{\varepsilon}$ instead of a stress tensor $\underline{\sigma}$, the spin-strain interaction is described completely analogous to Eq. (2.5), but with the substitutions $\underline{\sigma} \mapsto \underline{\varepsilon}$ and corresponding spin-strain coupling strength parameters instead of the spin-stress susceptibilities (refer to [105, 106] for more details).

To illustrate the spin-stress interaction on the ground state levels, we first consider uniaxial stress applied along the NV axis. Such stress changes the relative distance between the lattice atoms but maintains the C_{3v} symmetry of the defect, so that the energy of the $|-1\rangle$ and $|+1\rangle$ hyperfine states are increased (compressive stress) or decreased (tensile stress) with respect to $|0\rangle$ [66]. The corresponding hyperfine transition frequencies shift linearly with the amplitude of the applied stress $\sigma_{\parallel}$ according to $\omega/2\pi = (\sqrt{3}a_1 + 2\sqrt{3}a_2)\sigma_{\parallel}$, while maintaining the two-fold degeneracy (see Fig. 2.3c). Uniaxial stress with amplitude $\sigma_{\perp}$ applied transverse to the NV axis breaks the trigonal symmetry of the NV, resulting in a mixing of the $|-1\rangle$ and $|+1\rangle$ hyperfine states accompanied by a shift. The occurrence of both effects, i.e. mixing and shifting, is a direct consequence of the tensor character of stress and results from the parameters of the spin-stress interaction given in Eq. (2.6). We obtain $\omega_{\pm}/2\pi = D_0 + (a_1 - a_2)\sigma_{\perp} \pm [(b+c)^2\sigma_{\perp}^2 + (m_I A_{\text{HF}})^2]^{1/2}$ for the corresponding response of the hyperfine transition frequencies, verifying the common-mode shift of all $|-1\rangle$ and $|+1\rangle$ (first term) and a splitting that depends on the nuclear spin projection m_I (second term). Again, the effect of the splitting is suppressed to first order for the $m_I = \pm 1$ transitions due to the axial hyperfine coupling, in analogy to the transverse electric field.

By comparing the spin-electric and spin-stress interaction Hamiltonians (2.4) and (2.5) it becomes obvious that both perturbations can be treated in similar ways. Consequently, we define the effective field as the combined strain and electric field [82]. In the NV's coordinate frame it is represented by $\mathbf{\Pi} = (\Pi_x, \Pi_y, \Pi_z)$, where its components are $\Pi_{x,y} = d_\perp E_{x,y} + \mathcal{M}_{x,y}$ and $\Pi_z = d_\parallel E_z + \mathcal{M}_z$. The interaction of the NV ground state with the effective field can then be written as

$$\hat{\mathcal{H}}_{\text{eff}}/h = \Pi_z \hat{S}_z^2 + \Pi_x\left(\hat{S}_y^2 - \hat{S}_x^2\right) + \Pi_y\left(\hat{S}_x\hat{S}_y + \hat{S}_y\hat{S}_x\right) , \tag{2.7}$$

where we neglected the coupling terms with $\Delta m_s = \pm 1$[8].

Comparing the electric field susceptibilities with the spin-stress coupling strength parameters yields an important feature characterizing the effective field interaction. While we find $d_\perp \approx 50 d_\parallel$, all spin-stress coupling strength parameters are of comparable magnitude. This implies that the average effect of a randomly oriented electric field leads to a large splitting of the transition frequencies with a negligible common-mode shift, while in the case of stress the splitting is accompanied by a common-mode shift in the same order of magnitude [115, 116]. Thus, by averaging over an ensemble of electric field and stress arrangements, one can differentiate between their relative contributions to the effective field by considering the spectral response. This property will be used in Chap. 6 to characterize the effective field of individual NV centers.

2.2.3. Temperature

At ambient conditions, temperature variations affect the NV ground state spin manifold as well. In particular, it was found that the zero-field splitting D_0 is temperature-dependent and decreases slightly with increasing temperature T [107]. The linear dispersion valid around room temperature is characterized by $\mathrm{d}D_0/\mathrm{d}T = -74.2\,\text{kHz/K}$ (see Fig. 2.3d). As environmental temperature fluctuations cannot be completely suppressed in our experiments, they constitute an important limitation of our experimental setup, which will be discussed later (see e.g. Sec. 3.3 for more details).

### 2.2.4. Hyperfine interaction with nuclear spins

When a single ^{13}C nuclear spin occupies a lattice site in the vicinity of the NV center, it can individually couple to the NV spin via the magnetic hyperfine interaction. The general interaction Hamiltonian [88, 89] reads

$$\hat{\mathcal{H}}_{\text{HF}}^{(C)}/h = \hat{\boldsymbol{S}} \cdot \underline{\boldsymbol{A}} \cdot \hat{\boldsymbol{I}}^{(C)} , \tag{2.8}$$

where $\hat{\boldsymbol{I}}^{(C)}$ is the dimensionless nuclear spin operator of the ^{13}C nucleus with $I^{(C)} = 1/2$ and $\underline{\boldsymbol{A}}$ the hyperfine tensor defined by

$$\underline{\boldsymbol{A}} = \begin{pmatrix} A_{xx} & A_{xy} & A_{xz} \\ A_{yx} & A_{yy} & A_{yz} \\ A_{zx} & A_{zy} & A_{zz} \end{pmatrix} . \tag{2.9}$$

---

[8]To take account of these couplings additional effective field terms $\Sigma_{x,y} = d'_\perp E_{x,y} + \mathcal{N}_{x,y}$ can be introduced and correspondingly added to Hamiltonian (2.7).
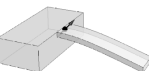
In the case of a weak external magnetic field applied along the NV axis, terms proportional to $\hat{S}_x$ and $\hat{S}_y$ can be neglected within the secular approximation [117, 118]. This simplifies Hamiltonian (2.8) to

$$\hat{\mathcal{H}}_{\mathrm{HF}}^{(C)}/h = \hat{S}_z \sum_{i=x,y,z} A_{zi}\hat{I}_i^{(C)} \ . \tag{2.10}$$

Hence, the ^{13}C hyperfine coupling causes a splitting and mixing of the NV's hyperfine states $|m_s, m_I\rangle$, which in the present case are characterized by the additional ^{13}C nuclear spin quantum number, $|m_s, m_I, m_I^{(C)}\rangle$, with $m_I^{(C)} = \pm 1/2$. To evaluate how the $|m_s, m_I\rangle$ states with $m_s = \pm 1$ split due to ^{13}C hyperfine coupling, we diagonalize the complete interaction Hamiltonian. This Hamiltonian comprises Eq. (2.1), Eq. (2.3), and Eq. (2.10) in combination with a Zeeman coupling of the ^{13}C nuclear spin, $\gamma_C \boldsymbol{B} \cdot \hat{\boldsymbol{I}}^{(C)}$, where $\gamma_C = 1.07\,\mathrm{kHz/G}$ is the gyromagnetic ratio of the ^{13}C nuclear spin [89]. For a parallel magnetic field, we find

$$\Delta^{(C)} = \left[A_{zx}^2 + A_{zy}^2 + (A_{zz} - \gamma_C B_\parallel)^2\right]^{1/2} + \gamma_C B_\parallel \ . \tag{2.11}$$

In reasonably low magnetic fields, the contribution of the nuclear Zeeman splitting can be neglected, resulting in a hyperfine splitting of

$$\Delta^{(C)} = \left(A_{zx}^2 + A_{zy}^2 + A_{zz}^2\right)^{1/2} \equiv A_{\mathrm{HF}}^{(C)} \ , \tag{2.12}$$

where we introduced the ^{13}C hyperfine coupling strength $A_{\mathrm{HF}}^{(C)}$ [88]. Note that only certain discrete values for the hyperfine splitting were observed, as the ^{13}C isotope can only occupy discrete lattice sites in the vicinity of the NV. For example, the
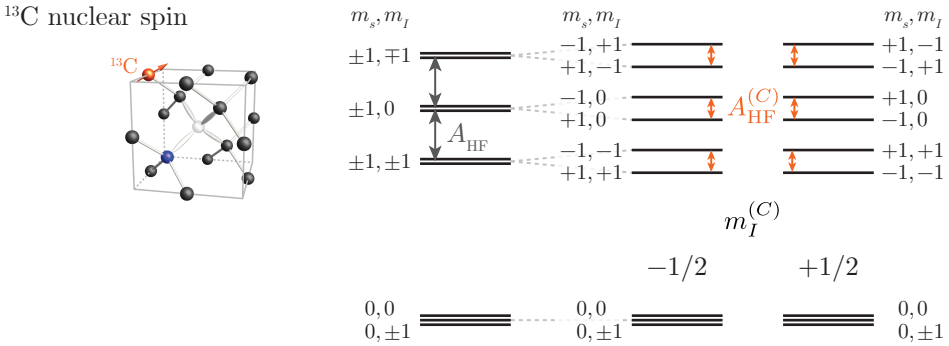

Figure 2.4.: Hyperfine interaction between the NV spin and a nearby ^{13}C nuclear spin ($I = 1/2$). Due to spin-spin interactions, the hyperfine levels of the NV ground state experience an additional splitting according to the nuclear spin projection of the ^{13}C spin, $m_I^{(C)} = \pm 1/2$. The level scheme is given for a positive ^{13}C hyperfine parameter, $A_{\mathrm{HF}}^{(C)} > 0$ with $A_{\mathrm{HF}}^{(C)} < A_{\mathrm{HF}}$, and for negligible off-diagonal components of the hyperfine tensor. Consequently, without any external field applied each of the hyperfine states is two-fold degenerate, leading to six nuclear spin-conserving transitions.

maximum hyperfine coupling strength for a ^{13}C placed in one of the nearest neighbor lattice sites of the vacancy is $130\,\mathrm{MHz}$ [85], while for other proximal lattice sites, the coupling strengths are in the order of $\approx 1\,\mathrm{MHz}$. A detailed classification of possible hyperfine couplings strengths is presented in [88, 89].

In Fig. 2.4 we illustrate the level splitting of the hyperfine states in the presence of a nearby individual ^{13}C nuclear spin when the off-diagonal terms are negligible and $A_{\mathrm{HF}}^{(C)} > 0$. At zero-field all $m_s = \pm 1$ hyperfine states split into two sublevels with an energy splitting $A_{\mathrm{HF}}^{(C)}$. Consequently, there are six possible nuclear spin-conserving transitions. As the involved sublevels are two-fold degenerate, the spin transitions split into a total of twelve transitions in an external magnetic field.

2.3. MW spin manipulation

Up to now, we only considered the effect of static fields on the NV's ground state, causing static changes of the level structure. In contrast, time-varying external fields introduce a time-dependence to the system. Specifically, magnetic fields in the MW regime can be utilized to coherently control and manipulate the NV's spin degree of freedom [63, 64]. In this section, we introduce the technique of optically detected ESR, which has been the workhorse for studying the NV's response to the external perturbations discussed in Sec. 2.2 [100, 107, 119, 120]. Moreover, we discuss coherent manipulation pulse sequences used to investigate the relevant spin properties.

2.3.1. Magnetic dipole transitions

Magnetic dipole interactions are the dominant effect when an externally applied electromagnetic field couples to the NV spin in its ground state. As the ground state is an orbital singlet, i.e. it has no orbital magnetic dipole moment, a harmonic MW magnetic field $\boldsymbol{B}^{\mathrm{mw}}(t) = \boldsymbol{B}^{\mathrm{mw}} \cos(\omega_{\mathrm{mw}} t)$ couples only to the spin magnetic dipole moment, resulting in the time-dependent interaction Hamiltonian

$$\hat{\mathcal{H}}_{\mathrm{mw}}(t) = -\boldsymbol{B}^{\mathrm{mw}}(t) \cdot \hat{\boldsymbol{\mu}} \,, \tag{2.13}$$

where the magnetic dipole moment operator reads $\hat{\boldsymbol{\mu}} = -2\mu_B \hat{\boldsymbol{S}} = -h\gamma_{\mathrm{NV}} \hat{\boldsymbol{S}}$. This interaction Hamiltonian gives rise to transitions between an initial spin state $|i\rangle$ and a final spin state $|f\rangle$. Applying the rotating wave approximation in a reference frame rotating with angular frequency ω_{mw} around the spin quantization axis, we find that the system performs coherent oscillations between $|i\rangle$ and $|f\rangle$ with a 'Rabi frequency'

$$\Omega_{i,f} = \frac{1}{\hbar} |\langle f| -\boldsymbol{B}^{\mathrm{mw}} \cdot \hat{\boldsymbol{\mu}}|i\rangle| = \frac{1}{\hbar} |\boldsymbol{B}^{\mathrm{mw}} \cdot \boldsymbol{\mu}_{i,f}| \,. \tag{2.14}$$

Here, we introduced the magnetic dipole matrix elements

$$\boldsymbol{\mu}_{i,f} = \langle f|\hat{\boldsymbol{\mu}}|i\rangle = -2\mu_B \left\langle f \left| \hat{\boldsymbol{S}} \right| i \right\rangle \,, \tag{2.15}$$

which can easily be evaluated for given $|i\rangle$ and $|f\rangle$ by using the definition of the spin operator $\hat{\boldsymbol{S}}$ from Eq. (2.2). According to Eq. (2.14) and Eq. (2.15) we can deduce two
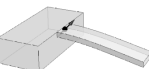
important aspects. First, from the magnetic dipole matrix elements $\boldsymbol{\mu}_{i,f}$ we can derive the selection rules for a magnetic dipole transition, i.e. transitions are only possible if electron spin quantum number changes by $\Delta m_s = \pm 1$. Second, only MW magnetic field components transverse to the NV axis yield non-zero Rabi frequencies for two different spin states and are consequently able to drive spin transitions in the NV ground state. Parallel components only induce time-varying shifts of the spin states, which can yield a parametric drive [46].

The magnetic dipole moment operator defined in Eq. (2.15) additionally allows us to infer information about the response of the spin transitions to MW fields with different polarizations. To that end, we define the Stokes vector $\boldsymbol{S} = (\mathcal{S}_0, \mathcal{S}_1, \mathcal{S}_2, \mathcal{S}_3)$ [121], whose components in the coordinate frame of the NV are given by

$$\mathcal{S}_0 = |\mu_x|^2 + |\mu_y|^2 \tag{2.16a}$$

$$\mathcal{S}_1 = |\mu_x|^2 - |\mu_y|^2 \tag{2.16b}$$

$$\mathcal{S}_2 = 2\,\mathrm{Re}(\mu_x^* \mu_y) \tag{2.16c}$$

$$\mathcal{S}_3 = -2\,\mathrm{Im}(\mu_x^* \mu_y) \ . \tag{2.16d}$$

Here, $\mu_{x,y,z}$ denote the components of the magnetic dipole matrix elements $\boldsymbol{\mu}_{i,f}$ for given $|i\rangle$ and $|f\rangle$. Note that the Stokes vector is normally used to determine the polarization of a MW field and defined in terms of the field components instead of the magnetic dipole matrix elements. However, to characterize the polarization response of a spin transition, we consider the magnetic dipole matrix elements. These allow us to deduce the MW field polarization that results in a maximum overlap in Eq. (2.14), i.e. the polarization that drives the transition the best.

The Stokes parameters $\mathcal{S}_{0,1,2,3}$ can be interpreted in the following way: While $\mathcal{S}_0$ determines the degree of polarization for a MW field to optimally drive the spin transition, $\mathcal{S}_1$, $\mathcal{S}_2$, and $\mathcal{S}_3$ characterize the polarization response of the transition. If $(\mathcal{S}_1^2 + \mathcal{S}_2^2 + \mathcal{S}_3^2)^{1/2} < \mathcal{S}_0$ the transition has a partially polarized response, otherwise it has a fully polarized response. In the latter case, the transition response is generally described in terms of a polarization ellipse [121]. The shape of this ellipse is thereby determined by polarization ellipse parameters $\mathcal{S}_{1,2,3}$ (see Fig. 2.5a). While $\mathcal{S}_1$ and $\mathcal{S}_2$ indicate a linear polarization in a horizontal/vertical and diagonal/anti-diagonal polarization plane, respectively, $\mathcal{S}_3$ denotes right/left circular polarization. The polarization ellipse parameters can be visualized on the Poincaré sphere [121] (see Fig. 2.5b), where the equator corresponds to purely linear polarization ($\mathcal{S}_1$- and $\mathcal{S}_2$-axes), whereas the poles corresponds to purely circular polarization ($\mathcal{S}_3$-axis). Consequently, if $\boldsymbol{\mu}_{i,f}$ only has real components, we find $\mathcal{S}_3 = 0$, which implies a linear polarization response. If the components of $\boldsymbol{\mu}_{i,f}$ have, however, imaginary arguments with the same magnitude, we find $\mathcal{S}_3 \neq 0$, which corresponds to a circular polarization response.

As an example we consider the $|0\rangle \leftrightarrow |\pm 1\rangle$ spin transitions in the NV ground state. Using Eq. (2.15) we can calculate the magnetic dipole matrix elements

$$\boldsymbol{\mu}_{0,\pm 1} = -\sqrt{2}\mu_B\big(1, \pm\mathrm{i}, 0\big) \ . \tag{2.17}$$

From these, Eq. (2.16) allows us to obtain the normalized Stokes vector, which reads

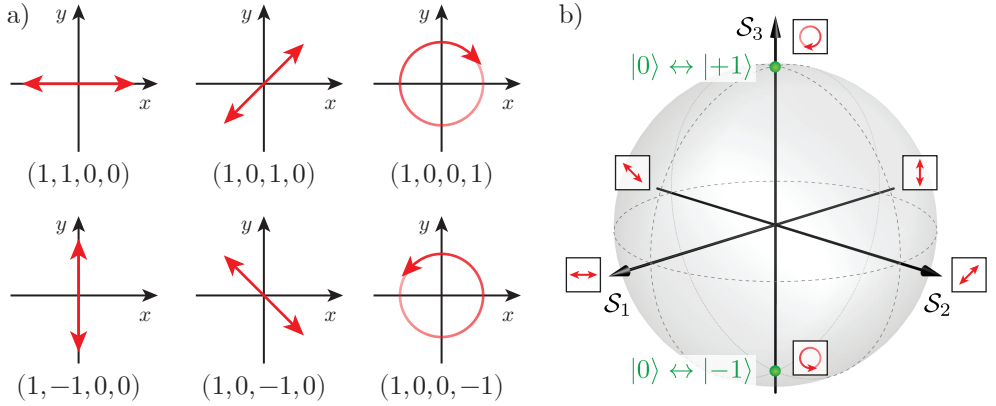$$\boldsymbol{S}_{0,\pm 1} = \big(1, 0, 0, \pm 1\big) \ . \tag{2.18}$$

Figure 2.5.: Polarization response and its visualization on the Poincaré sphere. a) Examples of Stokes vectors $\mathcal{S}$ and the corresponding polarization responses. While $\mathcal{S}_1$ and $\mathcal{S}_2$ characterize a linearly polarized response, $\mathcal{S}_3$ implies a circular polarization response. b) The Stokes parameters $\mathcal{S}_{1,2,3}$ corresponds to a point on or inside the Poincaré sphere. Any transition on the sphere has a fully polarized response, otherwise it has a partially polarized response. Antipodal points on the Poincaré sphere refer to orthogonal polarization responses. As an example, the green points illustrate the $|0\rangle \leftrightarrow |\pm1\rangle$ spin transitions, which have a purely circular polarization response.

As the only non-zero polarization ellipse parameter is $\mathcal{S}_3$, both transitions exhibit a purely circular polarization response, with $|0\rangle \leftrightarrow |-1\rangle$ having a left circularly polarized response and $|0\rangle \leftrightarrow |+1\rangle$ having a right circularly polarized response. Thus, the two spin transitions correspond to MW driving field polarizations located on opposite poles of the Poincaré sphere (see Fig. 2.5b).

2.3.2. Electron spin resonance

By using MW magnetic fields we can address and manipulate the NV's spin transitions, which will ultimately allow us to characterize the fundamental properties of the NV spin and its environment. Typically, these studies are done by the general manipulation pulse sequence illustrated in Fig. 2.6a. First, the NV spin is initialized in $|0\rangle$ by optical means, i.e. a green laser pulse (see Sec. 2.1.3). Next, a MW magnetic field is used to perform spin manipulation. Finally, the spin state is read out optically, which also reinitializes the NV spin into $|0\rangle$ again. The specific MW manipulation sequences used for spin characterization are discussed in the following.

To identify the spin transitions in the NV ground state we utilize optically detected pulsed ESR (see Fig. 2.6b). To that end, the manipulation pulse sequence consists of a MW pulse with fixed duration, whose frequency $\omega_{\mathrm{mw}}/2\pi$ is swept across the region of interest [71, 122] (for a maximum contrast, the pulse length should induce a full transition between the spin states, which is the case for a duration t_π, compare to Sec. 2.3.3). When the MW frequency is near resonance with a specific NV spin transition, the MW field induces coherent oscillations between the involved states. The consequent change in spin populations can then be read out by the spin-dependent
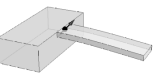
fluorescence of the NV. In the resulting ESR spectrum, we typically observe six hyperfine transition dips, which are labeled according to their spin quantum numbers. Here, an externally applied static magnetic field lifts the zero-field degeneracy of the involved states according to the Zeeman effect (see Fig. 2.3a). The corresponding level scheme is depicted in Fig. 2.6c.

Note that for the described 'pulsed ESR' technique the laser is switched off during MW manipulation in order to eliminate laser power induced broadening, while MW power is chosen to be low to minimize MW induced power broadening [122]. This procedure ensures that one can resolve the NV spin hyperfine structure, as the linewidth of the transitions is then limited by inhomogeneous broadening. One can also perform continuous wave (CW) ESR spectroscopy, where the laser illumination and the MW manipulation are constantly applied. This technique, however, only allows for the observation of inhomogeneously broadened linewidths when all power levels are carefully adjusted and will result in artificially broadened linewidths otherwise.
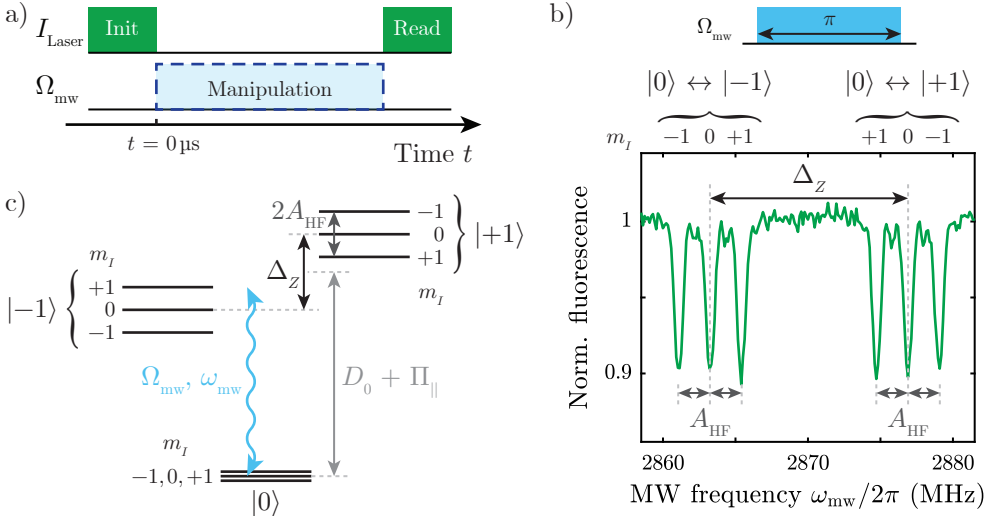

Figure 2.6.: MW manipulation and ESR. a) General pulse sequence employed for MW manipulation of the NV spin. In between the spin initialization and readout a specific manipulation sequence (symbolically represented by the blue box) is applied. We present these sequences for each of the manipulation techniques in the corresponding figures. b) Pulsed ESR allows us to selectively probe and resolve the hyperfine transitions. To that end, the MW manipulation field with amplitude Ω_{mw} is switched on for a certain period of time (typically $\tau_\pi = \pi/\Omega_{\mathrm{mw}}$, corresponding to a '$\pi$-pulse', see Sec. 2.3.3) while we vary the MW frequency $\omega_{\mathrm{mw}}/2\pi$. In the resulting spectrum (here obtained at $B_\parallel \approx 2.5\,\mathrm{G}$) we observe a pair of resonances with three hyperfine transitions each. The pair corresponds to the electronic spin transitions $|0\rangle \leftrightarrow |\pm1\rangle$ exhibiting a subdivision due to the hyperfine structure as illustrated in c). c) Level diagram of the NV ground state under a non-zero axial magnetic field and neglecting the quadrupolar interaction (see Sec. 2.1.2). The transverse MW manipulation field (blue) drives the hyperfine transitions $|0, m_I\rangle \leftrightarrow |\pm1, m_I\rangle$ with $m_I = 0, \pm1$.

2.3.3. Coherent spin manipulation

Characterizing the NV's spin transitions via ESR is crucial for more complex spin manipulation measurement protocols, which require resonant driving of these transitions [123–125]. Here, we focus on the three most common coherent manipulation techniques, specifically Rabi, Ramsey, and spin echo spectroscopy.

Rabi oscillations

Initializing the NV spin into a specific superposition state requires the definition of quantum coherent operations on the spin. The two most important rotation operations, the π- and $\pi/2$-pulse, can be defined by the Rabi pulse sequence. As described previously, transverse MW fields quasi-resonant with a transition in the NV ground state manifold can induce population transfer between the two coupled spin states, if the respective transition is magnetic dipole-allowed, i.e. $\Delta m_s = \pm 1$. The dynamics of the population transfer, however, depend on both the amplitude and duration of the MW pulse. When the MW field amplitude is fixed while its duration is varied, the spin populations of the two states exhibit coherent oscillations, a phenomenon known as Rabi oscillations [126].

In Fig. 2.7a we present coherent Rabi oscillations driven on the $|0\rangle \leftrightarrow |-1\rangle$ transition and measured with the corresponding manipulation sequence. For this measurement, we applied a parallel magnetic field $B_\parallel = 1.82\,\mathrm{G}$ to split $|-1\rangle$ and $|+1\rangle$[9]. In the present case of resonant driving, the spin population oscillates harmonically between the two states with frequency $\Omega_{\mathrm{mw}}/2\pi$. Applying the MW field for an interaction time $\tau_\pi = \pi/\Omega_{\mathrm{mw}}$ completely inverts the spin population from $|0\rangle$ to $|-1\rangle$ – a situation denoted as a 'π-pulse'. Similarly, for a '$\pi/2$-pulse', the MW field is applied for $\tau_{\pi/2} = \pi/(2\Omega_{\mathrm{mw}})$, resulting in an equal superposition of both coupled states. Note that driving the system slightly out of resonance, i.e. with a detuning $\delta = \omega_{\mathrm{mw}} - \omega_{0,-1} \neq 0$, results in faster oscillations at the effective Rabi frequency $\Omega = (\Omega_{\mathrm{mw}}^2 + \delta^2)^{1/2}$, with less contrast [114]. Moreover, as seen in Fig. 2.7a Rabi oscillations are damped, which is a result environmental fluctuations coupling to the NV spin. The interactions of the NV spin with its environment can be characterized by two time constants, the inhomogeneous dephasing time T_2^* and the homogeneous coherence time T_2, which we introduce in the following.

Free induction decay

To study the coherence properties of a single NV spin[10], we first consider a superposition of two states, e.g. of $|0\rangle$ and $|-1\rangle$. Due to the Zeeman interaction, the time evolution of this superposition is highly sensitive to changes in the local magnetic field, characterized by the accumulation of a relative phase between the two states. Consequently, time-varying environmental fluctuations, e.g. induced by the dynamics of the nuclear spin bath surrounding the NV spin, will randomize this relative phase, a process often referred to as transverse relaxation or decoherence.

---

[9]Alternatively one can apply a circularly polarized MW field to selectively address either the $|0\rangle \leftrightarrow |-1\rangle$ or $|0\rangle \leftrightarrow |+1\rangle$ transition even at zero magnetic field (see Sec. 2.3.1).

[10]In our case we investigate a typical shallow, single NV in a nanostructured, type-IIa diamond (see Sec. 3.1).
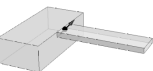
To characterize the decoherence mechanism we employ Ramsey or free induction decay spectroscopy [128]. The underlying pulse sequence is presented in Fig. 2.7b. First, the system is initialized into a superposition state by a $\pi/2$-pulse, after which the spin is left to evolve freely for a duration τ. Finally, we project the spin state into a measurable population difference by a second $\pi/2$-pulse, which allows us to analyze the accumulated phase. The experimental result obtained on a hyperfine resolved transition of a single NV shows a beating of frequencies with a Gaussian decay envelope. The observed beating is caused by the hyperfine coupling of the NV
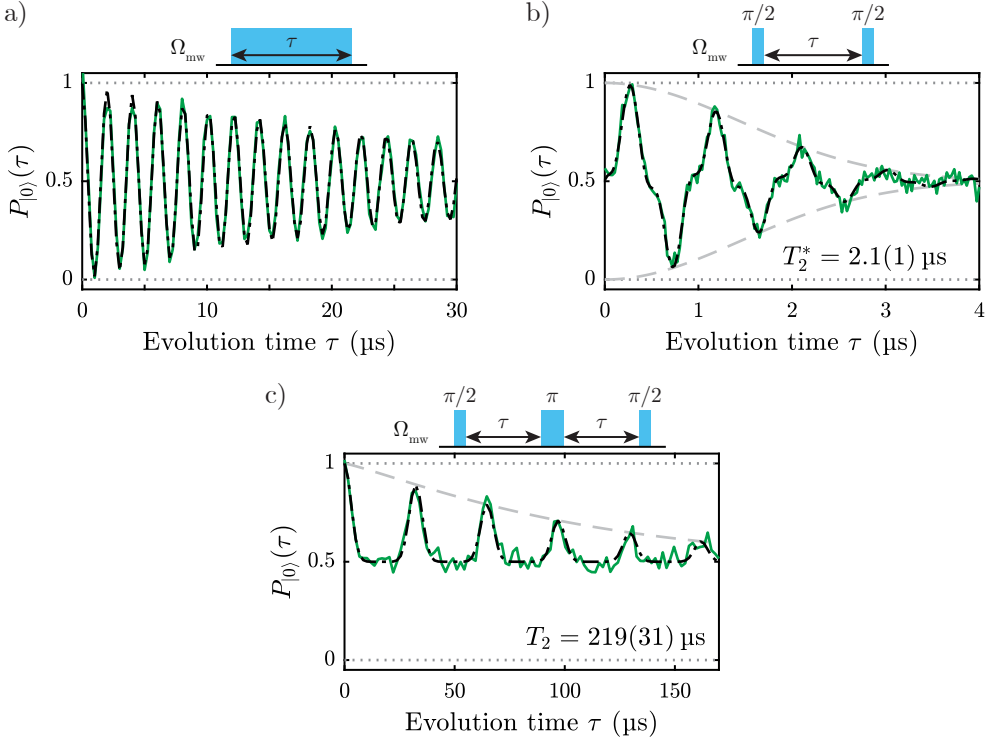

Figure 2.7.: Coherent MW manipulation of the NV spin. a) Varying the duration τ of the MW pulse while choosing the MW frequency on resonance with one of the transition frequencies allows one to drive coherent Rabi oscillations. For the present case we extract a Rabi frequency $\Omega_{\mathrm{mw}}/2\pi = 492(8)\,\mathrm{kHz}$ and a decay $T_{\mathrm{Rabi}} = 32(3)\,\mu\mathrm{s}$ from fitting an exponentially damped single harmonic. b) To determine the inhomogeneous dephasing time T_2^* we employ Ramsey spectroscopy. Two MW $\pi/2$-pulses are applied with a varying evolution time τ in between. Using a Gaussian decay envelope we obtain $T_2^* = 2.1(1)\,\mu\mathrm{s}$. c) For a spin echo an intermediate, refocusing π-pulse is inserted into the Ramsey sequence and the inter-pulse delays τ before and after this π-pulse are varied simultaneously. We apply a moderate magnetic field of $B_\parallel = 30\,\mathrm{G}$ to resolve periodic collapses and revivals of the signal, which are attributed to the precession of the $^{13}\mathrm{C}$ nuclear spin bath. Fitting the data with an appropriate model results in $T_2 = 219(31)\,\mu\mathrm{s}$ for an exponential decay with exponent $n = 1.2(3)$ [127].

electron spin to the ^{14}N nuclear spin, while the decay is attributed to both spin-spin relaxation and inhomogeneous effects, i.e. different static field conditions during each measurement cycle. Averaging over the subsequent variable phase accumulations ultimately results in the observed decay. The characteristic timescale for this process is the inhomogeneous[11] dephasing time T_2^*, which quantifies the decoherence process under free (undriven) spin dynamics. In a weak parallel magnetic field of $B_\parallel = 1.82\,\text{G}$, the NV under study exhibits $T_2^* = 2.1(1)\,\mu\text{s}$, limited by dipolar interactions between the NV spin and the slow-varying spin bath of ^{13}C nuclei [128].

Spin echo spectroscopy

To mitigate the effect of slow environmental fluctuations and to remove the inhomogeneous contribution to decoherence, spin echo spectroscopy can be employed. This allows us to determine the homogeneous coherence time T_2, the characteristic timescales of spin-spin relaxation.

For a spin echo sequence [112, 117, 123] an additional π-pulse is inserted in the Ramsey sequence, and positioned symmetrically between the two $\pi/2$-pulses (see Fig. 2.7c). The π-pulse inverts the sign of the relative phase accumulated during the second free evolution interval. Thus, the pulse sequence leads to a refocusing and cancellation of the net accumulated phase, in particular of the random phase shift caused by slowly varying noise components. A typical spin echo signal in a moderate magnetic field (here $B_\parallel = 30\,\text{G}$) shows periodic revivals at a rate set by the Larmor precession frequency for the ^{13}C nuclear spins, $\gamma_\text{C} = 1.07\,\text{kHz/G}$ [117]. This can be understood by considering the NV's phase accumulation. When the evolution time τ matches half of the Larmor oscillation period $1/(2\gamma_\text{C}B_\parallel)$ of the ^{13}C nuclear spin, the NV's accumulated phase is maximized, resulting in the fast initial collapse of the NV's coherence. For $\tau = 1/(\gamma_\text{C}B_\parallel)$ the accumulated phase is minimized due to the refocusing, which leads to a revival of the spin coherence. This process is repeated iteratively, so that the ^{13}C precession induces periodic decorrelation and rephasing of the nuclear spin bath, causing the observed collapses and revivals. The overall decay of the revivals allows us to extract the NV's homogeneous coherence time T_2. To that end, we fit our data using an appropriate fit function [127] including a damping exponent n. We find $T_2 = 219(31)\,\mu\text{s}$ and $n = 1.2(3)$. Besides the paramagnetic bath fluctuations, T_2 is also limited by environmental electric field noise originating from the diamond surface. Consequently, T_2 is highly dependent on the diamond sample and additionally on the depth of the NV from the diamond surface. At room temperature the maximum reported values for T_2 reach up to 2 ms in isotopically purified diamond [53, 130].

Long coherence times are highly desired in quantum technologies. Dynamical decoupling techniques [32–34] can further suppress the decoherence processes and thereby elongate the coherence time. However, these techniques suffer from experimental complexities and are only severely compatible with quantum gate operations. Alternatively, the decoherence process can be mitigated by using dressed spin states, i.e. by driving the spin transitions continuously, as we will see in Chap. 3.

---

[11]For a single spin, T_2^* is also referred to as time-averaged dephasing time [129].
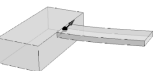
Spin lattice relaxation

Besides the transverse relaxation mechanism, the NV spin also undergoes longitudinal relaxation, which influences the level populations by induced spin flips. More precisely, such an energy relaxation process describes the decay of a polarized spin state into a thermally mixed state. In case of the NV spin, the decay is mainly induced by interactions with lattice phonons, so that this process is referred to as spin-lattice relaxation[12]. The corresponding timescale is the spin-lattice relaxation time T_1.

To determine the relaxation time T_1 of the NV's three level ground state, we need to take all possible relaxation channels between the spin states into account [131]. In particular, the transition rates between both $|0\rangle \leftrightarrow |\pm1\rangle$ and $|-1\rangle \leftrightarrow |+1\rangle$ have to be considered and are given by Γ and γ, respectively (see Fig. 2.8a). The population dynamics are then described in terms of rate equations, i.e. the population change in each state corresponds to the sum of rates into and out of the state weighted by the current populations [131]. Based on this relaxation model, T_1 for the three-level system of the NV ground state is found as

$$\frac{1}{T_1} = 3\Gamma + \gamma \,. \tag{2.19}$$

This definition of the relaxation time ultimately sets the upper limit for the homogeneous coherence $T_2 \leq 2T_1$ of any superposition spin state in the NV ground state.
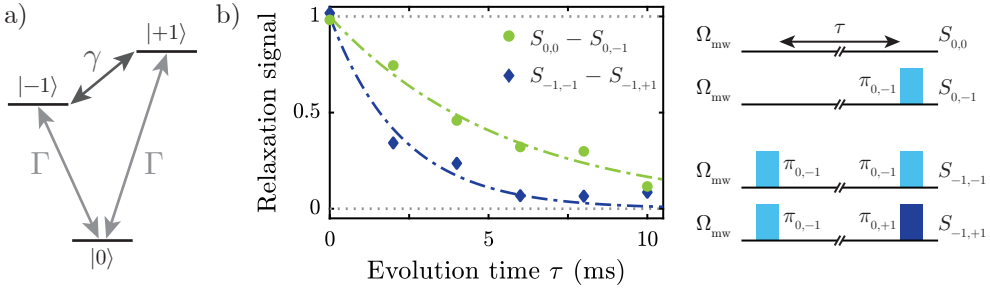

Figure 2.8.: Relaxation of the NV spin. a) The transition rates in the ground state are denoted by Γ ($|0\rangle \leftrightarrow |\pm1\rangle$ transitions) and γ ($|-1\rangle \leftrightarrow |+1\rangle$ transition). While Γ is mainly sensitive to magnetic field noise, the transition rate γ is sensitive to electric field noise. b) The complete measurement sequence to determine the relaxation time T_1 of the NV's three-level system consists of four parts as depicted on the right. To extract the two transition rates Γ and γ, various $\pi_{j,k}$-pulses between states $|j\rangle$ and $|k\rangle$ ($j, k = 0, \pm1$, but $j \neq k$) are used to initialize in $|i\rangle$ and read out the population in $|r\rangle$, giving the signal $S_{i,r}$. The resulting relaxation signals offer two different population decays, which are fitted with a corresponding exponential model [131]. From the fits we obtain $\Gamma = 60(14)\,\text{Hz}$ and $\gamma = 190(81)\,\text{Hz}$, resulting in $T_1 = 2.7(9)\,\text{ms}$.

---

[12]Note that the interaction with lattice phonons is not the only mechanism contributing to longitudinal relaxation, as magnetic and electric noise at the frequency of the transition between two states can induce relaxation as well.

The right part of Fig. 2.8b presents the manipulation pulse sequences to extract the two transition rates Γ and γ. The complete measurement consists of two sets of pulse sequences. Using various resonant π-pulses, the pulse sequences probe the population in $|r\rangle$ after the system was initially prepared in $|i\rangle$ and freely evolved for time τ, yielding the signal $S_{i,r}$. Subtracting the two signals within a measurement set results in the relaxation signal, which we fit with an exponential decay [131]. In the present case of $B_\| = 1.82\,\mathrm{G}$, we find the transition rates $\Gamma = 60(14)\,\mathrm{Hz}$ and $\gamma = 190(81)\,\mathrm{Hz}$. Using Eq. (2.19) finally results in $T_1 = 2.7(9)\,\mathrm{ms}$. Note that due to its phonon-assisted nature spin-lattice relaxation exhibits a strong temperature dependence, reaching T_1 values up to $\approx 1\,\mathrm{min}$ at cryogenic temperatures [132].

2.4. Interaction with time-dependent strain fields

The discussed MW spin manipulation is limited by the magnetic dipole selection rules, which only allow us to address the $|0\rangle \leftrightarrow |\pm 1\rangle$ spin transitions in the NV ground state. Thus, coherent transitions between $|-1\rangle \leftrightarrow |+1\rangle$ are difficult to access using conventional magnetic resonance techniques. In recent years mechanical motion has been investigated to overcome this limitation and to coherently manipulate the NV's spin degree of freedom through strain coupling [52, 102, 133, 134]. In particular, hybrid spin-mechanical systems have emerged as an attractive platform to exploit the quantum-coherent spin-mechanical interaction [65, 66].

According to Eq. (2.5) strain mixes $|-1\rangle$ and $|+1\rangle$ states. Applying time-varying strain, e.g. induced by the fundamental mode of a diamond cantilever, to an embedded NV, the state mixing is modulated dynamically, leading to a coupling between $|-1\rangle$ and $|+1\rangle$ [52]. In the case of a cantilever, driving spin transitions between $|-1\rangle$ and $|+1\rangle$ requires the Zeeman splitting Δ_Z to match the frequency of the mechanical strain field, $\omega_\mathrm{m}/2\pi$. Note that Eq. (2.5) is independent of the nuclear spin, i.e. strain only couples states with the same nuclear spin projection m_I (see Fig. 2.9a).

To verify coherent mechanical spin manipulation with $\Delta m_s = \pm 2$ we demonstrate strain-driven Rabi oscillations between $|-1\rangle \leftrightarrow |+1\rangle$ for a given hyperfine manifold (here $m_I = +1$, see Fig. 2.9a). The employed pulse sequence is illustrated in Fig. 2.9b. After optical initialization of the NV spin, we swap the $|0, +1\rangle \leftrightarrow |-1, +1\rangle$ populations by a resonant π-pulse to prepare the system in $|-1, +1\rangle$. Then, the spin evolves for a variable time τ under the presence of the resonant strain field, before another π-pulse allows us to optically read out the spin population in $|-1, +1\rangle$. Fig. 2.9c shows the resulting strain-induced, coherent Rabi oscillations with $\Omega_\mathrm{m}/2\pi = 1.14(1)\,\mathrm{MHz}$ and hardly any damping over the $30\,\mu\mathrm{s}$ observation time [52]. We note that due to the long ring-up and ring-down times of the mechanical motion, it is experimentally not possible to switch on and off the mechanical drive. Typical values of ring-down times are $\approx 100\,\mu\mathrm{s}$, far exceeding the timescales of our applied pulse sequences ($t_\pi \approx 500\,\mathrm{ns}$). This, in combination with the non-zero length of the MW pulses, reduces the contrast of the mechanical Rabi oscillations to $\approx 80\,\%$ due to incomplete population transfer during the initial and final π-pulses.
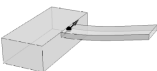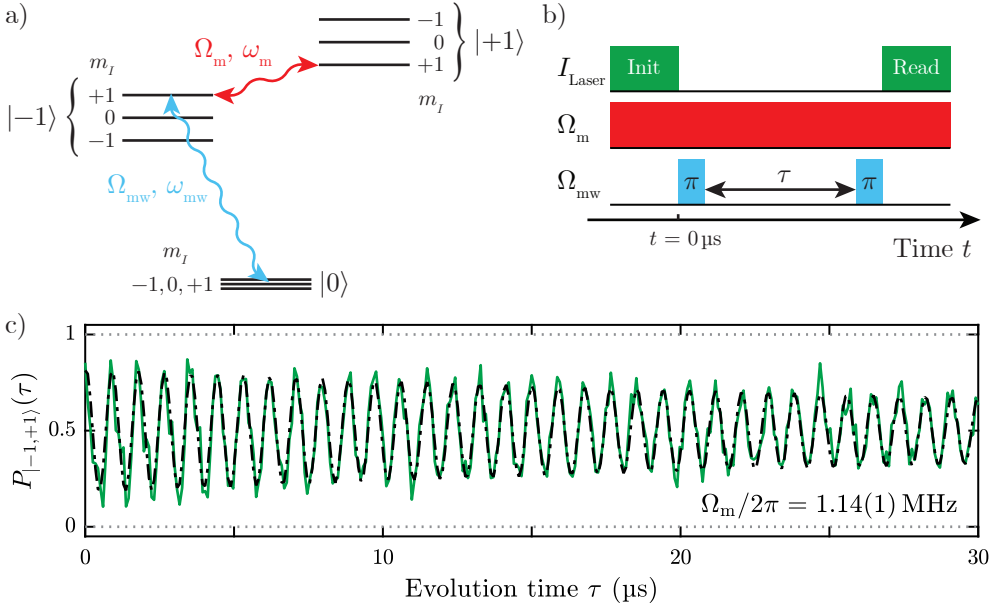
Figure 2.9.: Coherent spin manipulation with strain fields. a) While transverse MW fields coherently drive transitions between $|0\rangle \leftrightarrow |\pm1\rangle$ (blue), time-dependent transverse strain fields coherently address transitions between $|-1\rangle \leftrightarrow |+1\rangle$ (red). Note that in both cases only states with the same nuclear spin projection m_I are driven. b) Pulse sequence employed to demonstrate strain-induced coherent spin drive in terms of Rabi oscillations in the $|-1\rangle \leftrightarrow |+1\rangle$ manifold. For initialization and readout of the spin, a π-pulse between $|0\rangle$ and $|-1\rangle$ is used. c) Mechanically driven Rabi oscillations between $|-1\rangle \leftrightarrow |+1\rangle$ mediated by transverse strain. The fit yields a Rabi frequency $\Omega_{\mathrm{m}}/2\pi = 1.14(1)\,\mathrm{MHz}$ and a decay time $T_{\mathrm{Rabi}} = 48(10)\,\mu\mathrm{s}$.

Having direct access to the magnetic dipole forbidden $|-1\rangle \leftrightarrow |+1\rangle$ transition opens the door to several interesting operations. For example, this enables new types of spin-based sensing or even enhances current magnetometry protocols [135, 136]. Moreover, combining strain driving with standard MW spin manipulation allows us to address all three spin transitions in the NV ground state simultaneously and coherently, thereby forming a closed '∇-system' [49]. Such a system, which is at the heart of this thesis, may find particular value in quantum-assisted sensing and quantum optomechanics and will be discussed extensively in the following chapters.

3. Coherence protection under closed-contour driving

Three-level quantum systems are an indispensable platform in quantum optics. Extending the well-studied capabilities of two-level systems, three-level systems give rise to diverse physical phenomena based on the interference between different, simultaneously driven excitation pathways [137, 138]. Typically, two out of three transitions are addressed by coherent driving fields, leading to effects like coherent population trapping [21, 22], electromagnetically induced transparency [23], and STIRAP [24, 25]. These phenomena rely on the special properties of the eigenstates of the driven system, the so-called dressed states. In the mentioned examples the crucial dressed states are formed by mixing two of the three undriven states.

Introducing an additional third driving field and thereby addressing all available transitions coherently extends the diversity of three-level systems further and gives rise to previously inaccessible effects [49]. Specifically, in such a closed-contour interaction scheme, novel system dynamics arise caused by interfering pathways. These interferences depend on the relative phase of the driving fields, which can be reduced to a single parameter, the global phase Φ [139]. The global phase thereby fully determines the system's dynamics and controls the quantum interference phenomena [49, 140, 141]. These effects can, in turn, be described by the eigenstates of the fully driven three-level system, i.e. dressed states, which will turn out to be equal, coherent superpositions of all three undriven spin states.

The properties of three-level dressed states emerging from closed-contour driving remain, however, largely unexplored. Studying these dressed states is severely complicated in most experimental systems due to prevailing selection rules attributed to the transitions. As a consequence of symmetry, not all of the three transitions adhere to the same selection rules, i.e. they cannot all be dipole-allowed for the same type of driving field. Systems combining electric and magnetic dipole transitions overcome this limitation, but their experimental observation of the coherent dressed-states' dynamics was limited by prevalent dephasing [142–146]. This was overcome in a recent demonstration of the coherent circulation of MW photons in three coupled superconducting qubits [147]. Yet this study does neither offer a complete characterization of the system's dynamics nor a systematic analysis of the coherence times of the occurring dressed states.

In this chapter, we introduce the experimental methods we employed to implement three-level dressed states in a closed-contour interaction scheme and provide a thorough characterization of their properties [114, 148]. To that end, we exploit a unique combination of coherent MW and strain driving to realize and study such dressed states in the '∇-system' of the NV's $S = 1$ ground state. We start with a brief overview of the experimental setup and the measurement techniques before we present a detailed study of the influence of the global phase on the coherent dynamics
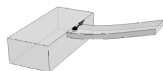
of the system and the remarkable properties of the dressed states. Most significantly, owing to the nature of the dressed states, the global phase serves as a powerful handle to protect them from environmental noise and thereby prolongs their coherence times by nearly two orders of magnitude compared to the NV's inhomogeneous dephasing time, even for moderate continuous driving strengths. Thus, dressed states emerging from closed-contour interaction driving constitute a novel dynamical decoupling approach with interesting perspectives for future technology applications.

The results presented here have been published in [148].

3.1. Experimental implementation

Our experimental approach to realizing three-level dressed states that emerge under closed-contour interaction is based on individual NV spins in a hybrid spin-mechanical system (see Fig. 3.1a). The sample under investigation for all experiments within the scope of this thesis is an electronic grade diamond (Element Six) implanted with ^{14}N (dose 10^9 ions/cm^2, energy $12\,\text{keV}$) and subsequently annealed using a high-temperature annealing process [149]. Hence, implanted NV centers are located at
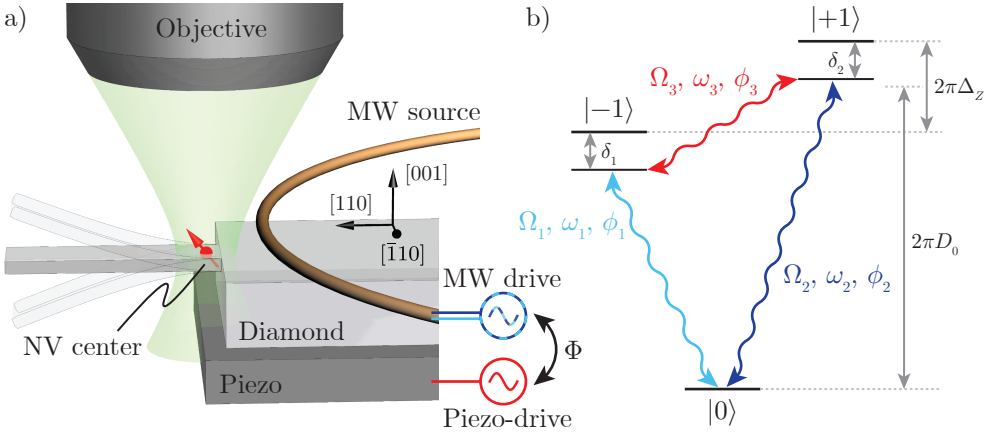

Figure 3.1.: Realization of dressed states under closed-contour driving in the $S = 1$ NV ground state. a) Schematic of the experimental setup. The single NV center under investigation (red) is embedded in a diamond cantilever. To enable strain driving of the NV spin a piezoelectric actuator drives the cantilever resonantly. A nearby wire is used for MW delivery. Strain and MW manipulation fields are generated by a function generator and a MW signal generator and are mutually phase-locked to ensure control over the global phase Φ. To optically initialize and read out the NV spin we use a confocal microscope. b) The electronic spin sublevels of the NV ground state form a three-level system. In an external magnetic field, the Zeeman splitting Δ_Z lifts the degeneracy of $|-1\rangle$ and $|+1\rangle$, so that all spin transitions can be individually and coherently addressed. MW fields drive the $|\Delta m_s| = 1$ transitions (blue), while strain is used to address the $|\Delta m_s| = 2$ transition (red). The manipulation fields have frequency $\omega_i/2\pi$, amplitude (Rabi frequency) Ω_i, and phase ϕ_i ($i = 1, 2, 3$).

a depth of $\approx 17(6)\,\mathrm{nm}$ below the surface, as estimated from implantation profiles using the software SRIM [150]. To structure cantilevers with dimensions in the range of $0.5(2) \times 3.5(1) \times (15-45)\,\mathrm{\mu m}^3$ in thickness, width, and length, we use well-established techniques for diamond fabrication [151]. All underlying steps to fabricate such diamond cantilevers are discussed in great detail elsewhere [114].

To optically address single NV centers we use a homebuilt confocal microscope setup [52, 103, 152]. It allows us to readily initialize the NV spin state via optical pumping from a laser, whereas we collect the spin-dependent red NV fluorescence for optical spin state readout [55]. For a detailed description of the microscope setup we refer the reader to [114]. Additionally, three pairs of magnetic coils allow us to apply an external magnetic field with full vector control (see App. A.1.1).

Manipulation of the NV spin is achieved through two different methods. First, a nearby gold wire with a diameter of $\approx 30\,\mathrm{\mu m}$ close to the NV under study acts as a near-field MW source. The delivered MW magnetic fields are generated by a MW circuit (see App. A.1.2) and allow us to drive transitions between electronic spin levels with $|\Delta m_s| = 1$. Second, resonantly driving the utilized cantilever at its eigenfrequency[1] induces a time-varying strain field, which is controlled by a piezoelectric transducer. To that end, we apply an external static magnetic field to bring the Zeeman splitting of $|-1\rangle$ and $|+1\rangle$ into resonance with the mechanical driving field while we maximize strain coupling by investigating a single NV close to the clamping point of the cantilever [102, 103]. This hybrid approach allows us to individually control the amplitudes, relative phases, and frequencies of all driving fields. All measurements present in this work are performed under ambient conditions.

3.2. Dressed states under closed-contour interaction

To dress the $S = 1$ electronic spin ground state of a single NV center in a closed interaction contour, we combine both spin manipulation techniques discussed above (see Fig. 3.1b). Specifically, while MW magnetic fields address the $|0\rangle \leftrightarrow |\pm 1\rangle$ transitions coherently [63, 64], strain coherently drives the nominally magnetic dipole-forbidden $|-1\rangle \leftrightarrow |+1\rangle$ transition [52, 134]. As strain only couples hyperfine levels with the same nuclear spin quantum number m_I, we restrict ourselves to the nuclear spin subspace with quantum number $m_I = +1$ for experimental simplicity [52].

To meet the requirement that the Zeeman splitting Δ_Z of $|-1\rangle$ and $|+1\rangle$ is in resonance with the driving frequency $\omega_3/2\pi = 5.8679\,\mathrm{MHz}$ of the cantilever under study, i.e. $\Delta_Z = \omega_3/2\pi$, we apply an axial magnetic field $B_\parallel = 1.82\,\mathrm{G}$. Correspondingly, the frequencies of the two MW fields are set to $\omega_{1,2} = 2\pi D_0 \pm \omega_3/2$. The amplitudes (Rabi frequencies) of all fields are controlled by either the amplitude of the piezo excitation (Ω_3) or the MW power delivered to the MW source ($\Omega_{1,2}$). While Ω_3 remains constant throughout our experiments[2], we can control the MW field amplitudes $\Omega_{1,2}$ arbitrarily, which will be a fundamental requirement for the following chapters. Additionally,

---

[1]For all the experiments presented in this thesis we use a cantilever with dimensions $0.5(2) \times 3.5(1) \times 43(2)\,\mathrm{\mu m}^3$ for thickness, width, and length, which results in a measured eigenfrequency of $5.8679(1)\,\mathrm{MHz}$.

[2]This is a direct consequence of the sizable quality factor of our cantilever (≈ 500), which prevents us to switch on and off the mechanical drive on the required ns timescale (see Sec. 2.4).
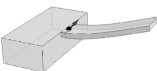
all three fields are generated in a phase-locked manner, allowing us to tune the relative phases $\phi_{1,2,3}$ and thereby providing full, coherent control of the closed-contour system.

Considering the combined action of the three driving fields, the dynamics of the closed-contour interaction scheme in an appropriate rotating frame [139, 153] are described by the time-independent Hamiltonian

$$\hat{\mathcal{H}}_0/\hbar = \frac{1}{2} \begin{pmatrix} 2\delta_1 & \Omega_1 & \Omega_3\,\mathrm{e}^{\mathrm{i}\Phi} \\ \Omega_1 & 0 & \Omega_2 \\ \Omega_3\,\mathrm{e}^{-\mathrm{i}\Phi} & \Omega_2 & 2\delta_2 \end{pmatrix} , \tag{3.1}$$

if the three-photon resonance $\omega_1 + \omega_3 = \omega_2$ is fulfilled (see [114, 148] for a detailed derivation). Hamiltonian $\hat{\mathcal{H}}_0$ is expressed in the basis $\{|-1\rangle, |0\rangle, |+1\rangle\}$ and $\delta_{1,2}$ are the detunings of the MW driving fields from the $|0\rangle \leftrightarrow |\pm1\rangle$ transitions (see Fig. 3.1b). Importantly, the resulting spin dynamics are dependent on the well-defined, gauge-invariant global phase $\Phi = \phi_1 + \phi_3 - \phi_2$, where ϕ_i $(i = 1, 2, 3)$ are the individual driving field phases. In the following, we will focus on the case of resonant and symmetric driving, i.e. $\delta_{1,2} = 0$ and $\Omega_{1,2,3} \equiv \Omega$. Here, we can readily diagonalize $\hat{\mathcal{H}}_0$, resulting in the dressed eigenstates

$$|\Psi_k\rangle = \frac{1}{\sqrt{3}} \left(\mathrm{e}^{\mathrm{i}(\Phi/3 - k\varphi_0)}, 1, \mathrm{e}^{-\mathrm{i}(\Phi/3 - k/\varphi_0)} \right) , \tag{3.2}$$

with corresponding eigenenergies

$$E_k/\hbar = \Omega \cos(\Phi/3 - k\varphi_0) , \tag{3.3}$$

where $\varphi_0 = 2\pi/3$ and $k = 0, \pm1$. Note that each of the dressed eigenstates is an equal superposition of the three NV spin states, i.e. the dressed states carry zero angular momentum and are, therefore, expected to be insensitive to magnetic fields to first order, as long as no degeneracy is present.

To provide a baseline for our subsequent studies of the three-level dressed states, we first characterize the system's dynamics under the closed-contour interaction. To that end, we measure the time evolution of the NV spin population for various values of Φ with $\Omega/2\pi = 500\,\mathrm{kHz}$ using the experimental sequence shown in Fig. 3.2b. For each value of Φ, a green laser pulse initializes the NV spin in $|\psi(\tau = 0)\rangle \equiv |0\rangle$, which can be expressed as equal superposition of all three dressed states,

$$|\psi(\tau = 0)\rangle = (|\Psi_{-1}\rangle + |\Psi_0\rangle + |\Psi_{+1}\rangle)/\sqrt{3} . \tag{3.4}$$

We then let the system evolve under the influence of the three driving fields for a variable evolution time τ. To monitor the time evolution

$$|\psi(\tau)\rangle = \mathrm{e}^{-\mathrm{i}\hat{\mathcal{H}}_0\tau/\hbar} |\psi(0)\rangle , \tag{3.5}$$

we finally apply an additional green laser pulse to read out the final population in $|0\rangle$,

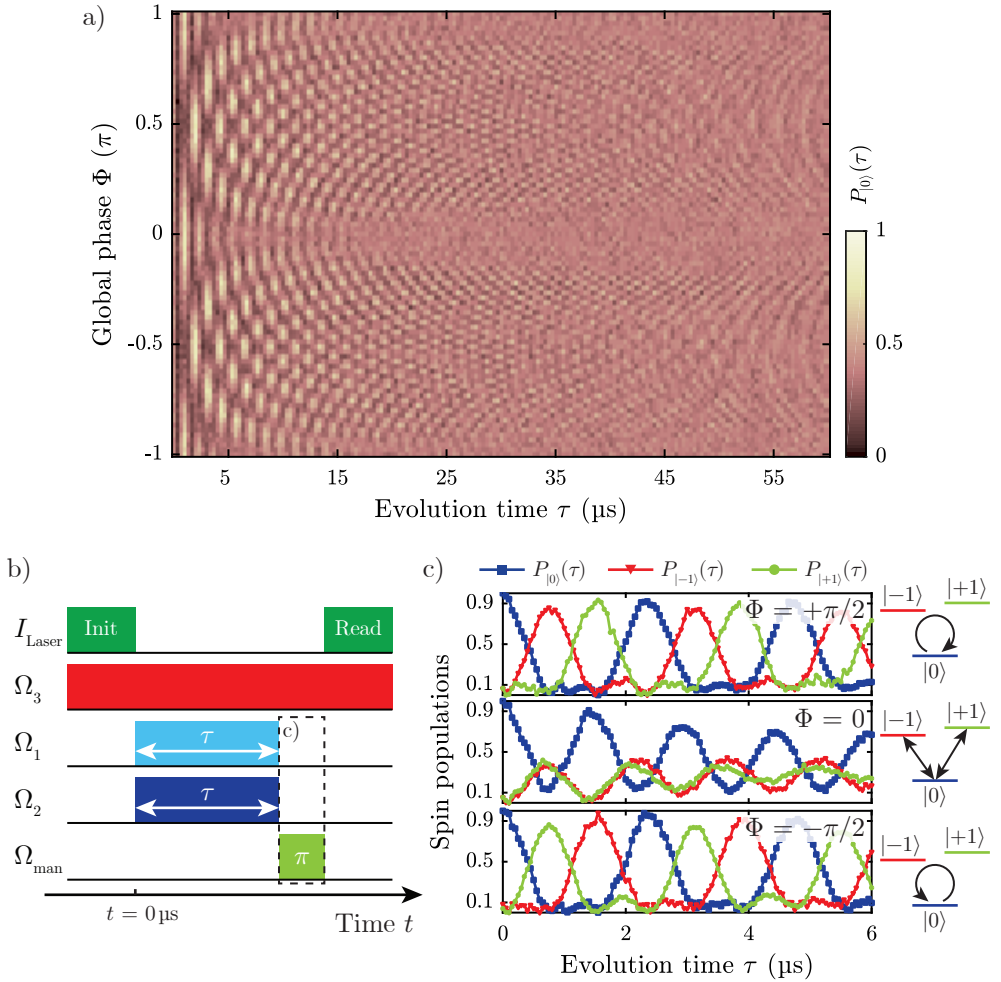$$P_{|0\rangle}(\tau) = |\langle 0|\psi(\tau)\rangle|^2 . \tag{3.6}$$

Figure 3.2.: Phase-dependent spin dynamics under closed-contour driving. a) Time evolution of the population $P_{|0\rangle}(\tau)$ as a function of global phase Φ after initialization in $|0\rangle$. Quantum interferences induced by the closed-contour driving cause a periodic evolution of $P_{|0\rangle}(\tau)$. The interference pattern shows a strong Φ-dependence of period and decay times. b) Pulse sequence used for studying the closed-contour dynamics. After initialization in $|0\rangle$, the MW fields are switched on instantaneously. The system then evolves under the presence of all fields for a time span τ, before the population in $|0\rangle$ is read out. An additional π-pulse (dashed box) is required to read out the populations in $|-1\rangle$ or $|+1\rangle$ shown in c). c) Time evolution of the $|m_s\rangle$ populations, $P_{|m_s\rangle}(\tau)$ with $m_s = 0, \pm 1$ for $\Phi = \pi/2, 0$, and $-\pi/2$ (top, middle, and bottom, respectively). For $\Phi = \pi/2$ $(-\pi/2)$ the population circulates clockwise (counterclockwise) in the three-level system indicating non-reciprocal character of the closed-contour driving. For $\Phi = 0$ the population oscillates between $|0\rangle$ and an equal superposition of $|-1\rangle$ and $|+1\rangle$.
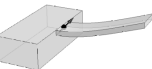
The resulting data, which is presented in Fig. 3.2a, shows oscillations of $P_{|0\rangle}(\tau)$ in time, with a π-periodic dependence of the population dynamics on Φ. Looking closely at the spectrum reveals that the decay times of the oscillations also depend on the global phase. For example, at $\Phi \approx 0$, the decay times are very short, while at $\Phi \approx -\pi/4$ the oscillations are long-lived. We will investigate and discuss this phase-dependent decay in the next section.

To complete the picture of the system's dynamics, we monitor the populations $P_{|\pm 1\rangle}(\tau)$ in $|-1\rangle$ and $|+1\rangle$ for $\Phi = 0, \pm\pi/2$ as presented in Fig. 3.2c. This measurement is achieved by applying a MW π-pulse resonant with the $|0\rangle \leftrightarrow |-1\rangle$ or $|0\rangle \leftrightarrow |+1\rangle$ transition at the end of the time evolution (dashed box in Fig. 3.2b). The resulting coherent spin dynamics show that, at $\Phi = \pi/2$ ($-\pi/2$), the spin exhibits clockwise (counterclockwise) circulation between $|0\rangle$, $|+1\rangle$, and $|-1\rangle$, thereby demonstrating time-reversal symmetry breaking population transfer for these values of Φ (see Fig. 3.2c, top and bottom). This behavior is in perfect analogy with electron dynamics on a closed loop interacting with a synthetic magnetic flux Φ [147]. Conversely, for $\Phi = 0$, the spin population oscillates between $|0\rangle$ and an equal superposition of $|-1\rangle$ and $|+1\rangle$ in a 'V-shaped' trajectory (see Fig. 3.2c, middle). These findings provide an intuition for the strong influence of Φ on the spin dynamics and the corresponding dressed states. For a more detailed discussion of the results and a direct comparison of the experimental results with numerical simulations using the Hamiltonian (3.1) we refer the reader to [114, 148].

3.3. Phase dependent coherence protection

Our experiments not only allow us to characterize the system's dynamics as a function of global phase, but to also directly access the dressed states' eigenenergies E_k from Eq. (3.3). After we initialize the system in $|\psi(\tau = 0)\rangle = (|\Psi_{-1}\rangle + |\Psi_0\rangle + |\Psi_{+1}\rangle)/\sqrt{3}$ (see Eq. (3.4)), each dressed state $|\Psi_k\rangle$ acquires a dynamical phase $E_k\tau/\hbar$ (see black lines in Fig. 3.3a). This phase accumulation leads to a time-dependent phase difference between the dressed states, which in turn governs the time evolution (see App. A.2). Thus, $P_{|0\rangle}(\tau)$ will oscillate in time at frequencies that correspond to the differences in the eigenenergies of the states, i.e. $\Delta_{m,n} = (E_m - E_n)/h$ with $m, n = 0, \pm 1$, but $m \neq n$ (see colored arrows and lines in Fig. 3.3a and b). As there are three possible pairs of dressed states, we expect to observe three beat frequencies in our measurements. This is verified by a Fourier transformation of $P_{|0\rangle}(\tau)$ from Fig. 3.2a, which reveals the $\Delta_{m,n}$ and thereby the dressed states' eigenenergies for any given Φ (see Fig. 3.3c).

The resulting frequency spectrum shows overall good agreement with the predicted spin transition frequencies for the undisturbed system, i.e. $\delta_{1,2} = 0$ (see Eq. (3.3) and colored lines in Fig. 3.3c). However, around $\Phi \approx 0, \pm\pi$ there are discrepancies between the expected and measured frequency components, as we find avoided crossings instead of the expected crossings in the frequency spectrum. Indeed, this observation indicates the vulnerability of the dressed states at these phase values to environmental fluctuations and slow drifts, which disturb the closed-contour interaction scheme. In particular, the most relevant noise sources are amplitude noise of the driving fields causing variations in the Rabi frequencies Ω_i, environmental magnetic fluctuations induced by nearby nuclear ^{14}N or ^{13}C spins, and drifts in the zero-field splitting D_0
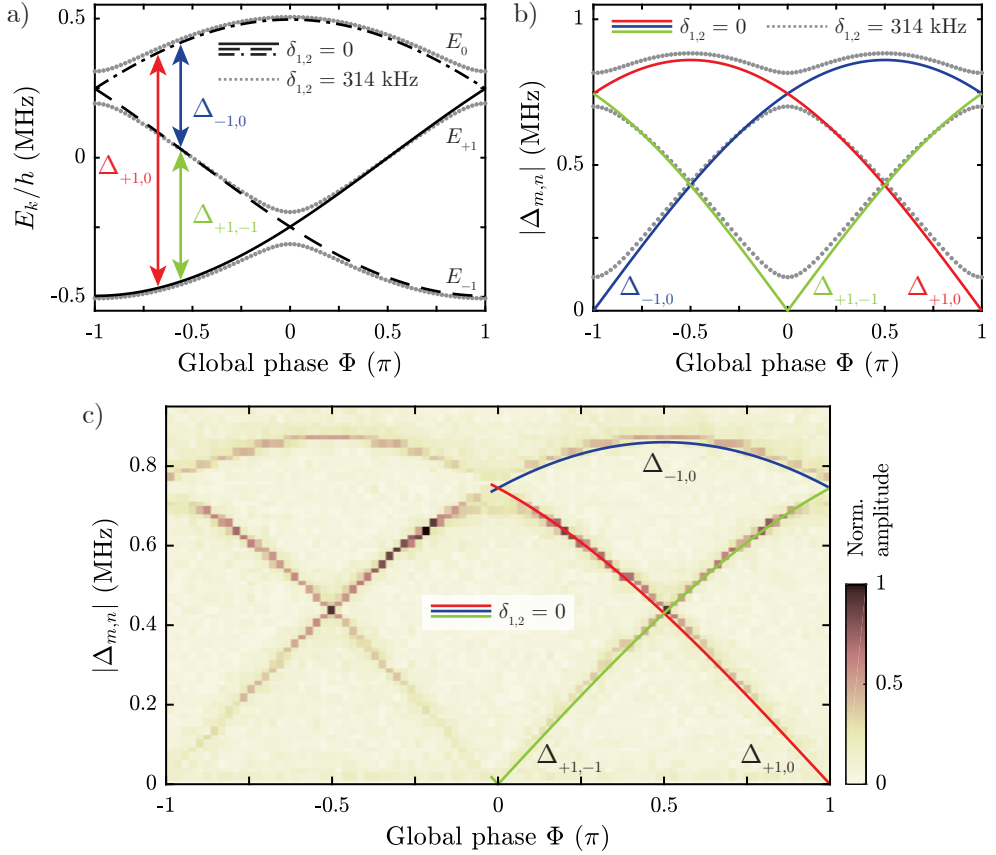
Figure 3.3.: Eigenenergy and transition frequency spectra of the three-level dressed states. a) Calculated eigenenergies E_k as a function of Φ for zero (black) and non-zero (gray) detunings $\delta_{1,2}$ for $\Omega/2\pi = 500\,\text{kHz}$. Two nearly degenerate dressed states are vulnerable to environmental fluctuations, which disturb the closed-contour interaction system causing the avoided crossings at $\Phi \approx 0, \pm\pi$. The colored arrows indicate the expected spin transition frequencies $\Delta_{m,n}$. b) Spectrum of spin transition frequencies $|\Delta_{m,n}|$ as a function of Φ for zero (colored) and non-zero (gray) detunings. The magnitude of the deviations between both cases is a measure of the system's vulnerability to environmental noise. For $\Phi \approx \pm\pi/4, \pm 3\pi/4$ the central transition frequencies are to first order not affected by detunings indicating a coherence protected spectral component. c) Discrete Fourier transformation of the data shown in Fig. 3.2a. The observed spin precession frequencies agree well with the calculated $|\Delta_{m,n}|$ for zero detunings (blue, red and green). The discrepancies around $\Phi \approx 0, \pm\pi$ arise from environmental magnetic fluctuations. The observed Fourier amplitude (contrast) is inversely proportional to the linewidth and, therefore, gives an indication of the decay time for each spectral component.
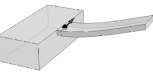
due to temperature fluctuations [107]. The latter two lead to variations in the de-tunings $\delta_{1,2}$ of Hamiltonian (3.1). The resulting, non-resonant ($\delta_{1,2} \neq 0$) driving lifts the degeneracies of the dressed states at $\Phi \approx 0, \pm\pi$ (see gray, dotted lines in Fig. 3.3a and b, for which we chose $\delta_1/2\pi = -\delta_2/2\pi = 50\,\text{kHz}$). This simplified approach illustrates the effect of environmental fluctuations on the dressed states. However, we stress that it is not a proper description of the experiment, as the interplay between the different noise sources is far more complex. In [114, 148] a careful modeling of these environmental noise effects is presented, yielding a good qualitative agreement between simulations and experimental data.

The dressed states' vulnerability to environmental fluctuations is also illustrated in Fig. 3.3b. The deviations of the transition frequencies between the unperturbed (colored) and perturbed (gray) system are a measure for the degree of vulnerabil-ity of the corresponding dressed state subspace to environmental noise. The largest deviations are present for $\Phi \approx 0, \pm\pi$, whereas for $\Phi \approx \pm\pi/4, \pm3\pi/4$ the central transition frequency is not affected by detunings indicating a coherent protected sub-space. Therefore, we expect the decay times T^{dec} of the dressed states to vary with Φ, having minima at $\Phi \approx 0, \pm\pi$ and maxima at $\Phi \approx \pm\pi/4, \pm3\pi/4$. This effect is qual-itatively confirmed by the phase-dependent interference pattern in Fig. 3.2a, where the interference fringes decay fastest for $\Phi \approx 0, \pm\pi$ and have some long-lived spectral components for phase values in between. Fig. 3.3c gives additional insights in the decay times of the different spectral components. For a given Φ the three frequency components are characterized by different peak amplitudes. As these amplitudes are inversely proportional to the linewidths, they are a direct measure for the decay times. Hence, the decay times of the three spectral components are in general not equal, i.e. $T^{\text{dec}}_{-1,0} \neq T^{\text{dec}}_{+1,0} \neq T^{\text{dec}}_{+1,-1}$. Moreover, the expected maxima of the decay times at $\Phi \approx \pm\pi/4$ (for $T^{\text{dec}}_{\pm1,0}$) and $\Phi \approx \pm3\pi/4$ (for $T^{\text{dec}}_{+1,-1}$) are indicated.

We further analyze the phase-dependent decay times and present detailed popula-tion oscillation data taken at $\Phi = 0$ (top) and $\Phi = -\pi/4$ (bottom) in Fig. 3.4a. By fitting the time traces with a sum of three exponentially decaying sinusoids [114], we find evidence for the expected significant enhancement of the dressed state coherence time from $T^{\text{dec}}_{-1,0} = 9(2)\,\mu\text{s}$ at $\Phi = 0$ to $T^{\text{dec}}_{-1,0} = 125(28)\,\mu\text{s}$ at $\Phi = -\pi/4$. To systemati-cally quantify the decay times as a function of Φ, we repeat this procedure for the data in Fig. 3.2a and extract the decay times $T^{\text{dec}}_{m,n}$ for each frequency component $\Delta_{m,n}$ (see Fig. 3.4b). The resulting phase-dependence of the decay times confirms our expec-tations, exhibiting pronounced maxima at $\Phi \approx \pm\pi/4, \pm3\pi/4$. These long coherence times result from the fact that at these global phase values, the corresponding two dressed states respond in the same way to environmental magnetic field noise (see Fig. 3.3a). In general, a long coherence time implies a highly predictable relative phase between two dressed states, which is directly linked to the noise vulnerability of their transition frequencies in Fig. 3.3b. We calculate the phase relation between two dressed states analytically with perturbation theory to model the decay times $T^{\text{dec}}_{m,n}$ (see [148] for further details). The result (dashed lines in Fig. 3.4b) reveals that at the phase values where $T^{\text{dec}}_{m,n}$ peaks, two dressed states exist whose eigenenergies show the same perturbative response to magnetic field fluctuations, even up to fourth order [148]. These pairs of states then form a subspace that offers efficient coher-ence protection, and for which $T^{\text{dec}}_{m,n}$ should theoretically approach the spin relaxation time. We attribute the significantly reduced value of $T^{\text{dec}}_{-1,0} \approx 105\,\mu\text{s}$ measured at
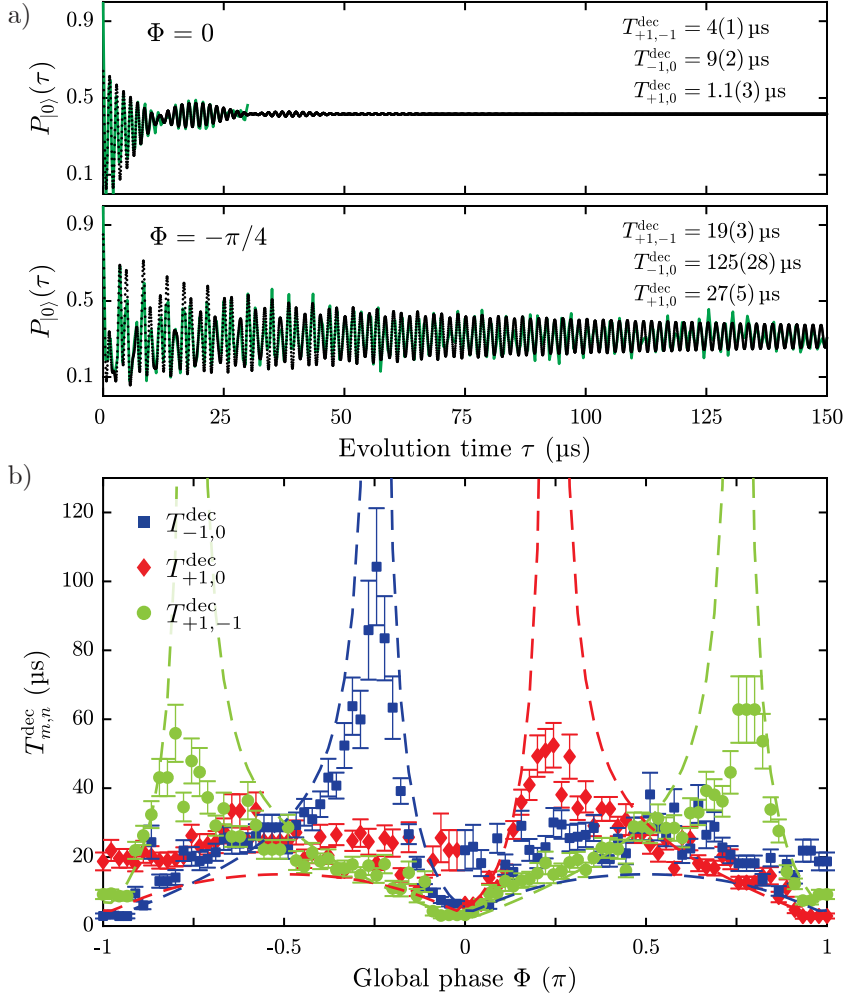
Figure 3.4.: Phase-controlled coherence protection of closed-contour dressed states. a) Time evolution of $P_{|0\rangle}(\tau)$ for $\Phi = 0$ (top) and $\Phi = \pi/4$ (bottom) including a fit with three exponentially damped harmonic frequency components (black). The resulting decay times $T_{m,n}^{\mathrm{dec}}$ reveal a strong phase dependence, varying between $T_{-1,0}^{\mathrm{dec}} = 9(2)\,\mu s$ ($\Phi = 0$) and $T_{-1,0}^{\mathrm{dec}} = 125(28)\,\mu s$ ($\Phi = -\pi/4$) for the most long-lived spectral component. b) Systematic study of $T_{m,n}^{\mathrm{dec}}$ as function of Φ obtained by fitting the data from Fig. 3.2a. The decay times are minimal for $\Phi \approx 0, \pm\pi$, while having pronounced maxima at $\Phi \approx \pm\pi/4, \pm3\pi/4$. The dashed lines are the result of a second-order perturbative caluculation of $T_{m,n}^{\mathrm{dec}}$ [148]. The observed asymmetry with respect to $\Phi = 0$ is caused by slow environmental drifts, for example of the zero-field splitting. Note that the extracted decay times differ slightly from those presented in panel a), as the data originate from separate measurements and thus under a different noise environment. All error bars represent $95\,\%$ confidence intervals of the fits.
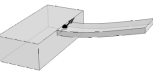
$\Phi = -\pi/4$ to driving field fluctuations – a hypothesis that is quantitatively supported by numerical modeling [148]. Additionally, compared to the theoretical calculation, our data shows an unexpected, though strong asymmetry of the decay times, most prominently visible in the varying magnitude of the four local maxima in Fig. 3.4b. This behavior is induced by slow experimental drifts in the zero-field splitting due to temperature variations and is also quantitatively reproduced by simulations that take these drifts into account [148]. Nevertheless, the theoretical and experimental results demonstrate that the global phase does not only control the dynamics under closed-contour driving but also serves as a handle to decouple the dressed states from magnetic fluctuations, thereby effectively protecting the NV spin.

3.4. Conclusion and outlook

To summarize, by combining coherent MW and strain manipulation we have established dressed states emerging from closed-contour driving of the three-level system in the NV's ground state. Compared to prior work on coherence protection by continuous driving [43, 44, 52, 154], such dressed states can be efficiently decoupled from environmental magnetic noise at comparatively weak driving fields, $\Omega/2\pi = 500\,\text{kHz}$. The decoupling we achieved is thereby far more efficient than comparable schemes relying on coherent driving of two-level systems. At the same time, experimental complexity is reduced compared to approaches based on multiple MW fields [155]. Our results evidence that the global phase in such a closed-contour interaction scheme serves as a useful control parameter not only for the system's coherent dynamics but also for the tunable decoupling mechanism of the dressed states. The phase-dependent coherence protection is explained in terms of the eigenenergies of the underlying Hamiltonian and their response to environmental noise. Specifically, the dressed states offer decoupling from magnetic field noise up to fourth order for certain phase values [148]. Additionally, our analysis indicates that further experimental improvements would make dressed states approaching T_1 limited inhomogeneous dephasing times feasible.

To realize such improved coherence protection, stabilizing and controlling the experimental environment is unavoidable. This may be realized by implementing a temperature stabilization in terms of a Peltier element in the setup to minimize drifts in zero-field splitting or to perform the experiment in more stable environments like in vacuum and/or cryogenic conditions. Additionally, using driving fields with less amplitude noise would improve the decoupling mechanism of the dressed states. With that, even larger driving amplitudes would be achievable without being limited by driving field fluctuations.

Our dressed states emerging in a three-level closed-contour scheme have promising application perspectives. Recently, efficiently decoupled two-level dressed states have been established as a powerful resource for sensing gigahertz fields [47, 156]. Combing these sensing schemes with the tunability and coherence protection of our dressed states offers interesting avenues for enhanced sensitivities and phase-tuning of the sensing frequencies. Our dressed state can also be used as built-in sensors to study the phase noise in our hybrid spin-mechanical system, as for $\Phi = \pm\pi/2$ the eigenenergies depend linearly on the phase. Moreover, the time-reversal symmetry breaking character of our dressed states is in strong analogy to recent realizations

of synthetic gauge fields in optomechanical systems [157]. This analogy opens interesting resources, for example for realizing on-chip, non-reciprocal MW elements, such as MW circulators or directional amplifiers, using ensembles of NV centers with engineered dissipation. In the context of quantum information processing the exploration of the coherent coupling of the dressed states to nearby nuclear spin [158] or the investigation of non-Abelian geometric phases induced in a subspace of two degenerate dressed states at $\Phi = 0, \pm\pi$ to implement error-resistant geometric quantum gates [159] offers exciting routes.

However, the measurements up to now have only addressed the preparation of a superposition of the three dressed states (see Eq. (3.4)). To take full advantage of the dressed state manifold and the prolonged coherence times, it is imperative to establish fast and robust initialization of individual, well-defined dressed states as well as precise coherent manipulation via applied control fields – an issue, which will be discussed in the next chapters.
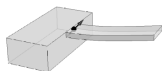
4. Initialization of three-level dressed states using STA

Decoherence of quantum states is one of the main obstacles to their operation in quantum sensing [81, 96, 160] and quantum information processing [161, 162], as it limits the sensitivity and the number of executable quantum gates. Therefore, quantum states require an efficient protection from environmental fluctuations [163, 164], which is primarily achieved by pulsed dynamical decoupling [27–29, 31]. However, these protocols suffer from drawbacks including experimental complexity and vulnerability to pulse errors [165]. In contrast, dressed states generated by continuous dynamical decoupling yield efficient coherence protection [39, 44, 52, 154, 166] in a robust and experimentally accessible way that is readily combined with quantum gates [41–43, 167]. In particular, the three-level dressed states emerging under closed-contour driving introduced in Chap. 3 exhibit outstanding decoupling from magnetic noise even for comparatively weak driving fields and thereby go beyond what is offered by driven two-level systems [114, 148].

A major challenge for further applications of such dressed states, however, is the difficulty in performing fast, high-fidelity initialization into individual, well-defined dressed states. Up to now, such initialization has focused on two-level systems and has mainly used adiabatic state transfer [41, 43], without characterizing the resulting transfer fidelities in detail. Despite their robustness to experimental imperfections, adiabatic protocols generally suffer from a tradeoff between speed and fidelity. The processes must be slow to maintain fidelity, but fast enough to avoid decoherence during the state transfer. For experimentally achievable driving field strengths, this tradeoff and the remaining sources of decoherence form a key limitation to further advances in the use of dressed states in quantum applications.

'Shortcuts to adiabaticity' (STA) [168–173] provide a useful toolbox to remedy and overcome the stated limitations. These approaches mitigate decoherence by designing fast dynamics that reproduce the results of a slow, adiabatic evolution, thus offering accurate operations despite a noisy environment within minimized process times [173]. STA protocols have been studied theoretically [159, 174–178] and implemented experimentally [179–182] with NV centers, but besides the theoretical proposal [159] none of the experimental realizations has been focused on the complete three-level system in the NV ground state so far.

In this chapter, we combine STA and the coherence protection provided by closed-contour, coherent driving of the NV spin in its ground state and demonstrate the initialization of well-defined, individual dressed states. Besides the inherently slow adiabatic transfer protocols, we exploit STA protocols to realize fast and robust state initialization. Using STA protocols, we accelerate the transfer speed by a factor of 2.6 compared to the adiabatic approach. We further show bidirectionality of the STA state transfer, which allows us to determine a transfer fidelity of 99.0(3) % bounded
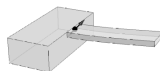
by experimental limitations. We finally present a first proof of principle of coherent control in the dressed state manifold. Thus, our results enable direct and efficient access to the coherence-protected dressed states introduced in Chap. 3 and thereby offer attractive avenues for their room temperature application to quantum technologies.

The presented results have been published in [183].

4.1. State transfer to the dressed state manifold

Faithfully transferring a quantum system from an initial to a desired final state is a central topic of quantum physics. A commonly applied approach to realize such state transfer relies on the adiabatic theorem. Its basic idea is that the quantum system remains in an instantaneous eigenstate if the variation of the Hamiltonian is slowly enough and if there is always an energetic gap to the other instantaneous eigenstates [184]. In other words, gradually changing conditions allow the system to adapt its configuration and to undergo an evolution that is referred to as adiabatic. To ensure adiabaticity the energy separation of the instantaneous, adiabatic eigenstates needs to be much larger than their mutual coupling at each instant in time. If this criterion is, however, not fulfilled, i.e. the changes of the control parameters are too fast, the evolution will generally have diabatic (nonadiabatic) character, which ultimately results in mixing of the adiabatic eigenstates [184]. In this context, STA represent theoretically developed methods, which design fast routes to the final state of an adiabatic change by avoiding diabatic errors. For an illustrative analogy to the STA approach, we consider a flat, horizontal road turn, which corresponds to the desired state transfer. To achieve a faster process, i.e. letting the vehicles go faster without sliding off the road, we can modify the road turn by inclining the roadway surface about its longitudinal axis with a bank angle. The inclining corresponds to additional control fields, which enable the same transfer process result but on shorter timescales [173].

Here, we study state transfer protocols to initialize into the dressed states that emerge from closed-contour interaction in the NV ground state as introduced in Chap. 3. To that end, we use our hybrid spin-mechanical system (see Fig. 3.1a) to simultaneously and coherently drive all three available NV spin transitions as illustrated in Fig. 4.1a. The resulting dressed states are best described in an appropriate rotating frame (see Eq. (3.1)), where, under resonant driving of all three transitions, i.e. $\delta_{1,2} = 0$, the system Hamiltonian reads

$$
\begin{aligned}
\hat{\mathcal{H}}_0(t)/\hbar &= \frac{1}{2}\Big[\Omega_1(t)\,|{-}1\rangle\langle 0| + \Omega_2(t)\,|{+}1\rangle\langle 0| + \Omega_3\,\mathrm{e}^{\mathrm{i}\Phi}\,|{-}1\rangle\langle{+}1| + \mathrm{H.c.}\Big] \\
&= \frac{1}{2}\begin{pmatrix} 0 & \Omega_1(t) & \Omega_3\,\mathrm{e}^{\mathrm{i}\Phi} \\ \Omega_1(t) & 0 & \Omega_2(t) \\ \Omega_3\,\mathrm{e}^{-\mathrm{i}\Phi} & \Omega_2(t) & 0 \end{pmatrix}\,.
\end{aligned}
\tag{4.1}
$$

In this case, the matrix representation is given in the basis $\{|{-}1\rangle, |0\rangle, |{+}1\rangle\}$. We explicitly note that in contrast to Eq. (3.1), Hamiltonian $\hat{\mathcal{H}}_0(t)$ is now time-dependent, as the amplitudes (Rabi frequencies) of the MW driving fields $\Omega_{1,2}(t)$ are now a function of time, while the mechanical driving amplitude $\Omega_3 \equiv \Omega$ remains constant. In the following, we tune the global phase $\Phi = \phi_1 + \phi_3 - \phi_2$ (where ϕ_1, ϕ_2, and ϕ_3 are the

phases of the driving fields, see Sec. 3.2) to $\Phi = \pi/2$. We choose this particular value of Φ, because the resulting, equal energy spacing between the dressed states allows for a straightforward derivation of an analytical, purely real STA for our system. The STA formalism is, however, applicable to arbitrary global phase values Φ, as we can employ numerical methods to determine the required experimental protocols (see App. A.4).
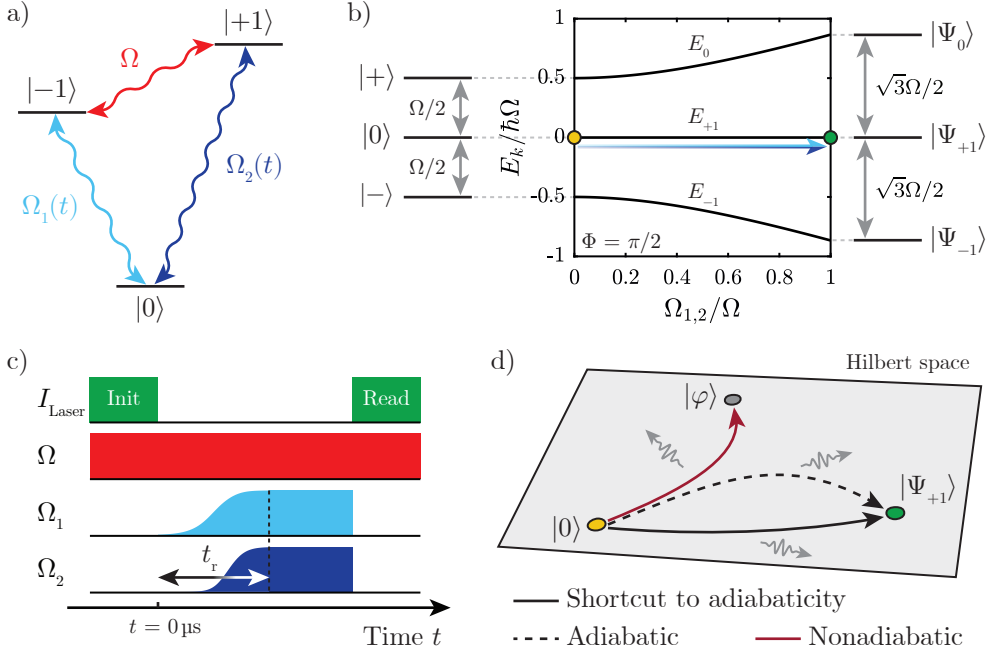

Figure 4.1.: State transfer schematics. a) Level scheme of the NV's $S = 1$ ground state with spin states $|0\rangle$, $|-1\rangle$, and $|+1\rangle$. All three spin transitions are individually and coherently addressable, either by MW magnetic fields ($\Omega_{1,2}(t)$, light and dark blue) or by a cantilever induced strain field ($\Omega_3 = \Omega$, red). b) Level schemes in the rotating frame for $\Phi = \pi/2$. The initial system (left) comprises the states $|0\rangle$, $|-\rangle$, and $|+\rangle$, with $|-\rangle$ and $|+\rangle$ being equal admixtures of $|-1\rangle$ and $|+1\rangle$. Ramping the amplitudes of both MW fields results in a transfer to the final dressed states $|\Psi_k\rangle$ ($k = 0, \pm 1$, right). We initialize the system in $|0\rangle$ (yellow) to transfer along the adiabatic eigenstate $|\psi_{+1}(t)\rangle$ to $|\Psi_{+1}\rangle$ (dark green). c) Pulse sequence employed for state transfer. Note that in general $\Omega_{1,2}(t)$ may be complex and have different time dependencies. d) Schematics of possible state transfer dynamics. A perfect adiabatic evolution transfers the desired state along the dashed trajectory, which is followed exactly only in the infinite time limit. Speeding up the evolution causes nonadiabatic transitions leading to an imperfect state transfer (dark red). STA protocols (solid black) in general employ control pulses to start and end up at the same states as the perfect adiabatic protocol, thereby ensuring perfect state transfer, but for arbitrary evolution times and possibly along a different path. Dissipation (gray arrows) leads to errors in all processes.
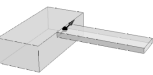
To achieve state transfer into the dressed state basis, we start in the initial NV system, where only the strain field resonant with the $|-1\rangle \leftrightarrow |+1\rangle$ transition is applied, i.e. $\Omega_{1,2}(t=0) = 0$ and $\Omega_3 = \Omega$. For $\Phi = \pi/2$, the eigenstates of $\hat{\mathcal{H}}_0(t)$ prior to state transfer are then $|0\rangle$ and $|\pm\rangle \equiv (|-1\rangle \mp \mathrm{i}|+1\rangle)/\sqrt{2}$ (see Fig. 4.1b, left). By ramping up the MW driving fields $\Omega_{1,2}(t)$ within a ramp time t_r, we end up in the final dressed state system with $\Omega_{1,2}(t=t_\mathrm{r}) = \Omega_3 = \Omega$. The eigenstates of the final system are the desired dressed states given by

$$|\Psi_k\rangle = \frac{1}{\sqrt{3}}\left(\mathrm{e}^{\mathrm{i}\pi(1-4k)/6}|-1\rangle + |0\rangle + \mathrm{e}^{-\mathrm{i}\pi(1-4k)/6}|+1\rangle\right), \tag{4.2}$$

with $k = 0, \pm 1$ (see Fig. 4.1b, right, and Eq. (3.2)). Both initial and final system are linked via the instantaneous (adiabatic) eigenstates $|\psi_k(t)\rangle$ ($k = 0, \pm 1$) defined at each instant in time, i.e. for each value of $\Omega_{1,2}(t)$. These eigenstates coincide with the initial system at $t = 0$ and with the final system at $t = t_\mathrm{r}$. Thus, in Fig. 4.1b our state transfer protocol consists of spin initialization of the initial system into $|0\rangle$ with $\Omega_{1,2}(t=0) = 0$ (yellow dot), after which we apply suitable ramps to the MW driving field amplitudes $\Omega_{1,2}(t)$ (blue arrow) to transfer along the adiabatic eigenstates into the dressed state basis (green dot). For analytic simplicity, we choose to work with dressed states under symmetric driving of all three transitions, i.e. $\Omega_{1,2}(t=t_\mathrm{r}) = \Omega_3 = \Omega$.

The generally employed experimental pulse sequence is shown in Fig. 4.1c. A green laser pulse prepares the initial system in $|\psi(t=0)\rangle \equiv |0\rangle$. Then, we individually ramp the MW driving field amplitudes within the ramp time t_r. The state $|0\rangle$ is thereby ideally transferred to $|\Psi_{+1}\rangle$, but in general ends up in a (non-ideal) final state $|\psi(t_r)\rangle$. For analysis of the final state, we let $|\psi(t_r)\rangle$ subsequently evolve in presence of all three driving fields,

$$|\psi(t)\rangle = \mathrm{e}^{-\mathrm{i}(t-t_\mathrm{r})\hat{\mathcal{H}}_0(t_\mathrm{r})/\hbar}|\psi(t_\mathrm{r})\rangle, \tag{4.3}$$

where $t > t_\mathrm{r}$, and finally read out the population in $|0\rangle$ using spin-dependent fluorescence,

$$P_{|0\rangle}(t) = |\langle 0|\psi(t)\rangle|^2. \tag{4.4}$$

During the whole pulse sequence, the amplitude of the mechanical driving field is constant at $\Omega_3/2\pi = \Omega/2\pi = 510\,\mathrm{kHz}$.

The fluorescence signal acquired during readout directly indicates, whether the state transfer was successful or not. If we prepare our system in a single dressed state, i.e. $|\psi(t_\mathrm{r})\rangle = |\Psi_{+1}\rangle$, the measured population for $t > t_\mathrm{r}$ is time-independent with $P_{|0\rangle}(t) = 1/3$. If, however, we do not prepare in a single dressed state, but rather a mixture of dressed states, we measure a time-dependent population $P_{|0\rangle}(t)$ for $t > t_\mathrm{r}$, characterized by a beating of the transition frequencies of the dressed states (see Sec. 3.3 and App. A.2 for a detailed description of the readout mechanism).

Fig. 4.1d shows the generalized idea of STA protocols [180, 185]. Starting in the initial state $|0\rangle$ an adiabatic protocol transfers along the dashed trajectory to the final state $|\Psi_{+1}\rangle$. This trajectory, however, is only followed exactly in the infinite time limit. For finite time realizations, $|0\rangle$ may be transferred to a different state $|\varphi\rangle$ as nonadiabatic errors lead to imperfect state transfer (dark red). STA protocols (solid

black) in general design an evolution that provides perfect state transfer, but for arbitrary evolution times and generally along a different path compared to adiabatic protocols. To achieve such transfer, controlled ramps of $\Omega_{1,2}(t)$ are employed, which ensure that the transfer state coincides with the desired states at the initial and final time of the protocol, $|0\rangle$ and $|\Psi_{+1}\rangle$, respectively. The design and implementation of appropriate ramp functions will be discussed in the following sections.

4.2. Adiabatic state transfer

To benchmark subsequent studies of STA protocols, we first demonstrate state transfer into the dressed state manifold by employing an adiabatic protocol. Such a state transfer protocol in general ensures that the system will remain in an initially prepared adiabatic eigenstate if changes to the system are sufficiently slow. To that end, we choose the 'Vitanov-shape' ramp functions developed in quantum optics for adiabatic state transfer in three-level 'Λ-systems' via STIRAP [186],

$$\Omega_{1,2}(t) = \Omega \sin[\theta(t)] \ , \tag{4.5}$$

(see Fig. 4.2a), with

$$\theta(t) = \frac{\pi}{2} \cdot \frac{1}{1 + \exp[-\nu(t - t_0)]} \ . \tag{4.6}$$

Here, the phase function $\theta(t)$ is a Fermi function shifted by

$$t_0 = \ln\left[\frac{\pi}{2\sin^{-1}(\varepsilon)} - 1\right]/\nu \ , \tag{4.7}$$

which has the two free parameters ε and ν (see red highlights in Fig. 4.2a). While $\varepsilon \ll 1$ sets the amplitude of the ramp's unavoidable discontinuities at $t = 0$ and $t = t_{\mathrm{r}}$, ν controls the slope of $\theta(t)$ at $t = t_0$ and thereby is directly linked to the ramp time

$$t_{\mathrm{r}} = t_0 - \ln\left[\frac{\pi}{2\sin^{-1}(1-\varepsilon)} - 1\right]/\nu \ . \tag{4.8}$$

In all our experiments we use $\varepsilon = 10^{-3}$, as this value is comparable to the estimated amplitude noise of our MW signals (see App. A.1.2 for a detailed description of the MW field generation and control).

In Fig. 4.2b we present the time evolution of $P_{|0\rangle}(t)$ for several values of t_{r} after employing the adiabatic protocol. For small t_{r}, i.e. for fast ramping, $P_{|0\rangle}(t)$ oscillates for $t > t_{\mathrm{r}}$ indicating imperfect (nonadiabatic) state transfer. Increasing t_{r} reduces the amplitude of these oscillations, until $P_{|0\rangle}(t)$ becomes time-independent with $P_{|0\rangle}(t > t_{\mathrm{r}}) \approx 1/3$. This transition from an oscillatory to a constant time evolution with increasing t_{r} marks a change from a nonadiabatic to an adiabatic transition.

We corroborate our experimental findings by calculating the time evolution of $P_{|0\rangle}(t)$. To that end, we solve the time-dependent Schrödinger equation for $|\psi(t)\rangle$ using Hamiltonian (4.1) and find excellent agreement with our data (see Fig. 4.2b). Note that the calculation is based on a fully coherent evolution, i.e. it does not take
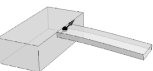
into account dissipation, which causes additional damping in the experimental data. To further highlight the agreement between measurement and calculation, we present in Fig. 4.2c a time trace recorded in the nonadiabatic regime for $t_r = 6.8\,\mu s$, which is indicated by green dashed line in Fig. 4.2b.

The transition from the nonadiabatic to the adiabatic regime is determined by the adiabatic criterion, which requires that the energy separation of the adiabatic eigenstates (see Fig. 4.1b) far exceeds their mutual coupling. This requirement ensures that transitions between the adiabatic eigenstates are avoided during the transfer protocol, but thereby implies inherently slow processes. The method to determine the adiabatic criterion is to express the state transfer dynamics in the adiabatic frame [168, 173]. The associated adiabatic basis consists of the instantaneous eigenstates of Hamiltonian $\hat{\mathcal{H}}_0(t)$, i.e. the adiabatic eigenstates $|\psi_k(t)\rangle$ (given in the $\{|m_s\rangle\}$ basis). In the adiabatic frame, these states are accordingly time-independent and denoted by $|\psi_k\rangle$.
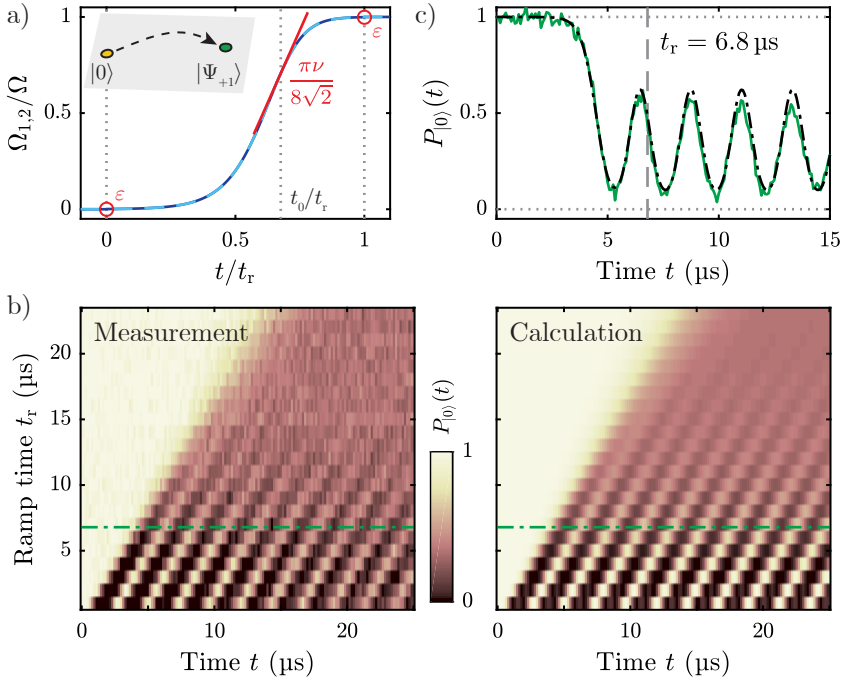

Figure 4.2.: Adiabatic state transfer. a) Experimentally employed ramps for the MW field amplitudes. Both MW fields are ramped simultaneously in an optimized STI-RAP pulse shape. The slope parameter ν is directly linked to the ramp time t_r, the amplitude of the ramp's unavoidable discontinuities at $t = 0$ and $t = t_r$ is set by ε. b) Measurement of $P_{|0\rangle}(t) = |\langle 0|\psi(t)\rangle|^2$ as a function of time t and ramp time t_r. The right panel shows theoretical calculations based on a fully coherent evolution. For small t_r oscillations in $P_{|0\rangle}(t)$ indicate a nonadiabatic transfer, whereas for slower ramping of the MW fields the state transfer becomes adiabatic. The green line indicates the location of the time trace presented in c). c) Time evolution of measured population $P_{|0\rangle}(t)$ (green) for $\nu = \Omega/2$ with corresponding calculation (black).

Thus, the unitary transformation to the adiabatic frame is given by

$$\hat{\mathcal{U}}(t) = \sum_{k=0,\pm 1} |\psi_k\rangle\langle\psi_k(t)| \ , \tag{4.9}$$

which for each time t maps the adiabatic eigenstate $|\psi_k(t)\rangle$ onto the time-independent state $|\psi_k\rangle$, i.e. $|\psi_k\rangle = \hat{\mathcal{U}}(t)\,|\psi_k(t)\rangle$. Specifically, we can obtain $\hat{\mathcal{U}}(t)$ from its inverse $\hat{\mathcal{U}}^\dagger(t)$, whose columns contain the normalized adiabatic eigenstates $|\psi_k(t)\rangle$.

By applying this unitary transformation to the Schrödinger equation, we find that the Hamiltonian in the adiabatic frame has the form

$$\hat{\mathcal{H}}_0^{\mathrm{ad}}(t) = \hat{\mathcal{U}}(t)\,\hat{\mathcal{H}}_0(t)\,\hat{\mathcal{U}}^\dagger(t) - i\hbar\hat{\mathcal{U}}(t)\,\partial_t\hat{\mathcal{U}}^\dagger(t) \ . \tag{4.10}$$

Hamiltonian $\hat{\mathcal{H}}_0^{\mathrm{ad}}(t)$ comprises two terms. The first term in Eq. (4.10) is by definition of $\hat{\mathcal{U}}(t)$ diagonal and gives the eigenenergies of the adiabatic eigenstates. The second term, however, is nondiagonal and results in diabatic couplings between the adiabatic eigenstates.

In our specific case defined by Hamiltonian (4.1) and the ramp functions from Eq. (4.5), we find

$$\hat{\mathcal{H}}_0^{\mathrm{ad}}(t)/\hbar = \begin{pmatrix} \frac{\Omega}{2}\sqrt{2-\cos[2\theta(t)]} & \frac{\cos[\theta(t)]\,\partial_t\theta(t)}{2-\cos[2\theta(t)]} & 0 \\ \frac{\cos[\theta(t)]\,\partial_t\theta(t)}{2-\cos[2\theta(t)]} & 0 & -\frac{\cos[\theta(t)]\,\partial_t\theta(t)}{2-\cos[2\theta(t)]} \\ 0 & -\frac{\cos[\theta(t)]\,\partial_t\theta(t)}{2-\cos[2\theta(t)]} & -\frac{\Omega}{2}\sqrt{2-\cos[2\theta(t)]} \end{pmatrix} \ , \tag{4.11}$$

which is expressed in the basis $\{|\psi_0\rangle, |\psi_{+1}\rangle, |\psi_{-1}\rangle\}$ (see App. A.3 for more details on the derivation). At this point, the adiabatic condition is evident, as we need to compare the off-diagonal elements of $\hat{\mathcal{H}}_0^{\mathrm{ad}}(t)$ with the separation of the diagonal elements. Consequently, the adiabatic criterion reads

$$\frac{2\cos[\theta(t)]\,\partial_t\theta(t)}{\Omega\big(2-\cos[2\theta(t)]\big)^{3/2}} \ll 1 \ . \tag{4.12}$$

Note that the criterion is proportional to $\partial_t\theta(t)$, i.e. it is directly linked to the slope of the applied ramps and thereby to the ramp time. By choosing an upper limit for the right-hand side of $1/10$ for all times, we find a critical ramp time of $t_{\mathrm{r}}^{\mathrm{ad}} = 12.9\,\mathrm{\mu s}$ for an adiabatic transition.

4.3. State transfer using STA

The established adiabatic state transfer into the dressed state basis requires long evolution times $(t_{\mathrm{r}} > t_{\mathrm{r}}^{\mathrm{ad}})$. To mitigate this drawback, i.e. to accelerate the initialization procedure without suffering from nonadiabatic errors, a general strategy termed STA [168–173] was theoretically proposed. The development of STA methods and applications has been quite fast since the term was coined in [170]. STA protocols provide fast dynamics that reproduce the results of a slow, adiabatic transition. The shortcuts are designed by a set of analytical and numerical methods,
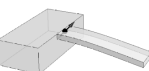
including, among others, transitionless driving (TD) [168, 169, 187][1], superadiabatic transitionless driving (SATD) [185], and the dressed state approach to SATD [185]. All techniques harness nonadiabatic transitions by adding theoretically engineered corrections to the state transfer Hamiltonian, which are experimentally implemented by control pulses. Thus, by speeding up the processes, STA methods are particularly useful for manipulating a quantum system on timescales limited by the coherence time, while enhancing flexibility and robustness to a noisy environment [173].

To allow for an analytical STA correction that is compatible with our current experimental setup, we focus on the case of symmetric driving and a global phase value $\Phi = \pi/2$. In this case, the TD approach does not demand any control of the mechanical drive, which remains constant over the whole experimental sequence (see Fig. 4.1c). Additionally, this technique results in a purely real correction for the MW fields, so that no time-dependent phase control of these fields is required.

The basic idea of the TD method is to add auxiliary control fields to the system, so that the dynamics follow exactly the time evolution that is defined by Hamiltonian (4.1) in the infinite time limit, i.e. nonadiabatic transitions between the adiabatic eigenstates are precisely canceled [168, 173]. To that end, we introduce a correction $\hat{\mathcal{H}}_{\mathrm{TD}}(t)$ to the Hamiltonian $\hat{\mathcal{H}}_0(t)$, which counteracts the coupling between the adiabatic eigenstates. Accordingly, the correction is chosen in a way that the second term in Eq. (4.10) is canceled, i.e.

$$\hat{\mathcal{H}}_0(t) \to \hat{\mathcal{H}}_0(t) + \hat{\mathcal{H}}_{\mathrm{TD}}(t) = \hat{\mathcal{H}}_0(t) + \mathrm{i}\hbar\Big[\partial_t \hat{\mathcal{U}}^\dagger(t)\Big]\hat{\mathcal{U}}(t) \ . \tag{4.13}$$

Evaluating the TD correction results in additional components in the Hamiltonian, which add to the initial driving field ramps (see App. A.3). We thereby find the modified MW pulse amplitudes

$$\Omega_{1,2}(t) = \Omega \sin[\theta(t)] \pm 2 \cdot \frac{\cos[\theta(t)]\,\partial_t\theta(t)}{2 - \cos[2\theta(t)]} \ , \tag{4.14}$$

while keeping the phases of all field constant. The resulting envelopes of MW driving fields for $\nu = \Omega/2$ and $\Omega/2\pi = 510\,\mathrm{kHz}$ are shown in Fig. 4.3a. The TD approach provides different corrections for the two MW fields, such that both field amplitudes are ramped successively with different functional forms. We note that in our experiment, we can implement the TD method of Eq. (4.13) only for $\Phi = \pm\pi/2$, where time-reversal symmetry is maximally broken (see Fig. 3.2c) and the resulting TD correction is, therefore, purely real. For different values of Φ, the resulting imaginary component to the corrected ramps would require control of the phase and amplitude of the driving fields. Our strain field mediated by the mechanical oscillator does not provide such phase control on the relevant timescales. However, other STA methods [185] can be applied to find appropriate ramps (see App. A.4).

---

[1]An equivalent terminology for the concept of TD is 'counterdiabatic driving' [173].

In Fig. 4.3b we present the experimental results of the state transfer when applying the TD corrected ramps. Independent of t_r, the time evolution of $P_{|0\rangle}(t)$ converges to $\approx 1/3$, indicating perfect initialization of a single dressed state, even for the fastest ramps. The measurements are in striking agreement with the calculations based on the Schrödinger equation. Note that there exists a lower bound for t_r in case of the TD corrected ramps. For faster state transfer, the corresponding ramps lead to momentary driving field amplitudes either < 0 or $> \Omega$ (see App. A.3). In such a scenario the energy separation of the adiabatic eigenstates gets temporarily larger than in Fig. 4.1b, thereby temporarily 'relaxing' the adiabatic criterion. To ensure a fair comparison with the adiabatic transfer protocol, we, therefore, exclude this parameter range from our study (grayed area in Fig. 4.3b). The fastest possible state transfer corresponds to $\nu = \Omega/2$, resulting in $t_r = 6.8\,\mu s$. The corresponding time trace is presented in Fig. 4.3c.
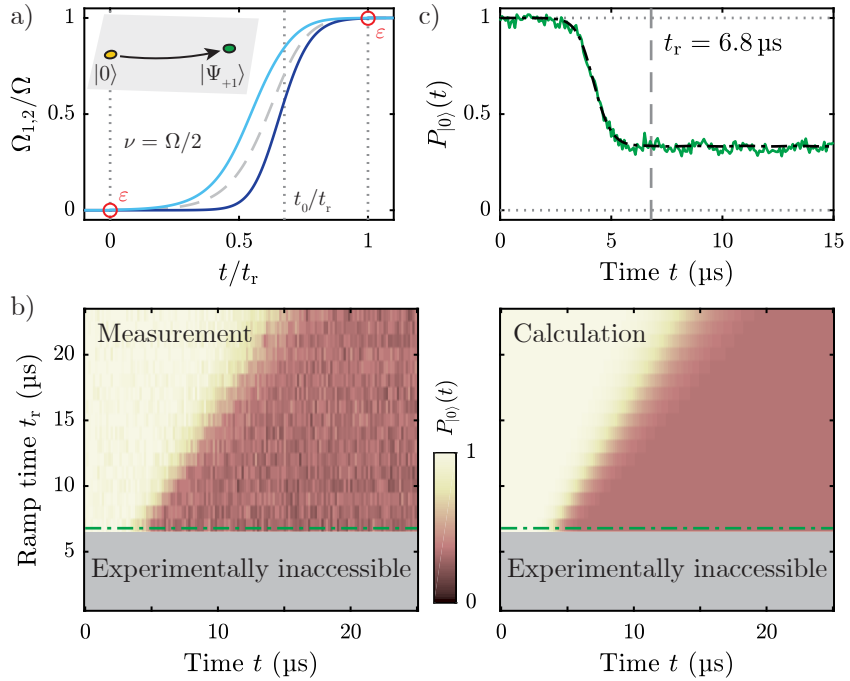

Figure 4.3.: STA state transfer protocol. a) Envelope of the optimized MW field amplitudes for $\nu = \Omega/2$ and $\Omega/2\pi = 510\,\text{kHz}$. Modifications of the adiabatic pulse shape (dashed) lead to altered and unequal ramps for the two MW fields (Ω_1 light blue, Ω_2 dark blue). b) Two-dimensional plots of $P_{|0\rangle}(t)$ as a function of time t and ramp time t_r. The left plot shows experimental data, and the right plot shows theoretical calculations. We achieve state transfer with high fidelity independent of t_r. The green line indicates the location of the time trace presented in c) with ramp parameters at the experimental limit ($\nu = \Omega/2$, border of the grayed area, see text). c) Time evolution of measured population $P_{|0\rangle}(t)$ (green) for the same parameters as in Fig. 4.2c with corresponding calculation (black).
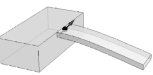
Fig. 4.2c and Fig. 4.3c allow for a direct comparison of the adiabatic and STA transfer protocols under identical conditions. For the first approach, $P_{|0\rangle}(t)$ oscillates, thereby clearly indicating nonadiabatic errors in the dressed state initialization (see Fig. 4.2c). However, in case of the TD protocol, almost no oscillations in $P_{|0\rangle}(t)$ are visible, which indicates excellent state transfer (see Fig. 4.3c). The remaining small oscillations are attributed to residual imperfections in the dressed state initialization, which we discuss in the next section. By comparing these residual oscillations with the calculations of the adiabatic protocol, we find that at least an adiabatic ramp time of $t_{\mathrm{r}} = 17.6\,\mu\mathrm{s}$ would be required to achieve the same transfer fidelity when using an adiabatic approach. This allows us to determine the acceleration of the TD protocol compared to adiabatic ramping, for which we here find a speedup factor of 2.6.

4.4. Reverse state transfer and transfer fidelity

Having implemented the initialization into the dressed state manifold by STA protocols, we next demonstrate the reversibility of these transfer protocols and map from the dressed states back to the initial system. This remapping also verifies that our TD protocol indeed results in the initialization of an individual, pure dressed state, and not of an incoherent state mixture, which may also yield a time-independent $P_{|0\rangle}(t) = 1/3$. More specifically, we use the TD method introduced in Sec. 4.3 to prepare the system in a single dressed state, and then use the inverted TD protocol, i.e. $t \rightarrow t_{\mathrm{r}} - t$, to map back to the NV states, while measuring the population $P_{|0\rangle}(t')$ as a function of the remapping time t'. The corresponding pulse sequence is presented in Fig. 4.4a. For both transfer directions we set $\nu = \Omega/2$ to achieve maximal ramping speed.

In Fig. 4.4b we present the time evolution of $P_{|0\rangle}(t')$ as we apply the remapping protocol. In this case, we consider only a single cycle of mapping in and mapping out, i.e. $N = 1$. The experimental data clearly shows that almost all of the population in the prepared dressed state returns to $|0\rangle$. This observation evidences a coherent, reversible population transfer between undressed and dressed states. Under the fair assumption that mapping in and mapping out yield the same transfer fidelity, such measurements further allow us to quantify the efficiency of a single state transfer. To that end, we initialize the NV spin and then repeatedly map in and out of the dressed state basis before we read out the final population in $|0\rangle$. Each set of one mapping in and one mapping out process constitutes a single 'remapping cycle'. By varying the number of remapping cycles N and reading out the population $P_{|0\rangle}(2Nt_{\mathrm{r}})$ we quantify the transfer fidelity $\mathcal{F}$ (see Fig. 4.4c). We fit the data with an exponential decay towards $1/3$, i.e.

$$\mathcal{P}(N) = \frac{2}{3}\big(\mathcal{F}^2\big)^N + \frac{1}{3}\,, \tag{4.15}$$

which yields a fidelity of $\mathcal{F} = 99.0(3)\,\%$ for a single transfer process. This transfer fidelity is experimentally limited by several reasons. These include experimental uncertainties in the fidelity of the initialization into $|0\rangle$ at the beginning of the experiment, in setting the global phase Φ, leakage of the MW signals, nonequal driving field amplitudes, and most importantly unwanted detunings of the driving fields from

the spin transitions. We calculate our ramps assuming equal driving field amplitudes and zero detunings, but deviations from these assumptions are experimentally unavoidable, and the errors generally fluctuate in time [148]. These factors are also responsible for the remaining, small oscillations in $P_{|0\rangle}(t)$ visible after state transfer in Fig. 4.3c. In App. A.3 we simulate the state preparation process with these experimental uncertainties, which allows us to reproduce the residual small wiggles consistent with the observations in the measurements.
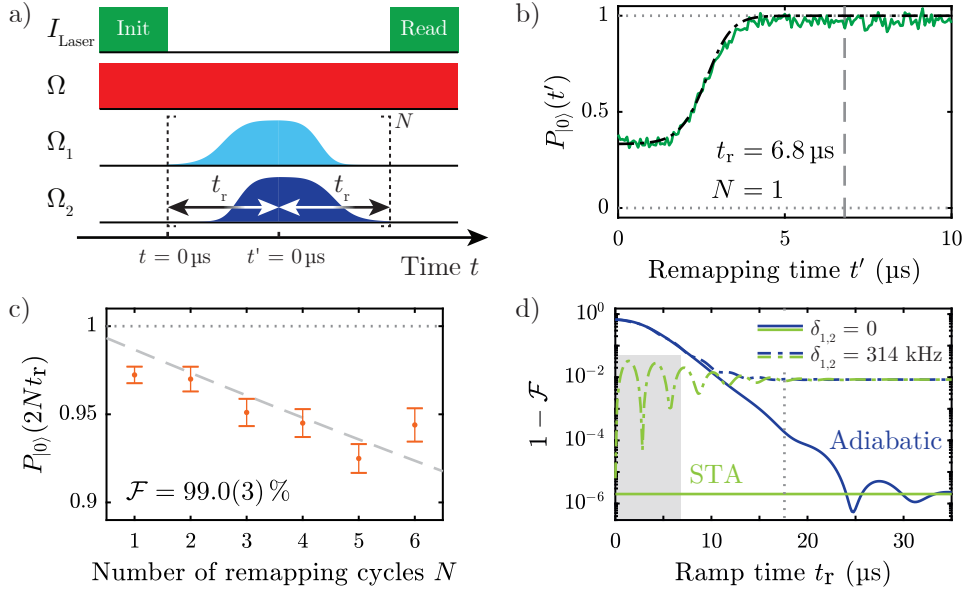

Figure 4.4.: Reverse state transfer and transfer fidelity. a) Pulse sequence employed for bidirectional state transfer. To characterize the transfer fidelity N subsequent cycles of mapping in and out of the dressed state basis are performed. b) Inverted state transfer to the NV basis after the dressed state $|\Psi_{+1}\rangle$ was prepared (single remapping cycle, $N = 1$). Measured population $P_{|0\rangle}(t')$ (green) as a function of the remapping time t' for $\nu = \Omega/2$ with corresponding simulation (black). c) Experimental transfer fidelity for various numbers of completed remapping cycles N. The exponential fit to the data (dashed line) yields a statistical transfer fidelity of $\mathcal{F} = 99.0(3)\%$. d) Theoretical transfer fidelity as a function of the ramp time t_r for the adiabatic (blue) and STA (green) transfer protocol on a logarithmic scale. Under ideal conditions the maximal achievable transfer fidelity for $\varepsilon = 10^{-3}$ is $\mathcal{F} \approx (1 - 2 \cdot 10^{-6})$ (solid lines). Considering non-zero detunings $\delta_{1,2}$ the fidelity decreases further (dashed dotted lines and see App. A.3). For the values of $\delta_{1,2}$ presented here (compare to Fig. 3.3) the transfer fidelity $\mathcal{F}$ is similar to the one determined experimentally. In this case the adiabatic and STA fidelities become the same for $t_r \approx 17.6\,\mu s$, the ramp time extracted for calculating the speedup factor (dashed gray). The grayed area corresponds to the experimentally inaccessible parameter range for the used STA protocol.
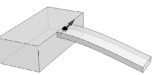
To evidence the influence of the named uncertainties, we theoretically model the transfer fidelities of the adiabatic and STA protocols in Fig. 4.4d. The logarithmic plot shows the deviation of the theoretical fidelity $\mathcal{F} = |\langle \Psi_{+1}|\psi(t_\mathrm{r})\rangle|^2$ from unity as a function of the ramp time t_r using the experimental parameters $\Omega/2\pi = 510\,\mathrm{kHz}$ and $\varepsilon = 10^{-3}$. Assuming no perturbations of the system (solid lines) a STA protocols achieves the maximal transfer fidelity of $\mathcal{F} \approx (1 - 2 \cdot 10^{-6})$, independent of t_r. The fidelity of the adiabatic protocol increases by ramping more slowly and finally converges to the maximum value of the STA transfer. The oscillatory behavior that the fidelity shows in the case of the adiabatic protocol for large t_r is a direct consequence of having only a finite duration of the ramps, which requires to cut the pulses at the beginning and the end of the ramps [185]. Thus, it is directly linked to the discontinuity ε.

To illustrate the effect of environmental fluctuations, we also show the numerically calculated fidelities for non-zero detunings, here $\delta_1/2\pi = -\delta_2/2\pi = 50\,\mathrm{kHz}$ (dashed lines, compare to Fig. 3.3). The detunings decrease the transfer fidelities for both adiabatic and STA protocol. Note that for the presented values of $\delta_{1,2}$ the theoretical transfer fidelity has the same magnitude as the one determined experimentally in Fig. 4.4c. Consequently, the adiabatic and STA fidelities correspond to each other around $t_\mathrm{r} \approx 17.6\,\mathrm{\mu s}$ (dotted gray line), the ramp time estimated for the speedup factor in the previous section. Again, the oscillations in the fidelities are attributed to the finite-time transfer pulses.

4.5. Summary

To conclude, we have shown high-fidelity, reversible initialization of individual dressed states in a closed-contour interaction scheme using state transfer protocols. Thereby, STA methods overcome the key limitation of adiabatic protocols, namely the intrinsically long ramp times and the concomitant accumulation of perturbations from the environment [173]. In contrast, STA provide fast, robust and efficient protocols. In particular, we demonstrated a more than twofold speedup over the adiabatic approach using the TD method, while we achieve state transfer fidelities $\approx 99\,\%$. The experimental results are accomplished by theoretical calculations, which yield a remarkable degree of consistency. By combining STA with closed-contour dressed states we establish a basis for future exploitation of these dressed states, which offer a close to 50-fold improvement in coherence times compared to the other continuous mechanical or MW driving schemes under similar conditions [148].

4.6. Outlook

Having shown efficient initialization of a single, pure dressed state and subsequent dressed state population readout with STA, a fundamental next step is the coherent control and manipulation of the dressed states. In Fig. 4.5 we present a first proof of principle of coherent manipulation in the dressed state basis by performing ESR and Rabi nutation measurements at $\Phi = \pi/2$. For this we apply an additional MW manipulation field with frequency $\omega_\mathrm{man}/2\pi$ and Rabi frequency Ω_man in between the STA initialization and remapping procedures (see Fig. 4.5a). By sweeping the frequency of

the manipulation field across the $|0\rangle \leftrightarrow |-1\rangle$ transition of the NV states while keeping the pulse duration of $\tau = 4.5\,\mu s$ constant, we observe the ESR spectrum shown in Fig. 4.5c. The spectrum shows two dips, corresponding to dressed state transitions at positive and negative frequencies in the rotating frame, i.e. at symmetric detunings around the bare $|0\rangle \leftrightarrow |-1\rangle$ transition frequency. Note that the two possible transitions from $|\Psi_{+1}\rangle$ to either $|\Psi_0\rangle$ or $|\Psi_{-1}\rangle$ (see Fig. 4.5b) occur at the same frequencies and are, therefore, indistinguishable in the presented ESR spectrum. Using the determined transition frequencies to resonantly drive the dressed state transitions for variable durations τ, allows us to observe coherent Rabi oscillations between dressed states (see Fig. 4.5d).
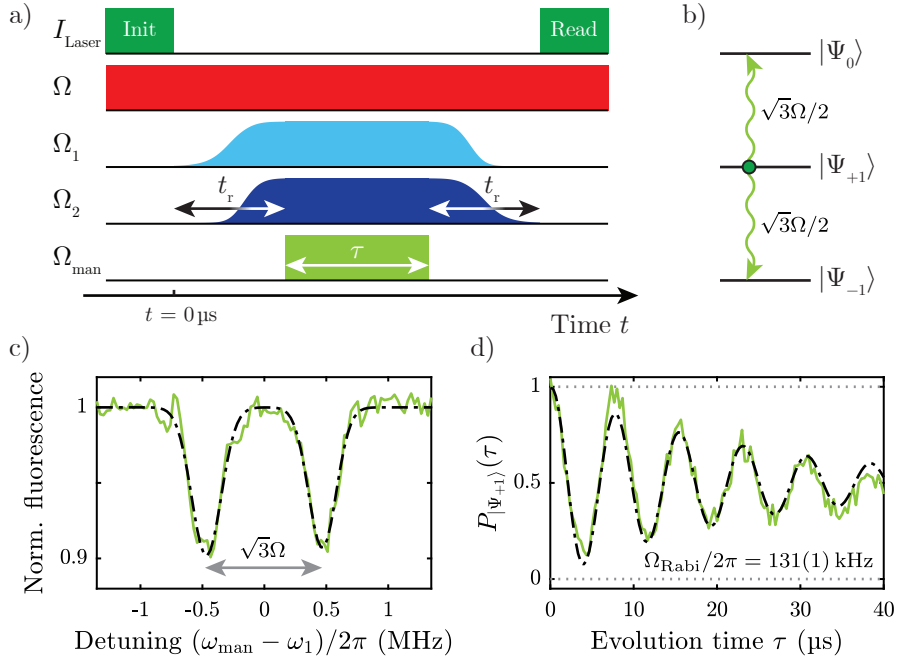

Figure 4.5.: Direct manipulation of the dressed states at $\Phi = \pi/2$. a) Pulse sequence employed for coherently manipulating the dressed states. After initialization with the STA transfer protocol, the dressed states are manipulated by an additional MW field for a duration τ. For reading out the dressed states' population the inverted STA state transfer is applied subsequently. b) Level diagram of the dressed states for $\Phi = \pi/2$. We initialize the system in $|\Psi_{+1}\rangle$ (green dot), from where we can drive the transitions to $|\Psi_0\rangle$ and $|\Psi_{-1}\rangle$, which have both the same transition frequency. c) Transition frequencies of the dressed states measured with the additional probe field Ω_{man}, which is applied for $\tau = 4.5\,\mu s$. The probe field frequency is given relative to the $|0\rangle \leftrightarrow |-1\rangle$ transition frequency $\omega_1/2\pi = 2.8672\,\mathrm{GHz}$ and the two observed dips correspond to positive and negative frequencies in the rotating frame. d) Rabi oscillations on a dressed state transition extracted from b) with $\Omega_{\mathrm{Rabi}}/2\pi = 131(1)\,\mathrm{kHz}$ and $T_{\mathrm{Rabi}} = 24(3)\,\mu s$.
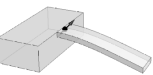
Based on these results, the coherent characterization and control of the closed-contour dressed states can be extended to arbitrary global phase values Φ. This will be discussed in more detail in Chap. 5. Looking forward, the superior coherence protection the closed-contour dressed states offer compared to the bare spin states [43, 148, 154] can be used for efficient storage of particular NV spin states on timescales much longer than the coherence times of the bare NV states by mapping to the dressed state basis [188–190]. Additionally, the possibility to initialize the dressed states in a fast and robust way in combination with the prolonged coherence times makes them attractive for ultrasensitive sensing of high-frequency magnetic fields on the nanoscale [47, 156]. Although demonstrated on an NV center in diamond here, our presented methods can be applied to other systems as well. For example, similar STA methods were proposed to be used for detection and separation of chiral, three-level molecules [191], where the chirality takes over the role of the global phase and determines the population dynamics. While for one species the nonadiabatic couplings are canceled and the population transfer is, therefore, perfect, for the other chirality the nonadiabatic couplings are enhanced, thereby hindering the state transfer. Lastly, owing to its versatility and stability, the experimental system we established here forms an attractive testbed for state transfer protocols from various STA approaches [173], which provide a variety of flexible techniques. Here, the cases $\Phi = 0, \pm\pi$ are of special interest as two of the dressed state become degenerate, thus state initialization occurs into a subspace of two degenerate dressed states. This subspace then allows for the implementation of universal geometric quantum gates, which can be sped up by STA protocols [159].

For many of these perspectives, it would, however, be advantageous to overcome a key limitation of the current system by having time-dependent amplitude control of the mechanical drive. This can be envisioned by using diamond optomechanical crystals [192–194] or surface acoustic wave structures [195–197], as they allow for full coherent control of all three driving fields.

5. Coherent control of dressed states under closed-contour interaction

For a quantum system to be fully functional in future quantum applications, it must meet several requirements [160, 198]. For example, the system must provide capabilities for initialization and readout and it must have a long coherence time. Moreover, coherent manipulation is a crucial prerequisite. This ensures that the system becomes a resource, in which a universal set of state rotations can be realized. The NV center constitutes a well-characterized spin system that satisfies the stated criteria, as it offers polarization and readout mechanisms by optical means, and spin manipulation is possible on timescales much faster than the relevant decoherence times [73].

Instead of using the bare NV spin states, it can be advantageous to utilize the states formed when the NV spin is dressed by closed-contour, continuous driving fields [148]. As shown in Chap. 3, these closed-contour dressed states are far less sensitive to dephasing from magnetic field noise than bare spin states and hence can be used to potentially increase the coherence time of the system by several orders of magnitude. Additionally, in Chap. 4 we established methods to initialize and readout the dressed states in a fast and robust way. However, full quantum control accompanied by a detailed characterization of these dressed states is an indispensable but still open requirement and, therefore, constitutes a fundamental step to develop their full potential for quantum technologies [12, 58–60].

In this chapter, we demonstrate coherent control of three-level dressed states under closed-contour driving and provide a detailed characterization of their coherence properties. To that end, we employ the dressed state initialization and readout mechanisms from Chap. 4 in combination with direct MW manipulation in the dressed state manifold based on the techniques discussed in Sec. 2.3. Specifically, we first perform phase-dependent ESR spectroscopy to identify the dressed state transition frequencies. By tuning the MW frequency to be in resonance with one of those transitions, we reveal the driven dynamics of the dressed states in terms of coherent Rabi oscillations. We then study the free (decoherence) dynamics of the system by performing phase-dependent Ramsey spectroscopy, which ultimately gives direct access to the dephasing time of the most long-lived spectral components. This measurement yields a direct comparison to the decay times determined in Chap. 3 and results in similar dephasing times up to $\approx 100\,\mu\text{s}$. We thereby directly confirm that the intrinsic coherence times of the closed-contour dressed states are significantly longer than the NV spin dephasing time of $T_2^* \approx 2\,\mu\text{s}$ and as such hold promise for prospective applications where long coherence times are required. To evaluate the ultimate limit of the coherence protection given by the relaxation time, we end the chapter by presenting T_1 relaxation measurements on the dressed states. Thus, our results enable the three-level dressed states under closed-contour driving to become a fully controllable quantum resource.
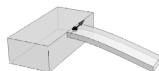
5.1. Coherent manipulation of dressed states

Our approach to realize the intended coherent control of the dressed states relies on applying additional MW pulses in between the initialization and readout processes, which we established in Chap. 4. Thereby we are able to address transitions between the dressed states and to ultimately achieve their direct manipulation. The general pulse sequence, on which all measurements presented in this chapter are based, is shown in Fig. 5.1a. We choose an adiabatic protocol for preparing and remapping the dressed states, so that the whole sequence can be applied with the same ramp functions for all values of Φ. The underlying ramps have an error-function envelope for both MW driving fields and are characterized by a fixed ramp time $t_r = 20\,\mu s$ and a discontinuity $\varepsilon = 3 \cdot 10^{-4}$ at the beginning and the end of each state transfer. Starting in the bare NV state $|0\rangle$, the initialization protocol prepares the system in $|\Psi_{+1}\rangle$ $(|\Psi_{-1}\rangle)$ for $0 < \Phi < \pi$ (for $-\pi < \Phi < 0$) or in the degenerate subspace of both states for $\Phi = 0, \pm\pi$. We then drive and manipulate the dressed states by applying a MW probe field with frequency $\omega_{man}/2\pi$ and amplitude Ω_{man}, where we use a characteristic pulse sequence for each measurement. This manipulation sequence is different for each of the following measurements and, therefore, discussed and presented in the corresponding context. Finally, we read out the dressed state population through a reversed transfer protocol followed by optical detection.

A basic requirement to perform coherent manipulation in the dressed states manifold is the determination of the corresponding dressed state transition frequencies. Consequently, we start our studies by performing phase-dependent ESR spectroscopy of the dressed states. To that end, we keep the duration of the MW manipulation pulse fixed (here $\tau = 6.8\,\mu s$, which results in the maximum contrast), while sweeping the frequency $\omega_{man}/2\pi$ of the probe field across the $|0\rangle \leftrightarrow |-1\rangle$ transition (see Fig. 5.1b). Whenever $|\omega_{man} - \omega_1|/2\pi$ is on resonance with one of the two dressed state transitions ($|\Psi_{+1}\rangle \leftrightarrow |\Psi_{0,-1}\rangle$ for $0 < \Phi < \pi$ or $|\Psi_{-1}\rangle \leftrightarrow |\Psi_{0,+1}\rangle$ for $-\pi < \Phi < 0$, respectively), we see a drop in the detected fluorescence signal. This indicates a population transfer in the dressed state basis induced by the MW field. For each value of Φ we observe four possible transitions, which consist of two pairs of dressed state transitions, one pair corresponding to positive frequencies and the other to negative frequencies in the rotating frame. Both pairs are thereby placed symmetrically relative to $\omega_1/2\pi = 2.8672\,GHz$. This can be understood by the fact that the dressed states are defined in a reference frame rotating at the frequencies ω_1 and ω_2 around appropriate axes (see Sec. 3.2 and [148]). Hence, in the lab frame, the dressed state transitions appear as positive and negative frequency components with respect to $\omega_1/2\pi$ and $\omega_2/2\pi$. Here we focus on the spectral features around $\omega_1/2\pi$ but would find identical results around $\omega_2/2\pi$.

To compare the determined transition frequencies with the theoretically predicted values for $|\Delta_{m,n}|$ (see Fig. 3.3b), we plot the theory result on top of the measured ESR data. For this we mirror $|\Delta_{m,n}|$ with respect to $\omega_1/2\pi$ to take account of the positive and negative frequency components discussed above (see Fig. 5.1b). Note that due to the initialization into $|\Psi_{+1}\rangle$ $(|\Psi_{-1}\rangle)$ we are not able to resolve the transitions at frequency $|\Delta_{-1,0}|$ $(|\Delta_{+1,0}|)$ for $0 < \Phi < \pi$ (for $-\pi < \Phi < 0$). Overall we find good agreement between measurement and calculation for $\delta_{1,2} = 0$ (colored). Just as in our observations from Sec. 3.3 deviations between theory and experiment are most
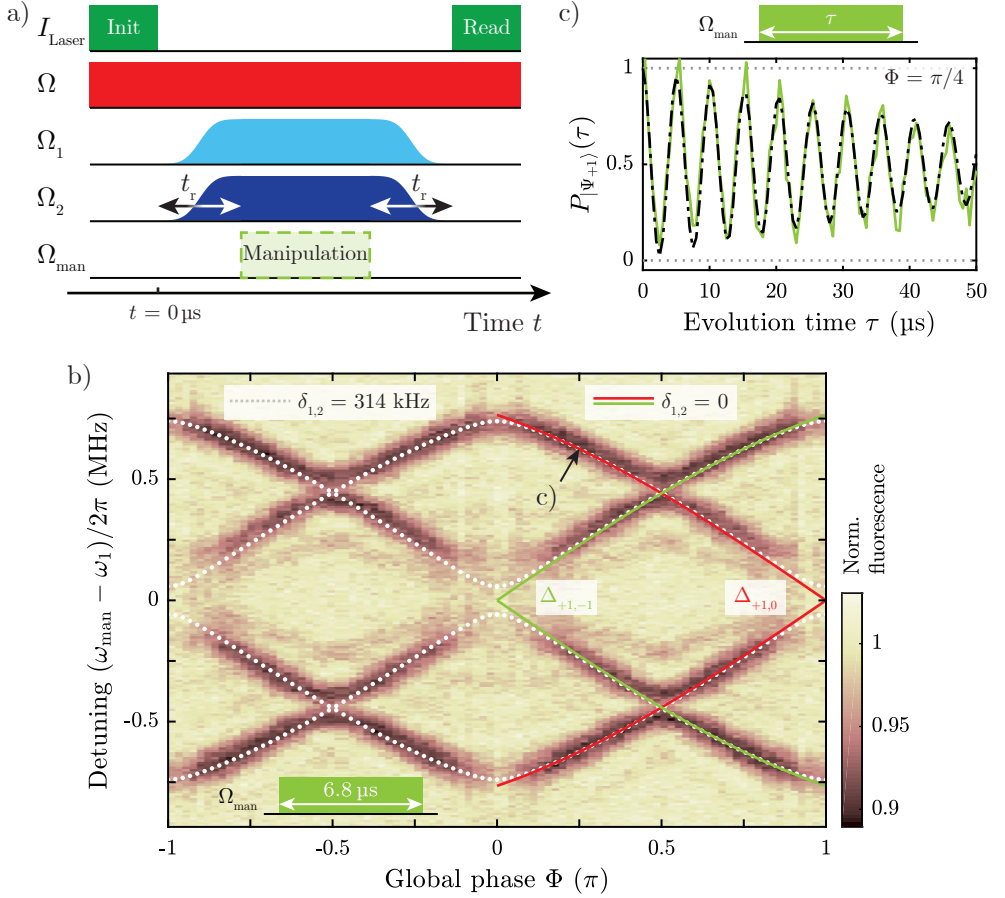
Figure 5.1.: Coherent manipulation in the dressed state manifold. a) To study the dressed states, we employ a universal pulse sequence. After the initialization process with an error-function shaped ramp ($t_r = 20\,\mu s$), we manipulate the dressed states with a MW probe field Ω_{man}. The specific manipulation sequence (here symbolically represented by the green box) for each of the following measurements is directly included in the corresponding figure. Finally, a reverse transfer protocol is used for dressed state readout. b) Phase-dependent ESR of the dressed states monitored with a fixed evolution time of $6.8\,\mu s$. The frequency of the probe field $\omega_{man}/2\pi$ is given relative to the $|0\rangle \leftrightarrow |-1\rangle$ transition of $\omega_1/2\pi = 2.8672\,\text{GHz}$. The observed transition frequencies $|\Delta_{m,n}|$ agree well with the calculated spectrum from Fig. 3.3b, here shown for zero (colored) and non-zero (dashed) detunings. c) Rabi oscillations driven on the $\Delta_{+1,0}$ dressed state transition for $\Phi = \pi/4$, demonstrating coherent control in the dressed state basis. The extracted parameters from the fit are $\Omega_{\text{Rabi}}/2\pi = 196(1)\,\text{kHz}$ and $T_{\text{Rabi}} = 57(16)\,\mu s$.
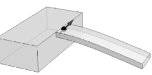
prominent at $\Phi \approx 0, \pm\pi$, where the system is most vulnerable to environmental noise. The induced coupling between two nearly degenerate dressed states results in avoided crossings, which manifest itself as a flattening of the transition frequency dispersion with Φ. Introducing non-zero detunings $\delta_{1,2} \neq 0$ in the calculation (white dotted lines, here shown for $\delta_1/2\pi = -\delta_2/2\pi = 50\,\mathrm{kHz}$) reproduces the observed experimental features (see also Sec. 3.2). In addition, around $\Phi \approx 0, \pm\pi$ we observe reduced contrast of the transitions compared to other global phase values. This is because at $\Phi \approx 0, \pm\pi$ two of the dressed states become nearly degenerate, thereby affecting the initialization and remapping processes. We no longer prepare the system in a single dressed state, but rather in a nearly degenerate subspace of dressed states. The remapping process itself also contributes errors, as the final dressed state populations are distributed over several NV states during the remapping. Therefore, only transitions to non-degenerate dressed states can be clearly identified in our spectrum.

Looking closely at the spectrum from Fig. 5.1b reveals two aspects that are not fully understood. First, there is an additional structure with less fluorescence contrast for detunings $|\omega_{\mathrm{man}} - \omega_1|/2\pi \approx 0.25\,\mathrm{MHz}$, most prominently at $\Phi \approx \pm\pi/2$. This structure is symmetric with respect to $\omega_1/2\pi$ and reproduces the course of the calculated transition frequencies. Even less pronounced there is a similar structure mirrored with respect to the calculated transition frequencies for detunings $|\omega_{\mathrm{man}} - \omega_1|/2\pi \approx 0.75\,\mathrm{MHz}$, faintly indicated at $\Phi \approx \pm\pi/2$. Both structures might be artifacts caused by higher-order resonances of the pulsed manipulation scheme we employ. While the evolution time $\tau = 6.8\,\mu\mathrm{s}$ was chosen to be a π-pulse for resonantly driving the transitions at $\Phi = \pi/3$, this pulse duration corresponds to an off-resonant '3π-pulse' at the frequencies where we observe the additional features. Such a scenario would explain the reduced contrast of the pattern and why this structure appears symmetrically around the main transitions. Second, at $\Phi = \pm\pi/2$, where the transition frequencies are supposed to cross, we observe small splittings between the transitions, indicating avoided crossings. These splittings cannot be explained by environmental fluctuations (detunings $\delta_{1,2}$) nor by unequal driving field amplitudes. We might, however, drive the system into a dark state, as at $\Phi = \pm\pi/2$ we address both transitions simultaneously. Still, this hypothesis remains speculative and requires further investigations.

Having determined the transition frequencies allows us to directly address these transitions and thereby probe the dynamics of selected dressed states, a feature that was not possible with our system before. Specifically, we focus on the manipulation of a subsystem spanned by two of the dressed states and demonstrate its coherent control by studying Rabi oscillations. To that end, we tune the frequency of the MW manipulation field in resonance with one of the transitions and vary the duration of the manipulation pulse τ. For example, choosing $\Phi = \pi/4$ and addressing the $|\Psi_{+1}\rangle \leftrightarrow |\Psi_0\rangle$ transition while monitoring the population in $|\Psi_{+1}\rangle$ results in an evolution as shown in Fig. 5.1c. The signal displays long-lasting coherent oscillations between the two dressed states. We note that such coherent manipulation is feasible for any dressed state transition and any global phase value provided that the transition frequency can be resolved (see e.g. Fig. 4.5d for coherent manipulation at $\Phi = \pi/2$). In particular, the transition frequencies of the subsystems that are supposed to offer the best coherence protection, e.g. $\Delta_{+1,0}$ for $\Phi \approx \pi/4$ and correspondingly for $\Phi \approx -\pi/4, \pm 3\pi/4$ (compare to Fig. 3.4b), are well-resolved in the ESR spectrum of Fig. 5.1b and can thus be addressed individually.

5.2. Determination of the dephasing time

Rabi oscillations represent the system's dynamics under an external drive and allow the determination of π- and $\pi/2$-pulse lengths. To observe the free (decoherence) dynamics of the dressed states we make use of Ramsey spectroscopy, to determine the dephasing time of the dressed states. This approach is in stark contrast to Fig. 3.4b, which constitutes a simultaneous measurement on all three possible dressed state subsystems, making it therefore difficult to faithfully extract individual coherence times. The technique used here, however, allows us to directly access and characterize the free induction decay of a subsystem spanned by only two dressed states. Following the results of Sec. 3.3, we focus on the most long-lived subsystems of the dressed states. Due to the underlying symmetry, we further restrict our study to phase values $0 < \Phi < \pi/2$, corresponding to the dressed state manifold of $|\Psi_{+1}\rangle$ and $|\Psi_0\rangle$.

The manipulation pulse sequence we use consists of two $\pi/2$-pulses separated by a variable delay τ. The frequency of the MW field is fixed and deliberately detuned by $\approx 200\,\text{kHz}$ from the transition frequency. This ensures the existence of Ramsey fringes at the frequency of the detuning. Fig. 5.2a shows free induction decay traces taken at $\Phi = \pi/2$ (top) and $\Phi = 0.23\,\pi$ (bottom)[1]. The decay of the Ramsey fringes gives us a direct measurement of the dephasing time of the dressed state subsystem under investigation. We extract $T_{+1,0}^{\text{dec}}$ from the data by fitting a single harmonic frequency component with a Gaussian decay envelope [128]. The dephasing times show the expected dependence on the global phase, varying from $T_{+1,0}^{\text{dec}} = 22(11)\,\mu\text{s}$ at $\Phi = \pi/2$ to $T_{+1,0}^{\text{dec}} = 94(29)\,\mu\text{s}$ at $\Phi = 0.23\,\pi$.

To investigate the dephasing of the dressed states as a function of the global phase, we repeat similar measurements for several values of Φ and especially focus on the phase values around the expected maximum at $\Phi \approx \pi/4$. The summarized results are presented in Fig. 5.2b. Note that this data set allows for a direct comparison with the decay times extracted in Fig. 3.4b and, consistent with these, we find decay times up to $T_{+1,0}^{\text{dec}} \approx 100\,\mu\text{s}$. Comparing our results with the theoretically expected dephasing times from perturbative calculations (see Sec. 3.3 and [148]) indicates that the measured dephasing times still do not reach the theoretical limit, presumably due to driving field fluctuations and temperature drifts. Despite this limitation, we still demonstrate an enhancement of the dressed states' dephasing time by a factor of ≈ 50 compared to the bare NV spin states.

---

[1]The used $\pi/2$-pulse lengths are $\tau_{\pi/2} = 1200\,\mu\text{s}$ and $\tau_{\pi/2} = 950\,\mu\text{s}$ for $\Phi = \pi/2$ and $\Phi = 0.23\,\pi$, respectively. Note that the pulse durations are slightly different as both measurements were taken under slightly different experimental conditions.
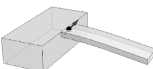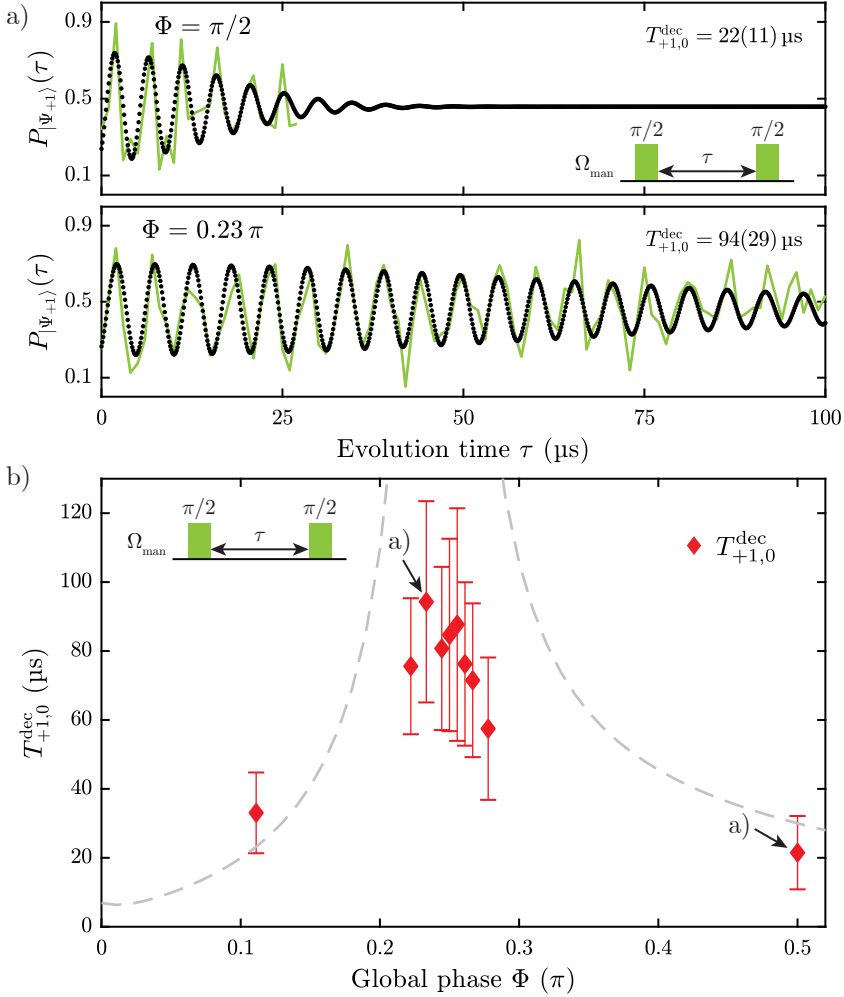
Figure 5.2.: Ramsey spectroscopy on the dressed states. a) Time evolution of $P_{|\Psi_{+1}\rangle}(\tau)$ for $\Phi = \pi/2$ (top) and $\Phi = 0.23\,\pi$ (bottom) under the pulse sequence of a free induction decay (see inset). We fit a single harmonic with a Gaussian decay envelope (black) to obtain the corresponding decay times, $T_{+1,0}^{\mathrm{dec}} = 22(11)\,\mu s$ ($\Phi = \pi/2$) and $T_{+1,0}^{\mathrm{dec}} = 94(29)\,\mu s$ ($\Phi = 0.23\,\pi$). This verifies the strong phase dependence of the dressed states' dephasing times from Fig. 3.4. b) Phase-dependent study of the dephasing time of the most long-lived dressed state subsystem ($|\Psi_{+1}\rangle$ and $|\Psi_0\rangle$) with dephasing time $T_{+1,0}^{\mathrm{dec}}$. We restrict ourselves to the range $\Phi \in [0, \pi/2]$, as the decay times of the studied spectral components are symmetric under sign changes of Φ and inflections of Φ around $\pi/2$ (see Fig. 3.4b). The theoretically calculated evolution of the decay time (dashed) [148] serves as a guide to the eye. All error bars represent 95 % confidence intervals of the fits.
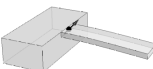
5.3. Relaxation in the dressed state manifold

In the absence of environmental and driving field fluctuations, the ultimate bound on the dephasing times of the dressed states is given by their relaxation time. To quantify the limit of the coherence protection and to characterize the inherent potential of the dressed states, we finish this chapter by studying dressed state relaxation. As we show in Sec. 2.3.3 the relaxation dynamics of a three-level system are more complex compared to a two-level system, as decay channels between all three states contribute to the total relaxation time T_1 [131]. In the case of the dressed states discussed here the situation simplifies, as they are composed of equal superpositions of the bare NV states. Therefore, the relaxation rates of the dressed states are also an equal mixture of the rates of the bare NV states and consequently the same for all the transitions (see Fig. 5.3a). Nevertheless, we confirm this line of reasoning by applying the general pulse sequence introduced in Sec. 2.3.3 and [131]. For that reason we probe the relaxation behavior of both $|\Psi_{+1}\rangle$ and $|\Psi_{-1}\rangle$ and adapt the π-pulses correspondingly (see Fig. 5.3b).

Varying the time delay τ between the initialization and readout pulses for each manipulation sequence allows us to extract the relaxation signals as a function of τ. This procedure results in an exponential decay, as shown for $\Phi = \pi/3$ in Fig. 5.3b. We find that independent of the initial dressed state the relaxation signals decay identically, which verifies that the decay rates Υ between all the dressed states are the same. The extracted characteristic decay rate is given by $\Upsilon \approx 90\,\text{Hz}$. Considering the definition of the relaxation time T_1 for a three-level system (see Sec. 2.3.3 and [131]) and assuming equal decay rates Υ, we find

$$\frac{1}{T_1} = 3\Upsilon + \Upsilon = 4\Upsilon \ . \tag{5.1}$$

Averaging both relaxation signals and evaluating Eq. (5.1) results in $T_1 = 2.8(18)\,\text{ms}$. This value of the relaxation time T_1 for the dressed states corresponds well to the one of the bare NV states, $T_1 = 2.7(9)\,\text{ms}$, determined in Sec. 2.3.3. This agreement is reasonable, as the driving fields only protect the dressed states from dephasing mechanisms, e.g. magnetic fluctuations, but not from relaxation mechanisms, e.g. coupling to phonons in the diamond lattice. Note that to ensure a fair comparison of both extracted relaxation times we perform both measurements with the same magnetic field applied, i.e. $B_\parallel = 1.82\,\text{G}$. We additionally note that the relaxation behavior of the dressed states can be studied for any global phase value, but the resulting relaxation time T_1 should not differ from the one determined here at $\Phi = \pi/3$, as we expect T_1 to be the same as for the bare NV states. Thus, the dephasing times of both the dressed states and the bare NV states are ultimately limited by the same T_1, characteristic of the spin-phonon coupling.
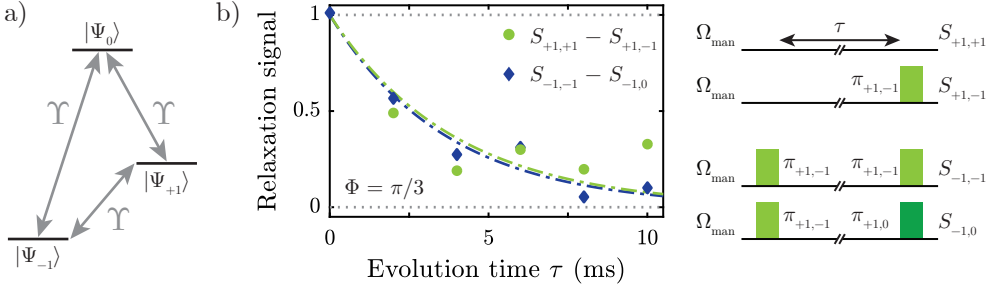
Figure 5.3.: Relaxation in the three-level system spanned by the dressed states $|\Psi_k\rangle$ for $\Phi = \pi/3$. a) Level diagram of the dressed states. The relaxation rates Υ for all possible transitions are the same. b) The manipulation sequences to extract the relaxation times are sketched on the right. Various $\pi_{m,n}$-pulses between $|\Psi_m\rangle$ and $|\Psi_n\rangle$ are used to initialize in $|\Psi_i\rangle$ and read out the population in $|\Psi_r\rangle$, giving the signal $S_{i,r}$. Independent of the initially prepared dressed state (green data for $|\Psi_{+1}\rangle$ and blue for $|\Psi_{-1}\rangle$) the decay rates determined by an exponential fit are the same, $\Upsilon \approx 90\,\text{Hz}$, which shows that all three relaxation rates in the dressed state manifold are equal. Thus, the (averaged) total relaxation time of the dressed states' three-level system is $T_1 = 1/(4\Upsilon) = 2.8(18)\,\text{ms}$, in equivalence with $T_1 = 2.7(9)\,\text{ms}$ of the bare NV states (see Sec. 2.3.3).

5.4. Summary

In conclusion, by using direct MW driving we have achieved coherent manipulation and control of the three-level dressed states. In particular, we were able to identify the transition frequencies of the dressed states through phase-dependent ESR. Building on these results, we demonstrated driven, coherent dynamics of the system in terms of Rabi oscillations, which allow all three of the dressed states to be prepared and read out individually. We subsequently performed Ramsey spectroscopy for various global phases Φ to get direct access to the dressed states' dephasing times. We confirmed the long-lived coherence of up to $\approx 100\,\mu\text{s}$ already implied in Chap. 3. Finally, to quantify the upper limit of the coherence times and to complete our detailed characterization of the dressed states, we studied their relaxation behavior and showed that their population decay rates are equivalent to the one of bare NV spin states. This indicates that the coherence of both systems is ultimately limited by the same relaxation mechanism, namely spin-lattice relaxation. Our results lay the foundation for establishing the closed-contour dressed states as a fully controllable platform, thereby opening up a wide range of possible applications in quantum technologies.

5.5. Outlook

After our complete characterization of the closed-contour dressed states, we can now turn our attention to exploiting their properties by using the established coherent control. In particular, the quasi-static dressed state dephasing mechanism could be mitigated by employing spin echo spectroscopy directly in the dressed state basis,

thereby gaining insight into the characteristics of the noise environment. To pursue this route we focus on the dressed state subsystem spanned by $|\Psi_{+1}\rangle$ and $|\Psi_0\rangle$ and investigate the system's dynamics under the spin echo sequence for various values of $\Phi > 0$. This procedure ultimately allows us to determine the homogeneous coherence time T_2. To that end, an additional π-pulse positioned symmetrically between the two $\pi/2$-pulses is inserted in the Ramsey sequence to refocus the dephasing spins. The MW pulses are on resonance with the selected dressed state transitions, and their duration has been determined by prior Rabi measurements.

In Fig. 5.4 we present preliminary experimental results of spin echo spectroscopy for two different global phase values, $\Phi = 0.23\,\pi$ and $\Phi = \pi/3$, with $\tau_\pi = 2.9\,\mu$s and $\tau_{\pi/2} = 1.4\,\mu$s for both measurements. Contrary to our expectations based on a free induction decay time $\approx 100\,\mu$s, we observe a fast decay of the signal within $< 10\,\mu$s in both measurements. After this initial decay the signal still shows a certain oscillatory behavior with periods of $\approx 30\,\mu$s and $\approx 17\,\mu$s for Fig. 5.4a and b, respectively. We made similar observations for other phase values and observed such oscillatory behavior with differing periods between each of the measurements, even for the same Φ. This indicates an origin in environmental fluctuations, e.g. temperature, or experimental uncertainties, e.g. in defining the pulse durations. The fast initial decay in the observed signal is yet unclear, as we expect the coherence times T_2 to far exceed the dephasing times $T_{+1,0}^{\text{dec}}$. We speculate that the decay results from limitations in the applied pulses. The MW pulses should be as short as possible to ensure fast coherent control of the states, i.e. the applied manipulation pulse amplitude Ω_{man} should be large. In our experiments, however, the amplitude is constrained by the splitting of the two dressed states under investigation to avoid populating the third uninvolved state. The latter condition ($\Omega_{\text{Rabi}}/2\pi \leq 200\,$kHz for $\Phi \approx \pi/4$) sets a lower bound for the π-pulse length of $\approx 2.5\,\mu$s, close to the value used in Fig. 5.4. We believe that
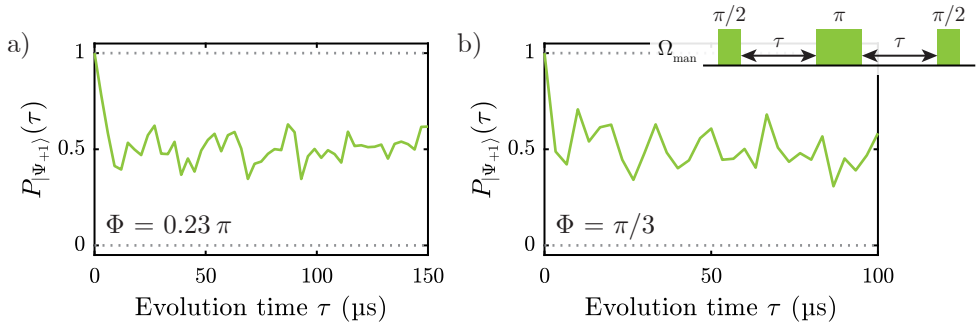

Figure 5.4.: Spin echo manipulation on the dressed state transition $|\Psi_{+1}\rangle \leftrightarrow |\Psi_0\rangle$ for two different global phase values, a) for $\Phi = 0.23\,\pi$ and b) for $\Phi = \pi/3$. The pulse sequence is shown in the inset, with $\tau_\pi = 2.9\,\mu$s and $\tau_{\pi/2} = 1.4\,\mu$s for both measurements. Both time evolutions decay within $< 10\,\mu$s, and then the signal shows a periodically oscillating behavior around the steady state level of ≈ 0.5. Similar spectra were also observed for other values of Φ, but are currently not understood. While the oscillations might be attributed to the interaction with $|\Psi_{-1}\rangle$, the fast decay could be caused by uncertainties in setting the experimental parameters.
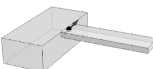
shorter pulse lengths are required to minimize decoherence effects during the control pulses and to ultimately resolve a spin echo of the dressed states. This limitation on the pulse length could be lifted by using larger driving field amplitudes $\Omega_{1,2,3}$, which would be feasible with advanced mechanical resonator structures [192–195]. Another approach to mitigate pulse errors is to use phase-controlled manipulation pulses, i.e. to rotate the states along different axes during the π- and $\pi/2$-pulses, respectively [124]. By changing the amplitude field's phase by 90° during the π-pulse, the corresponding state rotation might be more stable with respect to experimental uncertainties.

Coherent manipulation and spin echo spectroscopy are the basic building blocks for studying advanced decoupling sequences [124]. From a far-reaching perspective, our experiments consequently open up new avenues to employ noise spectroscopy [87] or dynamical decoupling [32–34], directly in the dressed state manifold. Unknown details of the remaining dressed state dephasing mechanisms could thereby be explored. In addition, our approach to combine continuous closed-contour and pulsed dynamical decoupling can be extended to more sophisticated pulse techniques. As theoretically studied in the context of mixed dynamical decoupling [48], such schemes might improve the robustness to amplitude fluctuations of the driving fields and thus prolong coherence times even further.

6. Determination of intrinsic effective fields and MW polarization analysis

The three-level dressed states extensively discussed and characterized in the previous chapters hold promise for high sensitivity sensing due to their long dephasing times. As for the NV itself and other defects in the solid-state, harnessing such a quantum system as a nanoscale sensor for external fields requires precise characterization of the local internal field environment, since the strength of intrinsic fields can be comparable to desired external signals [115]. Specifically, intrinsic fields arising from lattice strain, paramagnetic impurities, and electric fields induced by surface charges limit the system's ability to detect and characterize external fields of interest. Techniques operating at low magnetic fields, such as zero-field nuclear magnetic resonance [199, 200] and low-field magnetometry [201] are especially vulnerable to these parasitic fields. Their relevance and future prospects motivate extended studies to carefully characterize the environment surrounding single NV spins.

High-resolution spectroscopy offers a set of tools to study the interaction of various local intrinsic and externally applied fields. For example, NV ensembles in type-Ib diamond were probed with MW fields at zero magnetic field to investigate intrinsic effective fields, which represent the combined effects of strain and electric fields [82, 115]. This ensemble study revealed that for the particular diamonds under study, the electric field was the dominant contribution to the effective field. A similar technique was used to determine the orientation of single NVs [202] by simultaneously applying external electric and magnetic fields. However, a systematic study of the effective fields for individual NVs in high purity diamond has not been reported so far.

In this chapter, we present high-resolution, low-power ESR spectroscopy on individual NV centers in high purity, type-IIa diamond at and around zero magnetic field. The experimentally observed transitions depend sensitively on the interplay between the MW probing field and the local intrinsic effective field comprising strain and electric fields, which act on the NV spin. Based on a theoretical model of the magnetic dipole transitions and the MW driving field, we extract both the strength and the direction of the transverse component of the effective field. In contrast to the results mentioned above [115], we find that in our samples the strain contribution to the effective field dominates over the electric field. We tentatively assign this discrepancy to the higher dopant density in the samples of [115]. Moreover, we study hyperfine interaction between a single NV and an individual, nearby ^{13}C nuclear spin. Finally, as an additional outcome of our studies, we find that by applying external magnetic fields and exploiting the magnetic dipole selection rules we can directly probe the polarization of the MW field at the NV position. Thus, our results are of importance to low-field quantum sensing applications using NV spins and form a relevant addition to the ever-growing toolset for spin-based quantum sensors.

Most of the results presented here have been published in [116].
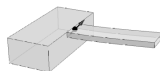
6.1. Characterizing the effective field

In the following experiments, we perform ESR measurements on a selection of individual NVs, and thereby extract information about their local environment. Quantitative analysis of our results requires a detailed understanding of the NV spin transition strengths under ESR driving at low fields. Based on the NV's ground state spin Hamiltonian in the presence of magnetic, electric, and strain fields (see Sec. 2.2), we present a model to describe how these fields influence the selection rules of the magnetic dipole spin transitions introduced in Sec. 2.3.1. We then calculate the transition magnetic dipole moments and thereby the fluorescence signal we expect to observe in our experiments. By comparing our theory to the experimental data, we are then able to directly characterize the local strain and electric field environment.

6.1.1. Influence on the level structure

Following the discussions of Sec. 2.1.2 and Sec. 2.2, the Hamiltonian of the NV ground state in the presence of magnetic, electric, and strain fields reads

$$\hat{\mathcal{H}}/h = (D_0 + \Pi_z)\hat{S}_z^2 + \gamma_{\text{NV}}\boldsymbol{B} \cdot \hat{\boldsymbol{S}} + A_{\text{HF}}\hat{S}_z\hat{I}_z +$$
$$+ \Pi_x\left(\hat{S}_y^2 - \hat{S}_x^2\right) + \Pi_y\left(\hat{S}_x\hat{S}_y + \hat{S}_y\hat{S}_x\right) . \quad (6.1)$$

The magnetic field $\boldsymbol{B} = (B_x, B_y, B_z)$ and the effective field $\boldsymbol{\Pi} = (\Pi_x, \Pi_y, \Pi_z)$ are given in the coordinate frame (xyz) of the NV, where z denotes the NV's symmetry axis and we choose y to lie in one of the NV's symmetry planes (see Fig. 6.1a).

To quantify the influence of the effective field $\boldsymbol{\Pi}$ on the NV hyperfine states $|m_s, m_I\rangle$ (see Fig. 6.1b, left), it is convenient to express the field vectors in components parallel and perpendicular to the NV axis. In particular, we write the partition of the effective field vector as $\boldsymbol{\Pi} = (\Pi_\perp \cos\varphi_\Pi, \Pi_\perp \sin\varphi_\Pi, \Pi_\parallel)$ (see Fig. 6.1a), where $\Pi_\parallel = \Pi_z$ is the parallel and $\Pi_\perp = (\Pi_x^2 + \Pi_y^2)^{1/2}$ the perpendicular effective field amplitude. The direction of $\Pi_\perp$ in the transverse xy-plane is set by the azimuthal angle φ_Π with respect to the x-axis, i.e. $\tan\varphi_\Pi = \Pi_y/\Pi_x$. We will treat $\boldsymbol{B}$ the same, with $B_\parallel$, $B_\perp$ and φ_B defined similarly.

According to Hamiltonian (6.1), the effective field then affects the level structure in two ways (see Sec. 2.2.2): First, an axial effective field shifts all $|-1, m_I\rangle$ and $|+1, m_I\rangle$ with respect to $|0, m_I\rangle$ by an amount $\Pi_\parallel$. Second, a transverse effective field couples $|-1, m_I\rangle$ and $|+1, m_I\rangle$, whenever they are near-degenerate. For example, for $\boldsymbol{B} = 0$, the transverse effective field mixes and splits the degenerate $|-1, 0\rangle$ and $|+1, 0\rangle$, leading to new spin eigenstates given by

$$|-\rangle = \left(e^{i\varphi_\Pi}|+1\rangle + |-1\rangle\right)/\sqrt{2} ,$$
$$|+\rangle = \left(e^{i\varphi_\Pi}|+1\rangle - |-1\rangle\right)/\sqrt{2} , \qquad (6.2)$$

where we have omitted the label for the nuclear spin projection $m_I = 0$ for clarity. The corresponding eigenenergies are $E_\pm = D_0 + \Pi_\parallel \pm \Pi_\perp$ as shown in Fig. 6.1b (right). Thus, besides the level shift of $\Pi_\parallel$ experienced by all nuclear spin projections, the coupled states $|-\rangle$ and $|+\rangle$ are split by $2\Pi_\perp$ due to the presence of the effective field.

We stress that the spin is far more susceptible to transverse effective fields when the electric field dominates, since the electric field susceptibilities fulfill $d_\perp \approx 50 d_\parallel$ [112] (see Fig. 2.3). In contrast, all spin-strain susceptibilities are comparable [104–106]. As a result, the average effect of a randomly oriented electric field leads to a large splitting with negligible common-mode shift (i.e. $\Pi_\perp \gg \Pi_\parallel$, on average), while in the case of strain the splitting is accompanied by a common-mode shift in the same
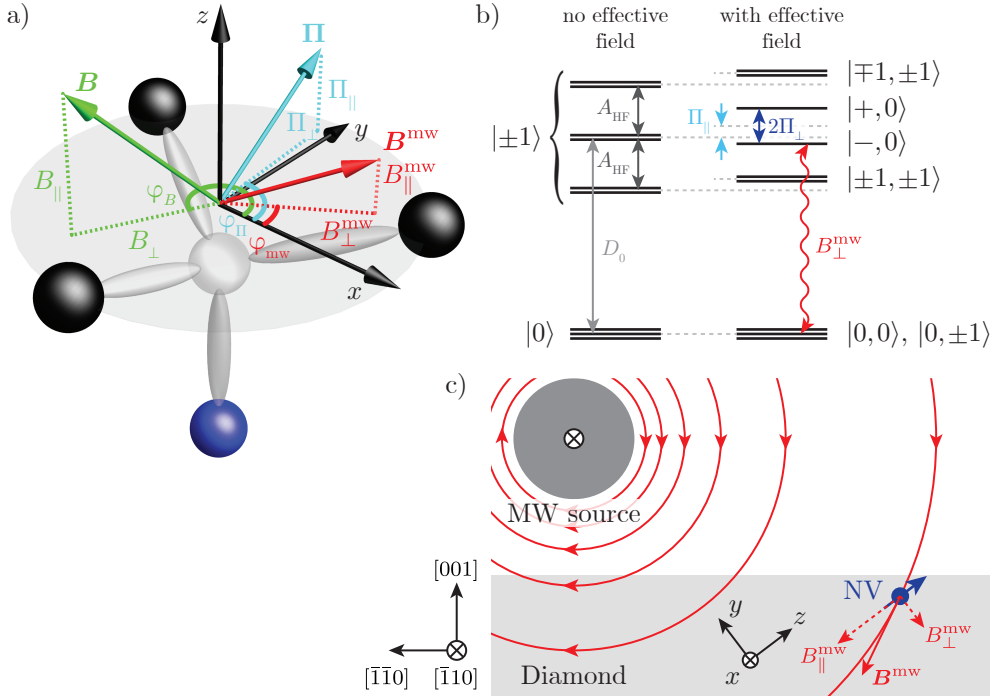

Figure 6.1.: Schematics and description of the experiment. a) Coordinate system of the NV center including the relevant fields interacting with the NV spin: The MW magnetic field (red) for spin manipulation, the effective field comprising strain and electric field (light blue) intrinsic to the diamond sample and the static magnetic field (green) externally applied to determine unknown MW polarizations. All fields are partitioned into components parallel and perpendicular to the NV symmetry axis, where the perpendicular components are further parametrized by the azimuthal angle φ_α ($\alpha \in \{mw, \Pi, B\}$). b) Simplified level diagram of the NV ground state according to Hamiltonian (6.1) without and with an effective field in absence of a magnetic field. The effective field induces a common-mode shift of the $|-1\rangle$ and $|+1\rangle$ hyperfine states by $\Pi_\parallel$ and additionally splits near-degenerate levels, which have the same nuclear spin projection (here $m_I = 0$). A MW magnetic field is used to address transitions between the states. c) Sketch of the experimental setup with a diamond sample and a nearby bonding wire for MW delivery. The NV spin under study experiences an approximately linear polarized field, which is used to manipulate the NV spin (the situation shown corresponds to the one of NV1).
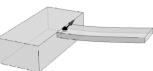
order of magnitude (i.e. $\Pi_\perp \approx \Pi_\parallel$, on average). This key difference allows high-resolution spectroscopy of NV spins to differentiate between the electric field and strain contributions of the effective field, as we will show in the following.

Note that although we focus here on the case $\boldsymbol{B} = 0$ and $m_I = 0$, analogous statements hold for the case $\gamma_{\mathrm{NV}} B_\parallel = \pm|A_{\mathrm{HF}}|$ and $m_I = \pm 1$.

6.1.2. Influence on the magnetic dipole transition strengths

In addition to shifting and splitting the hyperfine states, the effective field $\boldsymbol{\Pi}$ also influences the dipole moment of the spin transitions (see Sec. 2.3.1). Experimentally, these spin transitions are probed by a MW field $\boldsymbol{B}^{\mathrm{mw}}(t) = \boldsymbol{B}^{\mathrm{mw}} \cos(\omega_{\mathrm{mw}} t)$ with frequency $\omega_{\mathrm{mw}}/2\pi$ and (complex) amplitude $\boldsymbol{B}^{\mathrm{mw}}$, which interacts with the corresponding magnetic dipole moment. As the dipole moment determines the polarization response of the transition, it is ultimately linked to the observed transition strengths.

Based on the discussion in Sec. 2.3.1, the Rabi frequencies associated with the resonant spin transitions $|0\rangle \leftrightarrow |\pm\rangle$ read

$$\Omega_{0,\pm} = \frac{1}{\hbar}|\langle\pm|-\boldsymbol{B}^{\mathrm{mw}} \cdot \hat{\boldsymbol{\mu}}|0\rangle| = \frac{1}{\hbar}\left|\boldsymbol{B}^{\mathrm{mw}} \cdot \boldsymbol{\mu}_{0,\pm}\right| , \tag{6.3}$$

where the magnetic dipole moment operator is $\hat{\boldsymbol{\mu}} = -h\gamma_{\mathrm{NV}}\hat{\boldsymbol{S}} = -2\mu_B\hat{\boldsymbol{S}}$ and the related magnetic dipole matrix elements are

$$\boldsymbol{\mu}_{0,\pm} = \langle\pm|\hat{\boldsymbol{\mu}}|0\rangle = -2\mu_B\left\langle\pm\left|\hat{\boldsymbol{S}}\right|0\right\rangle . \tag{6.4}$$

Using Eq. (6.2) we then find

$$\begin{aligned}
\boldsymbol{\mu}_{0,+} &= -2\mu_B\big(\sin\left(\varphi_\Pi/2\right), \cos\left(\varphi_\Pi/2\right), 0\big) , \\
\boldsymbol{\mu}_{0,-} &= -2\mu_B\big(\cos\left(\varphi_\Pi/2\right), -\sin\left(\varphi_\Pi/2\right), 0\big) ,
\end{aligned} \tag{6.5}$$

showing that the azimuthal angle of the effective field is directly linked to the orientation of both dipole moments. Note that the dipole moments are completely real, implying a linearly polarized response of the transitions. In contrast, when $B_\parallel \gg \Pi_\perp$, the eigenstates of Hamiltonian (6.1) are $|0\rangle, |-1\rangle$, and $|+1\rangle$, and the transitions show the familiar circularly polarized response (compare to Eq. (2.17)).

The relative orientation of the dipole moment to the MW field determines the Rabi frequency of the transition and, therefore, the observed ESR response (see Eq. (6.3)). The observed transition strengths are then given by $\mathcal{A}_{0,\pm} \propto \Omega_{0,\pm}^2$ [122]. Writing the linearly polarized MW field amplitude as $\boldsymbol{B}^{\mathrm{mw}} = (B_\perp^{\mathrm{mw}} \cos\varphi_{\mathrm{mw}}, B_\perp^{\mathrm{mw}} \sin\varphi_{\mathrm{mw}}, B_\parallel^{\mathrm{mw}})$, where φ_{mw} is the azimuthal angle in the xy-plane (see Fig. 6.1a), the transition strengths between $|0\rangle$ and $|-\rangle$ or $|0\rangle$ and $|+\rangle$ read

$$\mathcal{A}_{0,\pm} \propto \frac{1}{\hbar^2}\frac{(2\mu_B B_\perp^{\mathrm{mw}})^2}{2}[1 \mp \cos(2\varphi_{\mathrm{mw}} + \varphi_\Pi)] . \tag{6.6}$$

Interestingly, the transition strengths contain information about the relative azimuthal angles of the effective field and the linearly polarized MW driving field.

Adapting the formalism of [115] this information can be directly accessed from the transition imbalance

$$\mathcal{I} = \frac{\mathcal{A}_{0,+} - \mathcal{A}_{0,-}}{\mathcal{A}_{0,+} + \mathcal{A}_{0,-}} = -\cos(2\varphi_{\mathrm{mw}} + \varphi_\Pi) \, , \tag{6.7}$$

which is provided by contrast difference of the ESR transitions. Thus, the azimuthal angle φ_Π of the effective field $\boldsymbol{\Pi}$ can be determined up to a reflection symmetry with respect to $2\varphi_{\mathrm{mw}}$ from the contrast imbalance of the ESR transitions, while the magnitude of $\Pi_\perp$ can be extracted from the splitting of the ESR transition frequencies. Hence, we have established that both the direction and the magnitude of the transverse effective field can be extracted from high-resolution ESR.

As mentioned earlier, the $m_I = \pm 1$ hyperfine projections are coupled by the effective field $\boldsymbol{\Pi}$ as well. At $\boldsymbol{B} = 0$, however, the corresponding hyperfine states with the same m_I are split by $2|A_{\mathrm{HF}}|$, so that the transition imbalance due to the effective field is mostly suppressed. As we typically find $\Pi_\perp \ll |A_{\mathrm{HF}}|$ in our samples, an approximate expression for the imbalance is given by

$$\mathcal{J} \approx -\frac{\Pi_\perp}{|A_{\mathrm{HF}}|} \cos(2\varphi_{\mathrm{mw}} + \varphi_\Pi) \, , \tag{6.8}$$

as derived in App. A.5.

6.2. High-resolution spectroscopy

In order to apply our findings from the previous section to investigate the effective field $\boldsymbol{\Pi}$ and to determine the respective weights of the electric field and strain, we perform high-resolution spectroscopy on single NV centers using the same sample and experimental setup as introduced in Sec. 3.1. Note that the fabrication steps performed to structure the cantilevers, e.g. etching, possibly cause a larger intrinsic strain in the diamond compared to an untreated sample.

For our low-power ESR measurements we make use of MW manipulation of the NV spins. More precisely the circularly polarized component of the MW field projection transverse to the NV axis, $B_\perp^{\mathrm{mw}}$ (see Fig. 6.1a), allows us to drive transitions between different spin levels with the same m_I, as illustrated with the red arrow in Fig. 6.1b. We realize this MW driving by applying an AC current to the gold wire acting as a MW source. This configuration leads to an approximately linearly polarized MW field at the NVs' locations as sketched in Fig. 6.1c. Note that we employ a pulsed ESR technique, in which the MW pulse duration exceeds $T_2^* \approx 2\,\mu\mathrm{s}$ of the NV spins. In this regime of incoherent manipulation, the observed transition characteristics are then described by the theory introduced in Sec. 6.1.

Geometric considerations allow us to determine the MW polarization angle required to interpret the experimental data (see Fig. 6.1 and compare to Eq. (6.7)). We find $\varphi_{\mathrm{mw}} \approx 90°$ for the specific orientation of a particular single NV ('NV1')[1]. We note that in Sec. 6.5 we will present a technique to determine this MW polarization angle without the requirement of such a geometric consideration. This technique, which is based on the controlled rotation of a large transverse magnetic field, yields very good agreement with our *a priori* determination of φ_{mw}.

---

[1]NV1 is the NV center on which all measurements in the previous chapters were performed on.
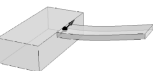
6.2.1. Spectroscopy around zero magnetic field

We start the characterization of our sample by investigating the response of NV1 to external magnetic fields. To that end, we first apply an axial magnetic field and record low-power, (incoherent) pulsed ESR measurements [122] as a function of $B_\parallel$ (see Fig. 6.2a). The resulting spectrum shows the six hyperfine resolved spin transitions. Due to the Zeeman effect, the three nuclear spin projections with $m_s = +1$ ($m_s = -1$) show a positive (negative) dispersion with magnetic field, i.e. shift to larger (smaller) frequencies with increasing $B_\parallel$, as described in Sec. 2.2.1. The order of the nuclear spin projections can be established from Hamiltonian (6.1) (see Fig. 6.2a). At and above the maximum values of $B_\parallel$ we apply, all six ESR transitions show the same contrast, as
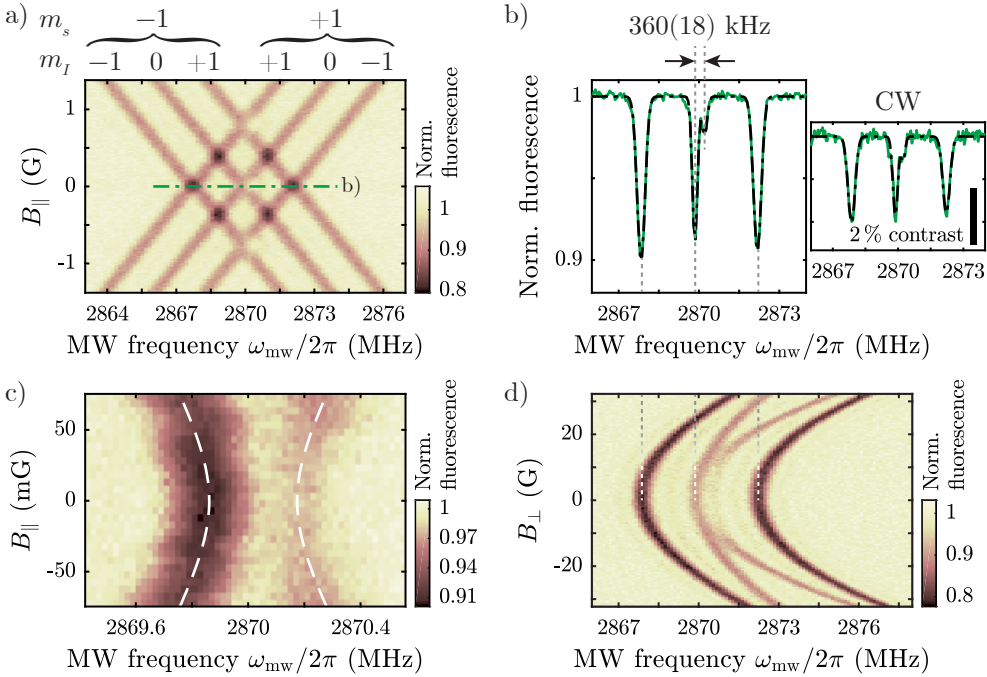

Figure 6.2.: Influence of external fields on the ESR transitions. a) A magnetic field $B_\parallel$ parallel to the NV axis results in a linear Zeeman splitting of the six possible spin transitions $|0\rangle \leftrightarrow |\pm1\rangle$. Whenever two transitions with the same nuclear spin quantum number m_I cross, we observe a reduced ESR contrast, resulting from a coupling of the corresponding states. b) High-resolution spectrum recorded at $B_\parallel = 0\,\mathrm{G}$ with incoherent MW manipulation including a Gaussian fit to the data (black). The central line is split by $360(18)\,\mathrm{kHz}$ into two transitions with an imbalance $\mathcal{I} = -58(5)\,\%$. The inset shows a control measurement recorded with CW ESR, which confirms the validity of the result. c) Zoom into the $m_I = 0$ transitions around $B_\parallel \approx 0\,\mathrm{G}$ showing a clear avoided crossing, indicative of a coupling between the two involved hyperfine levels. d) Applying a transverse magnetic field $B_\perp$ while maintaining $B_\parallel \approx 0\,\mathrm{G}$ mixes the spin levels and results in a second-order energy shift (see Sec. 2.2.1 and Sec. 6.5).

the nuclear spin states are equally (thermally) populated, and the $m_s = -1$ ($m_s = +1$) transitions have right (left) circularly polarized response, whereas we apply a linearly polarized MW field, which corresponds to an equal superposition of right and left circular polarization. At the field values, where the transitions corresponding to different m_I cross, no state mixing occurs and the transition contrasts, which are related to the strengths of both transitions, then sum together, resulting in twice the fluorescence drop compared to a single transition. When two states, which cross in energy, have the same nuclear spin projection m_I, however, the states do mix and we observe stark differences to the case of states of unequal m_I crossing.

To investigate this effect in more detail, we record a high-resolution ESR spectrum at $\boldsymbol{B} = 0$ (see Fig. 6.2b). The spectrum shows a clear splitting of the central transition into two peaks, both having different amplitudes. This imbalance is attributed to the influence of the effective field $\boldsymbol{\Pi}$, which mixes $|-1, 0\rangle$ and $|+1, 0\rangle$. Fitting the experimental data with a superposition of four Gaussian functions allows us to extract a splitting of $2\Pi_\perp = 360(18)\,\text{kHz}$ and a transition imbalance of $\mathcal{I} = -58(5)\,\%$. Note that for consistency, we also obtained the same results by using CW ESR, instead of incoherent pulsed ESR (see Fig. 6.1b inset).

To ensure that our findings are not masked by any residual parallel magnetic field, we perform high-resolution ESR measurements with the parallel magnetic field component in the vicinity of the $m_I = 0$ transition crossing (see Fig. 6.2c). We clearly resolve an avoided crossing of the two transitions, as illustrated by the dashed white line and consistent with the discussed coupling of the corresponding hyperfine states. Note that all the measurements presented in Fig. 6.2 and the following are recorded separately and hence under slightly different experimental conditions (e.g. temperature), leading to small variations in the zero-field splitting [107].
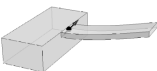
6.2.2. Comparison of transition strengths

To quantify the strengths of the involved ESR transitions in Fig. 6.2b, we conduct Rabi oscillation experiments on each transition using the same MW and laser power (see Fig. 6.3). Note that the MW power used here is higher compared to the measurements shown in Fig. 6.2 allowing for coherent manipulation. Employing Eq. (2.17) and Eq. (6.5) directly yields a relation between the Rabi frequencies Ω_i ($i = 1, 2, 3, 4$) of the four different transitions, which reads

$$\Omega_1^2 = \Omega_4^2 = \frac{1}{2}\left(\Omega_2^2 + \Omega_3^2\right) . \tag{6.9}$$

Here, we labeled the transitions as shown in Fig. 6.3 and defined $\Omega_1^2 = \Omega_4^2 = 2(\mu_B B_\perp^{\text{mw}})^2/\hbar^2$. In close agreement with this prediction, we find from fits to our data that $\Omega_1/2\pi = 220(1)\,\text{kHz} \approx \Omega_4/2\pi = 210(1)\,\text{kHz}$ and $[\frac{1}{2}(\Omega_2^2 + \Omega_3^2)]^{1/2}/2\pi = 220(3)\,\text{kHz}$, where $\Omega_2/2\pi = 288(2)\,\text{kHz}$ and $\Omega_3/2\pi = 118(6)\,\text{kHz}$.

The measured transition strengths are directly linked to the polarization response of each transition (see Fig. 6.3, right). Transitions ① and ④ each involve two $\Delta m_s = \pm 1$ transitions, such that they both show circular polarization responses. In contrast, transitions ② and ③ correspond to transitions from $|0\rangle$ to $|-\rangle$ and $|0\rangle$ to $|+\rangle$, respectively (both with $m_I = 0$, see Eq. (6.2)). These states are even and odd superpositions of $|-1\rangle$ and $|+1\rangle$ and the transitions, therefore, yield a linearly polarized response (see
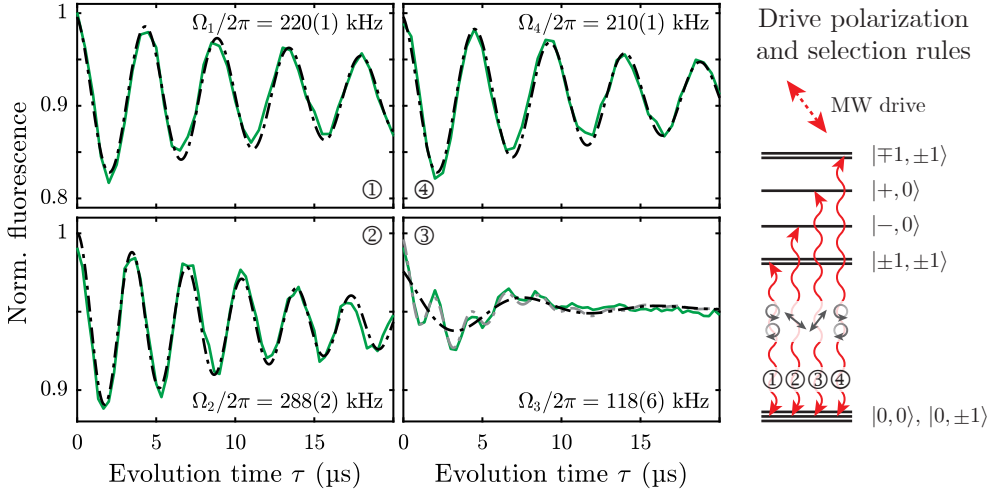
Figure 6.3.: Comparison of the transition strengths measured at $B_\parallel = 0\,\mathrm{G}$ by driving Rabi oscillations on each of the four transitions shown on the right under the same experimental conditions. To high accuracy we find the expected relation $\Omega_1^2 = \Omega_4^2 = \frac{1}{2}(\Omega_2^2 + \Omega_3^2)$. Note that panel ③ contains two oscillation frequencies, the slowly oscillating component of transition ③ (black) and a higher frequency caused by off-resonant driving of transition ②. The level diagram additionally shows the polarization of the MW drive and the polarization response of each transition.

Eq. (6.5)). Since the polarization of the MW drive is approximately linear, the overlap of the drive polarization and the transition dipole determine the transition strengths (refer to Eq. (6.3)).

We note that in the experimental data for transition ③, there are two oscillation frequencies present (see gray fit). The slowly oscillating component highlighted by the black line corresponds to driving of transition ③, while the quickly oscillating component originates from off-resonant driving of transition ②. Additionally, the slight mismatch between Ω_1 and Ω_4 results from coupling between the states $|-1, m_I\rangle$ and $|+1, m_I\rangle$ with the nuclear spin quantum numbers $m_I = \pm 1$ even at $\boldsymbol{B} = 0$. This slight mixing, which is suppressed by the hyperfine splitting $2|A_{\mathrm{HF}}|$, still causes the transitions to have an observable, slightly elliptically polarized response, rather than a purely circularly polarized response.

6.3. Characterization of individual NV centers

Having established a technique to characterize the effective field $\boldsymbol{\Pi}$ a single NV experiences, we now apply this method to investigate the field environment of a selection of individual NVs. For that we perform high-resolution ESR measurements at $\boldsymbol{B} = 0$ as outlined in Sec. 6.2.1 and study the splitting and transition imbalance of the $m_I = 0$ transitions (see Fig. 6.4a). In this we find different behavior for each NV under study, indicating a different effective field environment for each defect. Comparing the mean

transition frequency for each NV with the averaged transition frequency over all NVs, we find that the observed shifts and splittings are of the same order of magnitude, which indicates that strain is the dominant contribution to the effective field. This observation differs from the findings of [115], where the electric field originating from charge impurities was identified as the main effective field contribution in their samples.

We note that our method does not allow for a complete determination of the effective field, since we are not able to reliably determine the parallel component $\Pi_\parallel$. This is because the zero-field splitting depends sensitively on temperature (see Sec. 2.2.3), i.e. both temperature and the parallel effective field component have the same effect on the observed transition frequencies. Nevertheless, our conclusion of strain being the major contribution to the effective field holds, as we typically observe peak-to-peak temperature fluctuations of $0.3\,\mathrm{K}$ in our setup corresponding to temperature-induced shifts of $\approx 23\,\mathrm{kHz}$, much smaller than the shifts observed in Fig. 6.4a.

Using Gaussian fits we extract the splittings $2\Pi_\perp$ and transition imbalances $\mathcal{I}$ for each ESR spectrum in Fig. 6.4a and summarize the results in Fig. 6.4b. Eq. (6.7) allows us to visualize the transverse effective field components in the NV frames up to a reflection symmetry with respect to $2\varphi_\mathrm{mw}$ as presented in the inset of Fig. 6.4b. Here, the transverse effective field amplitudes are normalized with respect to NV1 and we used the MW polarization angle of NV1 as determined in the Sec. 6.5. Note that Fig. 6.4 shows NVs with all four possible orientations in the diamond lattice, which experience different relative MW polarization angles accordingly and, therefore, show
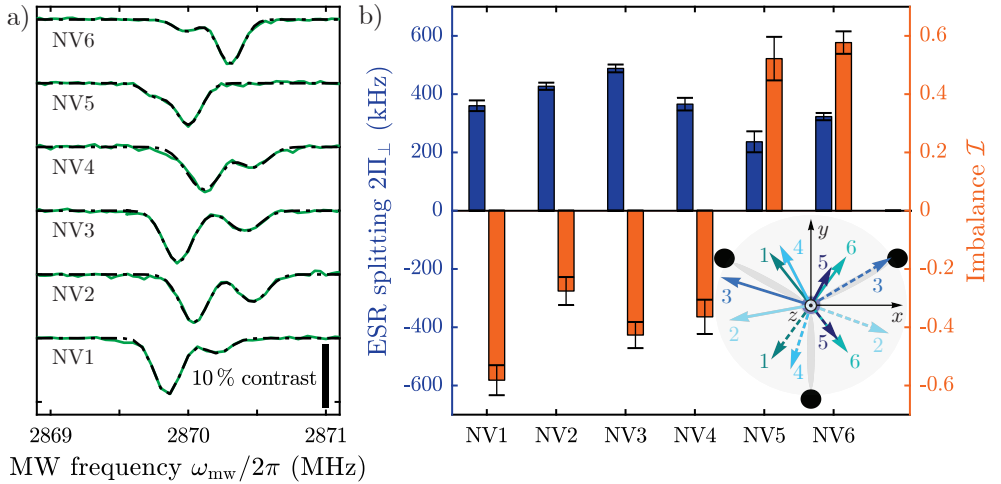

Figure 6.4.: Characterization of the effective field environment of selected single NV centers. a) High-resolution ESR spectra for $B_\parallel = 0\,\mathrm{G}$ for several single NV centers showing a splitting of the $m_I = 0$ levels and imbalances of the corresponding transitions. b) Summary of the extracted splittings $2\Pi_\perp$ and transition imbalances $\mathcal{I}$ from panel a) and schematic illustration of the transverse effective field component for each NV (numbers refer to NV labels). Each dataset is consistent with two possible values for φ_Π and both possible effective field orientations are shown for each NV.
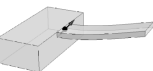
different symmetry behavior. Once the polarization angle for a given NV is known, geometric considerations allow us to infer the corresponding angles for the other NV orientations. Moreover, we point out that in order to determine φ_Π without ambiguity, one could e.g. conduct a second set of measurements with a different MW polarization angle φ_mw.

6.4. Hyperfine interaction with a nearby nuclear spin

Besides the well-understood ESR spectra of NV1–NV6 from Fig. 6.4, which show an effective field induced splitting of the $m_I = 0$ states into two sublevels at zero magnetic field, we also studied a single NV ('NV7'), whose spectrum shows in total six transitions in the high-resolution ESR spectrum at $\boldsymbol{B} = 0$. Specifically, besides a splitting of the $m_I = 0$ transitions, all other transitions show a splitting into a doublet as well. The splitting of all the hyperfine levels into two sublevels persists independent of an applied parallel magnetic field (see Fig. 6.5a). This observation indicates a coupling between the NV spin and a nuclear spin ($I^{(C)} = 1/2$) of a ^{13}C isotope, which occupies a nearby site in the diamond lattice (see Sec. 2.2.4).

According to Eq. (2.11), the ^{13}C hyperfine induced splittings of the $|m_s, m_I\rangle$ states with $m_s = \pm 1$ are in the secular approximation given by

$$\Delta^{(C)} = \left[A_{zx}^2 + A_{zy}^2 + (A_{zz} - \gamma_\mathrm{C} B_\parallel)^2 \right]^{1/2} + \gamma_\mathrm{C} B_\parallel \; . \tag{6.10}$$

In the regime of Fig. 6.5a, we find $\gamma_\mathrm{C} B_\parallel \lesssim 1\,\mathrm{kHz}$ to be a negligible factor, while the observed hyperfine splitting of the sublevels is $\approx 700\,\mathrm{kHz}$. Consequently, we define the ^{13}C hyperfine coupling strength $A_\mathrm{HF}^{(C)} = (A_{zx}^2 + A_{zy}^2 + A_{zz}^2)^{1/2}$, as introduced in Eq. (2.12). We determine $A_\mathrm{HF}^{(C)}$ by a Gaussian fit of the spectrum at $B_\parallel = 0\,\mathrm{G}$ in Fig. 6.5a (see inset). By evaluating the splitting of the $m_I = \pm 1$ transitions (outer transition pairs ① and ③) we find $A_\mathrm{HF}^{(C)} = 707(14)\,\mathrm{kHz}$. The extracted hyperfine coupling corresponds to a ^{13}C isotope that sits on a lattice site labeled by 'M' [89]. Unfortunately, for this group is no correspondence with a specific site in the diamond lattice available, as the accuracy of underlying *ab initio* calculation is hardly better than a few hundred kHz.

Besides the effect of the nuclear spin coupling, the spectrum also reveals the signatures of the effective field, emphasized by the fact that the contrast of the ESR transitions is not symmetric upon inflection with respect to $\omega_\mathrm{mw}/2\pi \approx 2870\,\mathrm{MHz}$. As established in Sec. 6.1, the effective field parameters can be related to the splitting and imbalance of the $m_I = 0$ transitions (inner transition pair ②) at $B_\parallel = 0\,\mathrm{G}$. In contrast to our considerations in Sec. 6.1, the splitting of these states is now given by

$$\Delta_\Pi^{(C)} = \left[\left(A_\mathrm{HF}^{(C)} \right)^2 + (2\Pi_\perp)^2 \right]^{1/2} , \tag{6.11}$$

whereas the transition imbalance from Eq. (6.7) is modified to

$$\mathcal{I}^{(C)} = -\frac{2\Pi_\perp}{\sqrt{\left(A_\mathrm{HF}^{(C)} \right)^2 + (2\Pi_\perp)^2}} \cos(2\varphi_\mathrm{mw} + \varphi_\Pi) \; . \tag{6.12}$$

We note that the prefactor in Eq. (6.12) arises from the fact that $B_\parallel = 0\,\mathrm{G}$ does not correspond to a magnetic field value where the strain-induced coupling between two hyperfine states is maximal, as the ^{13}C hyperfine splitting is present. This ultimately reduces the observed transition imbalance. Using the parameters extracted from the Gaussian fit of the inner transition pair ②, $\Delta_\Pi^{(C)} = 813(15)\,\mathrm{kHz}$ and $\mathcal{I}^{(C)} = -26(4)\,\%$, we obtain the effective field parameters $\Pi_\perp = 200(28)\,\mathrm{kHz}$ and $\varphi_\Pi = 126(10)°$ or $\varphi_\Pi = 243(10)°$ (resulting from the symmetry with respect to $2\varphi_\mathrm{mw}$).

These parameters allow us to simulate the spectrum from Fig. 6.5a, as shown in Fig. 6.5b. The underlying calculation is based on Hamiltonian (6.1) including an hyperfine interaction term $\hat{\mathcal{H}}_\mathrm{HF}^{(C)}/h = A_\mathrm{HF}^{(C)}\hat{S}_z\hat{I}_z^{(C)}$ (compare to Eq. (2.10)). A comparison of the simulation with the experimental data yields excellent agreement. Note that the spectrum exhibits a contrast asymmetry with respect to $\omega_\mathrm{mw}/2\pi \approx 2870\,\mathrm{MHz}$ that is more pronounced than in Fig. 6.2a, since in the present case the effective field amplitude is larger.
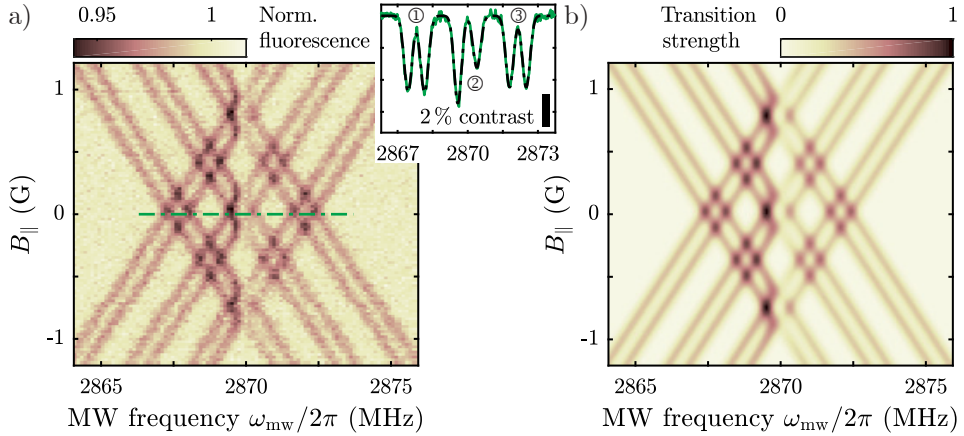

Figure 6.5.: Hyperfine interaction with a nearby ^{13}C nuclear spin. a) The spectrum of NV7 while varying the parallel magnetic field $B_\parallel$ shows a similar behavior compared to NV1 in Fig. 6.2a, but offers a splitting of each hyperfine transition into two lines. This splitting is characteristic for a coupling of the NV spin to a nearby ^{13}C nuclear spin. Still, the effective field induces a splitting of lines crossing around $\omega_\mathrm{mw}/2\pi \approx 2870\,\mathrm{MHz}$ and introduces a contrast imbalance between higher and lower frequency transitions. By fitting the spectrum at $B_\parallel = 0\,\mathrm{G}$ (inset) we determine the ^{13}C hyperfine coupling strength $A_\mathrm{HF}^{(C)} = 707(14)\,\mathrm{kHz}$ from the outer transition pairs ① and ③ as well as the effective field parameters $\Pi_\perp = 200(28)\,\mathrm{kHz}$ and $\varphi_\Pi = 126(10)°$ (or $\varphi_\Pi = 243(10)°$) from the inner transition pair ②. b) We use the extracted parameters to calculate the spectrum based on the Hamiltonians (2.10) and (6.1). The resulting simulation agrees excellently with the measurement.
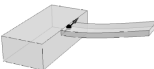
6.5. Determination of the MW polarization angle

We finalize our spectroscopy study of the effective field by establishing a method to experimentally determine the polarization angle φ_{mw} of the MW field that is used to drive the spin transitions (see Fig. 6.1a). To do so, we exploit the response of the hyperfine spin transitions to a purely transverse magnetic field. Because a transverse magnetic field couples $|-1\rangle$ and $|+1\rangle$ states in second order, the transition frequencies show a quadratic dependence on the field (see Fig. 2.3a and Fig. 6.2d for data on NV1). Similarly to Fig. 6.2a, the spectrum shows in total six transitions. However, the corresponding states of the two outer transitions are degenerate, resulting in four resolvable transitions with the two outer ones exhibit double the contrast relative of the inner ones. The inner transitions approach the dominant outer transitions for large fields, indicating a tilting of the spin quantization axis towards the transverse field axis, which defines the new eigenstates of the system, $|\tilde{0}\rangle$, $|\tilde{-}\rangle$, and $|\tilde{+}\rangle$.

At $B_\perp = 32\,\mathrm{G}$ (the largest achievable transverse magnetic field amplitude in our setup) we study the influence of the azimuthal angle of the transverse field φ_B while setting $B_\parallel = 0\,\mathrm{G}$ (within our experimental resolution). In this situation, we change φ_B and perform pulsed ESR measurements on the hyperfine transitions (see Fig. 6.6a). We observe clear oscillations of the contrasts of the four transitions as a function of φ_B. Specifically, the contrasts of the two lower frequency transitions at $\omega_{\mathrm{mw}}/2\pi \approx$ 2871 MHz and $\omega_{\mathrm{mw}}/2\pi \approx 2872.5\,\mathrm{MHz}$ (labeled with ① and ②) oscillate in phase, as do the contrasts of the two higher frequency transitions at $\omega_{\mathrm{mw}}/2\pi \approx 2875.5\,\mathrm{MHz}$ and $\omega_{\mathrm{mw}}/2\pi \approx 2877\,\mathrm{MHz}$ (labeled with ③ and ④). However, the oscillations of the contrasts of these two pairs of transitions with φ_B are not in phase and exhibit a phase shift $\approx \pi/2$. In other words the lower frequency transitions ① and ② have highest contrast when the higher frequency transitions ③ and ④ have low contrast, and vice versa.

Using a similar theoretical model as introduced in Sec. 6.1.2, we calculate the transition strengths based on Hamiltonian (6.1). As we consider the regime $\gamma_{\mathrm{NV}}B_\perp \gg \Pi_\perp, |A_{\mathrm{HF}}|$, the effective field and hyperfine coupling can be neglected in the first order. The eigenstates of the Hamiltonian thus read $|\tilde{0}\rangle \approx |0\rangle$, $|\tilde{-}\rangle$, and $|\tilde{+}\rangle$, where $|\tilde{-}\rangle$ and $|\tilde{+}\rangle$ are mixed states of $|-1\rangle$ and $|+1\rangle$ due to the presence of the transverse magnetic field. In analogy to our results in Sec. 6.1.2, we find the transition strengths

$$
\begin{aligned}
\mathcal{A}_{0,\pm} \propto \Omega_{0,\pm}^2 &= \frac{1}{\hbar^2} \left| \boldsymbol{B}^{\mathrm{mw}} \cdot \boldsymbol{\mu}_{0,\pm} \right|^2 \\
&\approx \frac{1}{\hbar^2} \frac{(2\mu_B B_\perp^{\mathrm{mw}})^2}{2} \left[1 \pm \cos(2\varphi_B - 2\varphi_{\mathrm{mw}}) \right] ,
\end{aligned}
\tag{6.13}
$$

where we have used the magnetic dipole matrix elements $\boldsymbol{\mu}_{0,\pm} = -2\mu_B \langle \tilde{\pm} | \hat{\boldsymbol{S}} | 0 \rangle$. According to Eq. (6.13), rotating the transverse magnetic field component by changing φ_B leads to oscillations in the transition strengths of the involved transitions, i.e. in their experimentally observed contrasts. The π-periodicity of these oscillations is induced by the periodic change of the overlap of the fixed MW polarization and the varying orientation of the dipole moments and is mirrored by the alternating ESR contrast in the experiment. The phase offset of these oscillations is related to the MW polarization angle φ_{mw}. By analyzing the oscillations in the data shown in Fig. 6.6a we find $\varphi_{\mathrm{mw}} = 89.2(8)°$ in the reference frame of NV1.
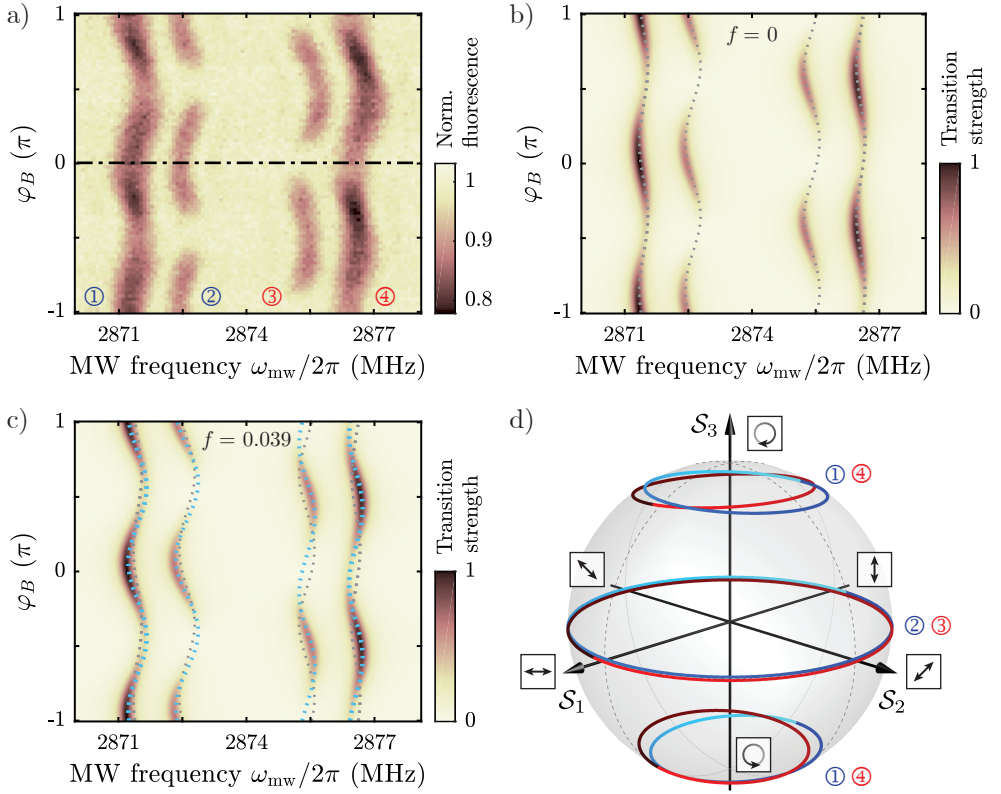
Figure 6.6.: Determination of the MW polarization angle φ_{mw} by rotating the transverse magnetic field component around the quantization axis of NV1. a) Experimental data for $B_\perp = 32\,\mathrm{G}$ and $B_\parallel = 0\,\mathrm{G}$. The transition strengths of all states oscillate. Additionally, the transition frequencies show periodic 'wiggles'. b) Calculated spectrum based on Hamiltonian (6.1) considering the intrinsic strain in the diamond lattice while the magnetic field rotation is assumed to be perfectly circular (flattening $f = 0$). The calculated transition frequencies are highlighted (gray dots). The transitions at higher frequency show 'wiggles', which are out of phase compared to the measurement. c) By including an imperfect, elliptic magnetic field rotation with a flattening $f = 0.039$ the simulation reproduces the experimental data. This allows us to determine the MW polarization angle in the transverse plane. In the reference frame of NV1, we find $\varphi_{\mathrm{mw}} = 89.2(8)°$ with respect to the x-axis. To quantify the relative contributions of intrinsic strain and the elliptic magnetic field rotation, we show the calculated transition frequencies (light blue dots) besides the ones extracted from the simulation in panel b) (gray dots). d) Visualization of the polarization response of each of the six transitions on the Poincaré sphere for $0 \le \varphi_B < \pi$ (from dark to light coloring). Due to symmetry the behavior for $\pi \le \varphi_B < 2\pi$ is identical. While the transitions ② and ③ have a purely linearly polarized response, the transitions ① and ④ have an elliptic polarization response as their mutual coupling is affected by the hyperfine interaction. Note that the transitions with lower frequency (① and ②) are phase-shifted by $\Delta\varphi_B = \pi/2$ with respect to the transitions with higher frequency (③ and ④).
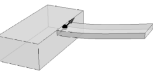
Eq. (6.13) reproduces the experimentally observed oscillations in the transition contrast and offers some intuition for interpreting the data. According to the presented model, however, the frequencies of the observed transitions should not be affected by varying φ_B. One reason for this discrepancy is that in Eq. (6.13) we have neglected the influence of the effective field. Including the effective field in the theory, however, does no longer allow for an analytical treatment. We, therefore, numerically model the impact of the effective field on the ESR spectrum by simulating our experiment based on Hamiltonian (6.1), using the parameters extracted from Fig. 6.2b. As shown in Fig. 6.6b, including the intrinsic strain in the simulation gives rise to 'wiggles' of the transition frequencies (gray dots). While the calculated lower frequency transitions ① and ② reproduce the wiggling observed in the measurement, the 'wiggles' of the calculated higher frequency transitions ③ and ④ are phase-shifted by $\pi/2$ compared to the experimental data. This phase shift is attributed to two effects, an imperfect alignment of the magnetic field axis and the influence of an imperfect, elliptical rotation of the transverse magnetic field amplitude. The imperfect field alignment induces a varying, non-zero parallel magnetic field component. As we discuss in App. A.1.1, this is, however, negligible in the present case. To take account of the second effect, we consider a realistic ellipticity of the transverse magnetic field rotation characterized by a flattening[2] of $f = 0.039$. Thereby we are able to reproduce both the wiggling of the transition frequencies and the asymmetric shift of the transition contrast (see Fig. 6.6c). To characterize the relative contributions of the effective field and the imperfect magnetic field rotation, Fig. 6.6c further shows the simulated transition frequencies for both situations. This allows us to compare the calculated transition frequencies including both aspects (blue dots) with the case where only the known effective field is considered, while the magnetic field rotation is assumed to be perfectly circular (gray dotted, see also Fig. 6.6b). From this comparison it becomes apparent that only the pair of the higher frequency transitions ③ and ④ is significantly affected by the ellipticity of the magnetic field, as the states involved in these transitions are more susceptible to transverse magnetic fields than the ones pertaining to the low-frequency pair of transitions ① and ② (see Fig. 2.3a). Moreover, the amplitude of the wiggles induced by the ellipticity is very similar to the amplitude of the wiggles induced by the effective field, thus both effects are of comparable order. Nevertheless, we conclude from our simulations that this experimental imperfection does not affect any of the other findings we report on here.

Finally, Fig. 6.6d illustrates the polarization response for each of the transitions as a function of φ_B on the Poincaré sphere following the analysis outlined in Sec. 2.3.1. The trajectories of the transitions ② and ③ evolve along the equator, implying a linearly polarized response with a rotating polarization axis, as expected. Thus, the overlap of the magnetic dipole matrix elements and the MW driving field changes periodically with φ_B from zero to its maximum. This corresponds to the experimental observations, where both transitions periodically lose their contrast completely. On the contrary, the transitions ① and ④ comprise elliptic polarization responses to both circulation directions. This is a direct consequence of the interplay between the magnetic field mixing and the hyperfine interaction between the involved states. Therefore, the magnetic dipole matrix element and the MW driving field have always

---

[2]The flattening f characterizes the aspect ratio of the ellipse in terms of the semi-major and semi-minor axes a and b, respectively. It is defined as $f = 1 - b/a$.

a non-zero overlap, resulting in an observable contrast independent of φ_B. To visualize the evolution of the trajectories, we encoded the variation of φ_B in their color gradients, starting at $\varphi_B = 0$ (dark blue and red) and evolving to $\varphi_B = \pi$ (light blue and red). Due to the periodicity of Eq. (6.13) the response of the transitions for $\pi \leq \varphi_B < 2\pi$ is the same. The color-coding makes the phase shift between the lower frequency (① and ②) and higher frequency (③ and ④) transitions visible. Both pairs of transitions rotate symmetrically with respect to the $\mathcal{S}_3$-axis, which is consistent with the $\pi/2$ phase shift along the φ_B-axis observed in the experimental data. The offset of the starting points for $\varphi_B = 0$ with respect to the $\mathcal{S}_1$-axis is directly linked to the azimuthal angle φ_Π of the effective field $\mathbf{\Pi}$. Hence, modeling the polarization response of the transitions on the Poincaré sphere gives an illustrative intuition for the observed contrast oscillations.

6.6. Conclusion and outlook

In summary, we presented high-resolution ESR spectroscopy studies on single NV defect centers in diamond to characterize their local effective field environment. Our approach is based on a detailed examination of the NV spin's allowed magnetic dipole transitions, which are affected by the interaction of the MW probing field and the intrinsic effective field. In our case of single NVs in high purity diamonds, we find that strain is the major contribution to the effective field. These findings contrast previous studies on NV ensembles in more strongly doped diamonds, where the electric field was the dominant over strain [115]. We also showed that our results apply to more complex NV environments, e.g. induced by the coupling to nearby nuclear spins. In addition, we established a new method for performing single spin-based, linear polarization analysis of MW fields using low-power ESR in well-controlled bias fields. Thus, our method offers a characterization tool for both the intrinsic effective field and the MW manipulation field.

However, there remain unexplained experimental observations that require further investigations. In this context, Fig. 6.7 shows the spectrum of NV8 in a parallel magnetic field. Compared to the spectrum of NV1 in Fig. 6.2a, NV8 offers an additional splitting at the avoided crossings of nuclear spin states with the same m_I. For instance, at $B_\parallel = 0\,\mathrm{G}$ there are four transitions associated with $m_I = 0$, whereas the $m_I = \pm 1$ transitions are not affected at all at this magnetic field strength. The same behavior with interchanged roles is observed at $B_\parallel = \pm |A_{\mathrm{HF}}|/\gamma_{\mathrm{NV}}$ for the other nuclear spin projections. This spectrum cannot be explained by a coupling to a $^{13}\mathrm{C}$ nuclear spin. The hyperfine interaction given by Eq. (2.10) is linear in $\hat{\mathbf{S}}$ and, therefore, does not couple $|-1\rangle$ and $|+1\rangle$ states, as this requires terms quadratic in $\hat{\mathbf{S}}$. This argument also holds if the secular approximation is not considered. Instead, the additional splitting of NV8 might be caused by an effective field environment, in which strain or the electric field fluctuates between two distinct values. When these fluctuations happen on a timescale faster than our data acquisition, we effectively measure a time average, which shows both possible values of the effective field splitting. To verify this approach to an explanation we suggest a time-resolved set of measurements. Another possibility is that two $^{13}\mathrm{C}$ nuclear spins are located at particular lattice sites
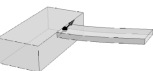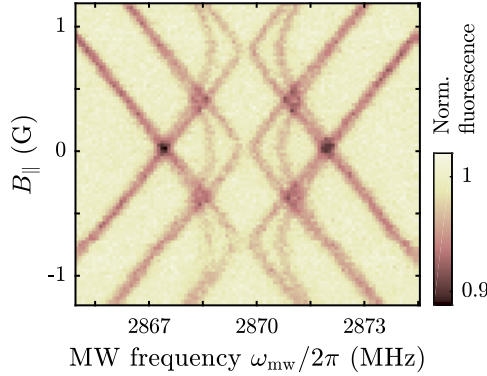
Figure 6.7.: Spectrum of NV8 while varying the axial magnetic field $B_\parallel$. Besides the familiar linear Zeeman shift of the transitions, the spectrum exhibits a splitting into four lines at the avoided crossings of two spin transitions with equal nuclear spin projection m_I. The origin of this additional splitting cannot be explained by a hyperfine interaction with a single nearby ^{13}C nuclear spin, but might be a signature of two coupled ^{13}C nuclear spins or a fluctuating effective field environment, which can attain only two distinct values. As of now, the spectrum is not explained and requires further investigations.

in the vicinity of NV8, whose mutual couplings with the NV affect each other and give rise to the observed behavior. Yet, the complete description of the spectrum is an open question.

Nevertheless, the fact that our conclusions on the nature of the local effective field of the single NV spins differ from recent studies on NV ensembles [115], highlights the importance of characterizing such fields in a quantitative and effective way. Such precise characterization is then particularly relevant for NV-based quantum sensing applications where low-field operation is of primary importance. Examples for these include the application of the three-level dressed states extensively discussed within the scope of this work [148, 183], nanoscale magnetic imaging of magnetically sensitive samples [203], or NV-based low-field techniques like zero and ultra-low field nuclear magnetic resonance [204]. The novel MW polarization analysis we demonstrated could find applications in NV-based MW imaging [205, 206], which until now was only demonstrated for sensing of circularly polarized MWs [207]. Our results extend these capabilities and the existing toolset of NV-based quantum sensing modalities. For instance, it would in principle allow for determining the full polarization state of MW fields with nanoscale resolutions, which has relevance in MW electronics [208] or spintronics devices [209].

7. Summary and outlook

The protection of electron spins from environmentally induced decoherence is a fundamental challenge in quantum science. Within the scope of this thesis, we reported on the experimental implementation and extensive analysis of a novel continuous decoupling scheme to address this impediment. To that end, we dressed the ground state spin levels of an individual NV spin in diamond with resonant and continuous driving fields in a closed interaction contour, thereby establishing a new resource for coherence protection from magnetic fluctuations. The detailed characterization we provided constitutes a major step towards the future applications of the dressed states in quantum technologies.

7.1. Summary

We started this thesis with a brief introduction to the foundations of the NV center in Chap. 2, including the general description of the spin ground state by its Hamiltonian and a discussion of NV's response to static external fields. We also explained the two employed mechanisms for coherent spin control, MW magnetic fields and time-varying strain fields. By combining both manipulation techniques, we were able to realize a closed-contour interaction scheme in the NV's three-level ground state, which also constitutes an appealing continuous dynamical decoupling scheme for other few-level quantum systems.

The closed-contour dressed states that emerge from such driving were at the heart of this thesis. In Chap. 3 we presented a comprehensive study of the system's dynamics as a function of the global phase, i.e. the relative phase of the three driving fields. Besides demonstrating a non-reciprocal character of the dynamics, we found that the dressed states under study exhibit robust coherence properties even in the presence of magnetic field fluctuations, i.e. they are efficiently decoupled from their spin-bath environment. This coherence protection is based on the unique nature of the dressed states we realized, which suppresses their response to magnetic noise. Our measurements thereby indicated coherence times up to nearly two orders of magnitude longer compared to the undriven NV spin.

While our initial results were obtained by performing measurements on a superposition of dressed states, we addressed the initialization of a pre-defined, single dressed state in Chap. 4. To that end, we employed state transfer protocols based on the adiabatic theorem and recently developed STA protocols to realize high-fidelity and reversible initialization of a particular dressed state. By comparing both approaches we achieved a more than twofold speedup for the STA protocol with state transfer fidelities $\approx 99\,\%$. This performance is the direct result of the fast, high-efficiency initialization with STA protocols and of the remarkable coherence protection of the closed-contour dressed states.
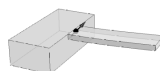
By establishing the initialization and remapping processes, we provided a basis for the coherent manipulation and control of the dressed states in their own manifold. This allowed us to accurately characterize the dressed states' properties. We thereby gained direct access to the dressed state subspace that offers the best coherence protection and verified that the corresponding coherence time is improved by nearly two orders of magnitude over the undressed case. Our results constitute an important step towards further studies of the remaining, unknown dressed state decoherence processes, which could be explored by employing noise spectroscopy and dynamical decoupling directly in the dressed state basis. In addition to this, the closed-contour decoupling mechanism will have impact on any quantum technology where pulsed decoupling protocols cannot be employed.

Finally, we characterized the local effective field environment of single NV centers by high-resolution ESR spectroscopy in Chap. 6. Based on a theoretical model of the magnetic dipole transitions and the MW driving field, we extracted both the strength and the direction of the transverse component of the effective field. A thorough examination of several single NVs revealed that in our case of a high purity diamond, strain is the major contribution to the effective field. Moreover, by applying external magnetic fields and exploiting the magnetic dipole selection rules we directly probed the MW polarization at the NV position. Thus, our method offers a characterization tool for both the intrinsic effective field and the MW manipulation field.

7.2. Outlook

In this outlook, we motivate further routes that can be taken with our dressed states under closed-contour interaction and discuss general proposals that are within reach with our experimental methods.

Our results yielded a nearly 100-fold improvement of coherence times for the dressed states compared to the undriven NV system. However, the enhancement was limited by temperature drifts and driving field noise. To push the coherence of the dressed states to the T_1 limit, we suggest stabilizing the environmental conditions by working with active temperature stabilization, in vacuum and/or in a cryostat, and to use driving fields with less amplitude noise. Overcoming the limitations imposed by these fluctuations and thus extending the coherence times represents a key step towards the construction of a quantum memory [188, 189] or the establishing of the dressed states as a resource for sensing of gigahertz fields on the nanoscale [47, 156]. In such sensing schemes, the tunability and coherence protection of our system offer interesting avenues for enhanced sensitivities and phase-tuning of the sensing frequencies.

The phase dependence of the closed-contour system further gives rise to phase-induced transparency, in which the phase of the MW driving fields tunes the absorption of the mechanical driving field [144]. In optomechanics experiments with NV centers, this may allow a phase-controlled switch to rapidly gate spin-phonon interactions [134]. Additionally, changing the phases of the applied fields offers the possibility to direct the population dynamics. By changing the global phase the populations, and thereby the absorption properties of the system are affected. This method could be used to create effective MW modulators [49]. In combination with the non-reciprocal

character of the dynamics for certain phase values, elements such as MW circulators or directional amplifiers could be envisioned [157].

Although demonstrated on a single NV spin here, we believe that our closed-contour driving scheme offers an attractive technique to extend coherence times in all few-level systems that suffer from magnetic noise, such as solid-state and atomic systems with suitable optical and MW transitions, e.g. ion-doped crystals, quantum dots, and trapped ions. In this context, the combination of the closed-contour decoupling with a robust sequence of phased pulses provides an innovative way to protect the system not only from environmental noise but also from driving field noise [48]. Such a mixed dynamical decoupling approach might lead to an even larger increase in the coherence time, which is of great significance for sensing protocols as it allows for enhanced sensitivities.

Based on our findings, we also believe that our system will serve as a powerful resource for quantum information processing. To that end, the construction of fault-tolerant quantum operations that are protected against noise and control errors must be examined [42]. In particular, we advocate the experimental implementation of non-Abelian geometric quantum gates. These build on the concept of geometric phases, which can be induced within the subspace of two degenerate eigenstates in a triangular three-level system like ours [159, 210]. In such a degenerate subspace a universal set of quantum gates can be implemented by using adiabatic non-Abelian geometric phases. In analogy to our state transfer protocols, these adiabatic geometric quantum gates can be accelerated in terms of STA methods. The combination of the intrinsic geometric characteristic and STA would offer fast quantum operations that are robust against noise and certain control errors and that achieve high operation fidelity [159].

Another interesting route to be pursued in the future is the exploration of the coherent coupling between the closed-contour system and nearby nuclear spins [158]. For example, instead of addressing all three NV spin transitions resonantly, we suggest driving one transition with a detuning that is resonant with the Zeeman splitting of the nuclear spins. Under the condition that the driving fields' amplitudes are much larger than the detuning, it will still be possible to define a global phase value for at least one circulation period of the population in the three-level system. Depending on the global phase the nuclear spin transitions is then only be addressed in the direction that is determined by the dynamics of the interaction contour. The resulting controlled manipulation of the nuclear spin transitions will allow for polarization of the nuclear spins and ultimately for cooling of nuclear spin ensembles in diamond. Such coupling would also offer new perspectives with respect to the detection and polarization of spins external to the diamond.

Quantum synchronization is an additional highly topical research area, in which our three-level system serves as an ideal experimental testbed. Theoretical studies revealed that three-level systems are the smallest possible systems that are able to show synchronization to an external signal, i.e. that offer stable limit cycle oscillations in phase space [211]. Besides individual control of the external driving fields (here e.g. two weak MW tones or all three driving fields to address all ground state transitions) that we provide in our system, an experimental implementation also requires engineering incoherent dissipation of the $|-1\rangle$ and $|+1\rangle$ states to $|0\rangle$ at particular rates. In the case of asymmetric decay rates, it is predicted that the system is able
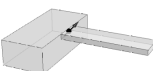
to synchronize to, for example, the difference phase of the applied weak MW driving fields [212]. Such dissipation processes may be realized by including optical transitions to the excited state and making use of the intersystem crossing or by applying additional incoherent fields to address the $|0\rangle \leftrightarrow |\pm 1\rangle$ transitions.

Finally, we point out some more far-reaching perspectives for the hybrid spin-mechanical system we used in this thesis. Based on the employed spin-strain coupling mechanism, the next steps could aim for the implementation of quantum coherent interactions between the spin and the mechanical oscillator. Specifically, collective strain-coupling of spin ensembles to nanomechanical oscillators can in principle be exploited to generate spin-squeezing, i.e. entanglement [213]. Such entangled spins form an attractive resource for quantum metrology, but methods for entanglement generation are currently too inefficient to implement practical sensing schemes. Moreover, coherent spin-phonon interactions may allow for the possibility of using an NV spin to probe the position of the mechanical resonator with uncertainty limited by the Heisenberg principle or conversely of making a quantum nondemolition readout of the NV spin state through a measurement of the cantilever displacement. Using spin-mechanical backaction further allows for the study of spin-induced cooling of the mechanical resonator to the quantum ground state by driving Raman like transitions on embedded spins in the resolved sideband regime [214–216]. This would enable fundamental studies of quantum mechanics in macroscopic objects and may be used to generate non-classical states of the mechanical resonator, such as Schrödringer cat states. Alternatively, phonons can also be employed to mediate quantum-state transfer and generate effective interactions between separate NV spins [217]. Another exciting avenue consists of integrating our hybrid spin-optomechanical system into optical cavities to realize a coherent, tripartite spin-phonon-photon system. The realization of all these challenging prospects can, however, only be speculated with our current experimental conditions [114]. An actual implementation would require several improvements, e.g. going to cryogenic temperatures, limiting surface-induced spin decoherence and spectral diffusion of the NV center, making use of new types of mechanical resonators such as diamond optomechanical crystals [192–194] or surface acoustic wave cavities [195], and employing the stronger excited state spin-strain [216] or orbital-strain coupling [218]. Thus, in the future each of these challenges must be mastered experimentally in their own right.

A. Appendix

A.1. Details on the experimental setup

In this section, we discuss two essential components of the employed experimental setup, the static magnetic field control and the MW field generation. For a detailed description of the other parts of the setup, e.g. the confocal microscope, we refer the reader to [114].

### A.1.1. Alignment and control of the magnetic field

To apply and control external magnetic fields, our experimental setup comprises three pairs of coils arranged in a Helmholtz-like setup, i.e. the spatial separation between corresponding coils matches their diameter (X,Y-pairs) or their radius (Z-pair) [114, 116]. Each pair is driven by a constant-current source (Agilent E3644A) enabling software-based three-dimensional magnetic field control. The calibration of the magnetic field was performed with a Teslameter (Projekt Elektronic, FM 302 with transverse probe AS-NTM).

In order to align the magnetic field to a desired NV orientation, we use the procedure described in detail in [219]. The method relies on the controlled spatial rotation of the magnetic field and the resulting effect on the NV's ESR frequency. Comparing the experimental data from Fig. 6.6a with corresponding simulations allows us to estimate two important parameters: First, the simulations show that the achieved alignment uncertainty is within $< 0.2°$ from a desired NV direction, otherwise the outer two degenerate states would be split. Second, we estimate that the ellipticity of the magnetic field rotation mentioned in Sec. 6.5 is characterized by a flattening $f < 0.04$, otherwise the observed wiggles in Fig. 6.6a would be larger. The fact that we observe such an ellipticity may be attributed to uncertainty in the calibration of the coils.

Both facts, however, only appear when a large perpendicular magnetic field is applied and rotated. Thus, within this work it is only relevant for the data of Fig. 6.6, where $B_\perp = 32\,\text{G}$. For all the other measurements and in particular the ones we use to extract the effective field parameters in Sec. 6.2.1 and Sec. 6.3, the applied magnetic fields are static and only used to cancel external magnetic fields, e.g. earth magnetic field. The extracted effective field parameters are, therefore, not affected.

A.1.2. Creation of arbitrary MW field pulse shapes with phase-locking

To generate the driving fields for our experiments we use the setup as shown schematically in Fig. A.1 and presented in [183]. The envelopes of the MW field amplitudes used for driving the $|0\rangle \leftrightarrow |\pm1\rangle$ transitions are created through an I/Q frequency
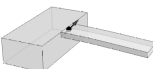
modulation technique. Specifically, a carrier signal at frequency ω_c is modulated with appropriate modulation signals I and Q. Both modulation signals are composed of two individually generated pairs of (I,Q) signals at the frequencies $\omega_{\text{IQ},1}$ for (I_1,Q_1) and $\omega_{\text{IQ},2}$ for (I_2,Q_2), respectively. Within each (I,Q) pair, the amplitudes are constant and equal, although the amplitudes of the pair (I_1,Q_1) differ in general from those of (I_2,Q_2). However, the relative phases of the signals within a pair differ from each other, i.e. I_1 (I_2) is phase shifted with respect to Q_1 (Q_2). This phase shift, which is $\phi_{\text{IQ},1} = -\pi/2$ and $\phi_{\text{IQ},2} = \pi/2$, allows for the suppression of one modulation sideband for each (I,Q) signal pair. Thus, after combining both modulation pairs, the resulting modulated frequency spectrum contains two remaining frequency components, namely $\omega_1 = \omega_c - \omega_{\text{IQ},1}$ and $\omega_2 = \omega_c + \omega_{\text{IQ},2}$. To arbitrarily shape the amplitudes of both MW driving fields and thereby generate the desired ramps for state initialization, we modify each (I,Q) pair's amplitude with well-defined envelope functions using an arbitrary waveform generator (AWG) and a four-quadrant voltage multiplier (MP).
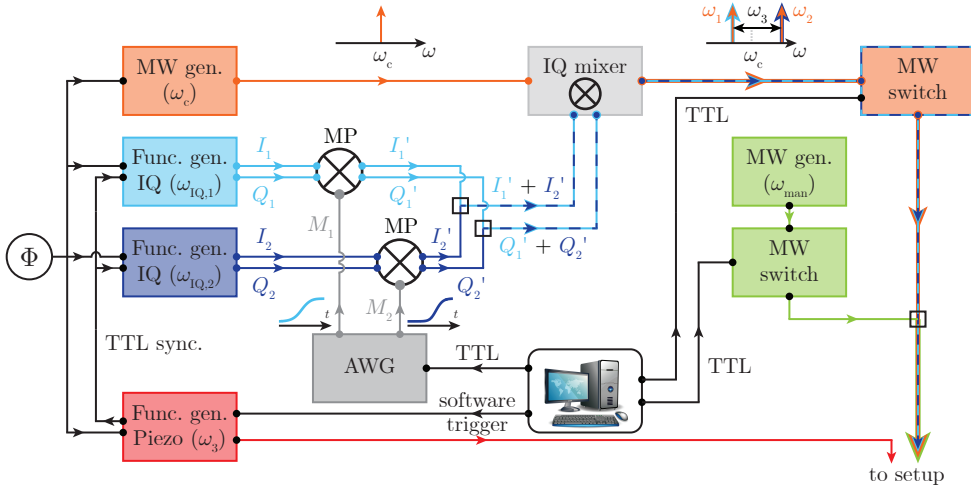

Figure A.1.: Setup used for arbitrary waveform control of the MW driving fields. The two MW driving tones with frequencies $\omega_1 = \omega_c - \omega_{\text{IQ},1}$ and $\omega_2 = \omega_c + \omega_{\text{IQ},2}$ are created via I/Q frequency modulation of a carrier signal with frequency ω_c. Therefore, two pairs of (I,Q) signals with frequencies $\omega_{\text{IQ},1}/2\pi = 2.4\,\text{MHz}$ and $\omega_{\text{IQ},2} = \omega_3 - \omega_{\text{IQ},1}$ are combined. Each pair exhibits an appropriate phase shift of the I and Q signal to suppress one modulation sideband. Additionally, the (I,Q) pairs' amplitudes are modified by multiplication with the signals (M_1,M_2) of an AWG using a four-quadrant MP. The mechanical driving field is created by a function generator actuating the Piezo element near-resonant with frequency $\omega_3/2\pi$. We establish phase-locking of the three driving fields to a global phase Φ by pulsed output synchronization and locking of the MW, I/Q and Piezo function generators to the same 10 MHz reference signal. An additional MW probe field (ω_{man}) is added to the MW driving fields for manipulation of the dressed spin states.

To ensure phase-locking between the three driving fields, the MW source (Standford Research Systems, SG384) and the function generators supplying the Piezo actuation and the (I,Q) signals (Keysight, 33522B) are connected to the same 10 MHz reference signal. To set the global phase to a well-defined value Φ, the output of the Piezo function generator is triggered via a software command. After receiving a trigger pulse, a subsequent trigger is forwarded to the I/Q function generators to start their outputs.

The (I,Q) signals' envelopes are synthesized by an AWG (Tektronix, AWG 5014C), whose signals modifies the (I,Q) pairs' amplitudes via four-quadrant multiplication (Analog Devices, AD734). After that, both (I,Q) pairs are combined (MiniCircuits, ZFSC-2-6+). For I/Q modulation we then use the in-built I/Q modulator of our MW source.

The additional MW field used for manipulation in the dressed state manifold (Rhode & Schwarz, SMB 100A) is added to the MW driving fields via a MW combiner (MiniCircuits, ZFRSC-42-S+). All MW pulses are controlled via digital pulses from a fast pulse generator card (SpinCore, PBESR-PRO-500), which triggers the AWG and the MW switches (MiniCircuits, ZASWA-2-50DR+).

Creating the MW pulses in the described way is limited by the vertical resolution of the four-quadrant MP, which exhibits a noise spectral density of $1\,\mu\text{V}/\sqrt{\text{Hz}}$. Hence, the estimated noise amplitude within the 10 MHz bandwidth of the MP is $3.2\,\text{mV}_{\text{rms}}$. The finite jumps at the beginning and at the end of our driving field ramps are determined by the parameter ε (see Sec. 4.2) scaled with the maximum output of the AWG, given by 4.5 V. As additional noise is added within the I/Q modulation, choosing $\varepsilon = 10^{-3}$ yields a discontinuity step that is comparable to the noise amplitude of our MW signals.

A.2. State transfer dynamics

In Chap. 4 and in [183], our experimental observations and theoretical calculations of the state transfer process are based on reading out the population

$$P_{|0\rangle}(t) = |\langle 0|\psi(t)\rangle|^2 \;, \tag{A.1}$$

where $|\psi(t)\rangle$ is the system's state after the time evolution t (see Fig. 4.1c). The Hamiltonian determining the evolution of the state $|\psi(t)\rangle$ is $\hat{\mathcal{H}}_0(t)$ from Eq. (4.1). In particular, for $t > t_{\text{r}}$ we find $\Omega_{1,2}(t) = \Omega$, i.e. $\hat{\mathcal{H}}_0(t) = \hat{\mathcal{H}}_0(t_{\text{r}})$. Thus, for $t > t_{\text{r}}$ the time evolution is given by
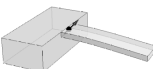
$$|\psi(t)\rangle = \text{e}^{-\text{i}(t-t_{\text{r}})\hat{\mathcal{H}}_0(t_{\text{r}})/\hbar}\,|\psi(t_{\text{r}})\rangle \;, \tag{A.2}$$

where $|\psi(t_{\text{r}})\rangle$ is the state after the state transfer is accomplished.

If we successfully prepare our system in a single dressed state, i.e. $|\psi(t_{\text{r}})\rangle = |\Psi_{+1}\rangle$, its evolution reads

$$|\psi(t)\rangle = \text{e}^{-\text{i}(t-t_{\text{r}})\hat{\mathcal{H}}_0(t_{\text{r}})/\hbar}\,|\Psi_{+1}\rangle = \text{e}^{-\text{i}(t-t_{\text{r}})E_{+1}/\hbar}\,|\Psi_{+1}\rangle \;, \tag{A.3}$$

where E_{+1} denotes the eigenenergy corresponding to $|\Psi_{+1}\rangle$. Thus, the eigenenergy characterizes the dynamical phase its eigenstate accumulates during the evolution. As

we read out the state $|0\rangle = (|\Psi_{-1}\rangle + |\Psi_0\rangle + |\Psi_{+1}\rangle)/\sqrt{3}$, the measured population $P_{|0\rangle}(t)$ can be expressed as

$$P_{|0\rangle}(t) = \frac{1}{3} \left| \sum_{k=0,\pm 1} \left\langle \Psi_k \middle| e^{-i(t-t_r)E_{+1}/\hbar} \middle| \Psi_{+1} \right\rangle \right|^2 = \frac{1}{3} \ . \tag{A.4}$$

Equivalent considerations hold for the other two dressed states, $|\Psi_0\rangle$ and $|\Psi_{-1}\rangle$. Thus, for a perfect state transfer into a single dressed state (in our case $|\Psi_{+1}\rangle$), the measured population for $t > t_r$ is time-independent with a value of $1/3$.

If, however, we do not prepare a single dressed state, but rather a mixture of dressed states, we start the time evolution in $t = t_r$ in $|\psi(t_r)\rangle = \sum_j c_j |\Psi_j\rangle$, with $c_j \in \mathbb{C}$ and $\sum_j |c_j|^2 = 1$ ($j = 0, \pm 1$). In this case, the evolution of the state reads

$$|\psi(t)\rangle = e^{-i(t-t_r)\hat{\mathcal{H}}_0(t_r)/\hbar} \sum_{j=0,\pm 1} c_j |\Psi_j\rangle = \sum_{j=0,\pm 1} c_j e^{-i(t-t_r)E_j/\hbar} |\Psi_j\rangle \ , \tag{A.5}$$

as each dressed state $|\Psi_j\rangle$ accumulates a dynamical phase corresponding to its eigenenergy E_j. During the readout we then measure

$$P_{|0\rangle}(t) = \frac{1}{3} \left| \sum_{j,k=0,\pm 1} \left\langle \Psi_k \middle| c_j\, e^{-i(t-t_r)E_j/\hbar} \middle| \Psi_j \right\rangle \right|^2 = \frac{1}{3} \left| \sum_{j=0,\pm 1} c_j\, e^{-i(t-t_r)E_j/\hbar} \right|^2 . \tag{A.6}$$

Thus, the measured time-dependent population is characterized by a beating of the transition frequencies of the dressed states with amplitudes depending on the weighting factors c_j. This can be easily illustrated for the extreme case, where we do not ramp the MW fields at all, but rather switch them on simultaneously, implying $t_r = 0$. In this instance, we start for $t = 0$ in $|0\rangle$, i.e. $c_j = 1/\sqrt{3}$ for all j. According to Eq. (A.6) the measured population then is

$$P_{|0\rangle}(t) = \frac{1}{3} + \frac{2}{9} \left[\cos(2\pi\Delta_{-1,0}t) + \cos(2\pi\Delta_{+1,0}t) + \cos(2\pi\Delta_{+1,-1}t) \right] , \tag{A.7}$$

with $\Delta_{m,n} = (E_m - E_n)/h$. This scenario exactly describes the dynamics observed in Fig. 3.2a [114, 148].

A.3. Details on the TD correction

In this section we provide details on the transformation of Hamiltonian $\hat{\mathcal{H}}_0(t)$ from Eq. (4.1) to the adiabatic basis [168, 183]. For the considered case of $\Phi = \pi/2$ we find in the $\{|-1\rangle, |0\rangle, |+1\rangle\}$ basis

$$\hat{\mathcal{H}}_0(t)/\hbar = \frac{\Omega}{2} \begin{pmatrix} 0 & \sin[\theta(t)] & i \\ \sin[\theta(t)] & 0 & \sin[\theta(t)] \\ -i & \sin[\theta(t)] & 0 \end{pmatrix} \ . \tag{A.8}$$

The corresponding eigenvectors $|\psi_k(t)\rangle$ with $k = 0, \pm 1$ are the instantaneous adiabatic eigenstates, which diagonalize $\hat{\mathcal{H}}_0(t)$ at each instant in time. In the frame, where $\hat{\mathcal{H}}_0(t)$

is diagonal, we denote these adiabatic eigenstates $|\psi_k\rangle$, as they are time-independent. The unitary transformation from the $\{|m_s\rangle\}$ basis to the adiabatic frame then reads

$$\hat{\mathcal{U}}(t) = \sum_{k=0,\pm 1} |\psi_k\rangle\langle\psi_k(t)| \ , \tag{A.9}$$

which maps the adiabatic eigenstates $|\psi_k(t)\rangle$ onto the time-independent states $|\psi_k\rangle$. Specifically, we obtain $\hat{\mathcal{U}}(t)$ from its inverse $\hat{\mathcal{U}}^\dagger(t)$, whose columns contain the $|\psi_k(t)\rangle$. We find

$$\hat{\mathcal{U}}^\dagger(t) = \begin{pmatrix} \frac{1}{2} + \frac{i}{2\sqrt{2-\cos[2\theta(t)]}} & -\frac{\sin[\theta(t)]}{\sqrt{2-\cos[2\theta(t)]}} & \frac{1}{2} - \frac{i}{2\sqrt{2-\cos[2\theta(t)]}} \\ \frac{\sin[\theta(t)]}{\sqrt{2-\cos[2\theta(t)]}} & -\frac{i}{\sqrt{2-\cos[2\theta(t)]}} & -\frac{\sin[\theta(t)]}{\sqrt{2-\cos[2\theta(t)]}} \\ \frac{1}{2} - \frac{i}{2\sqrt{2-\cos[2\theta(t)]}} & \frac{\sin[\theta(t)]}{\sqrt{2-\cos[2\theta(t)]}} & \frac{1}{2} + \frac{i}{2\sqrt{2-\cos[2\theta(t)]}} \end{pmatrix} \ . \tag{A.10}$$

To yield the Hamiltonian in the adiabatic frame, we have to consider the Schrödinger equation. For a state $|\xi\rangle$ in the adiabatic frame, whose equivalent in the $\{|m_s\rangle\}$ basis is given by $|\xi(t)\rangle = \hat{\mathcal{U}}^\dagger(t)|\xi\rangle$, the Schrödinger equation reads

$$i\hbar\,\partial_t\left[\hat{\mathcal{U}}^\dagger(t)|\xi\rangle\right] = \hat{\mathcal{H}}_0(t)\left[\hat{\mathcal{U}}^\dagger(t)|\xi\rangle\right] \ . \tag{A.11}$$

Multiplying both sides with $\hat{\mathcal{U}}(t)$ from the left and rearranging the terms results in

$$i\hbar\,\partial_t|\xi\rangle = \hat{\mathcal{H}}_0^{\text{ad}}(t)|\xi\rangle \ , \tag{A.12}$$

where the Hamiltonian in the adiabatic frame is given by

$$\hat{\mathcal{H}}_0^{\text{ad}}(t) = \hat{\mathcal{U}}(t)\,\hat{\mathcal{H}}_0(t)\,\hat{\mathcal{U}}^\dagger(t) - i\hbar\hat{\mathcal{U}}(t)\,\partial_t\hat{\mathcal{U}}^\dagger(t) \ , \tag{A.13}$$

as stated in Eq. (4.10). Using Eq. (A.10) and Eq. (A.13) yields the expression of Eq. (4.11),

$$\hat{\mathcal{H}}_0^{\text{ad}}(t)/\hbar = \begin{pmatrix} \frac{\Omega}{2}\sqrt{2-\cos[2\theta(t)]} & \frac{\cos[\theta(t)]\,\partial_t\theta(t)}{2-\cos[2\theta(t)]} & 0 \\ \frac{\cos[\theta(t)]\,\partial_t\theta(t)}{2-\cos[2\theta(t)]} & 0 & -\frac{\cos[\theta(t)]\,\partial_t\theta(t)}{2-\cos[2\theta(t)]} \\ 0 & -\frac{\cos[\theta(t)]\,\partial_t\theta(t)}{2-\cos[2\theta(t)]} & -\frac{\Omega}{2}\sqrt{2-\cos[2\theta(t)]} \end{pmatrix} \ . \tag{A.14}$$

To get rid of the off-diagonal elements in $\hat{\mathcal{H}}_0^{\text{ad}}(t)$, the TD correction adds additional control fields expressed by $\hat{\mathcal{H}}_{\text{TD}}(t)$ to the Hamiltonian. Motivated by Eq. (A.13) the correction reads

$$\hat{\mathcal{H}}_{\text{TD}}(t) = i\hbar\left[\partial_t\hat{\mathcal{U}}^\dagger(t)\right]\hat{\mathcal{U}}(t) \ , \tag{A.15}$$

such that $\hat{\mathcal{U}}(t)\,\hat{\mathcal{H}}_{\text{TD}}(t)\,\hat{\mathcal{U}}^\dagger(t) = i\hbar\hat{\mathcal{U}}(t)\,\partial_t\hat{\mathcal{U}}^\dagger(t)$ cancels the second term on the right hand side in Eq. (A.13). Note that Eq. (A.13) is in the adiabatic basis, whereas Eq. (A.15) is in the $\{|m_s\rangle\}$ basis. Inserting the corresponding expressions into Eq. (A.15) yields in the $\{|-1\rangle, |0\rangle, |+1\rangle\}$ basis,

$$\hat{\mathcal{H}}_{\text{TD}}(t)/\hbar = \begin{pmatrix} 0 & \frac{\cos[\theta(t)]\,\partial_t\theta(t)}{2-\cos[2\theta(t)]} & 0 \\ \frac{\cos[\theta(t)]\,\partial_t\theta(t)}{2-\cos[2\theta(t)]} & 0 & -\frac{\cos[\theta(t)]\,\partial_t\theta(t)}{2-\cos[2\theta(t)]} \\ 0 & -\frac{\cos[\theta(t)]\,\partial_t\theta(t)}{2-\cos[2\theta(t)]} & 0 \end{pmatrix} \ . \tag{A.16}$$
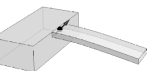
Adding this correction to the initial Hamiltonian (A.8), we find that the TD corrected MW pulses are

$$\Omega_{1,(2)}(t) = \Omega \sin[\theta(t)] \, (\overset{+}{\scriptstyle -}) \, 2 \cdot \frac{\cos[\theta(t)] \, \partial_t \theta(t)}{2 - \cos[2\theta(t)]} \; . \tag{A.17}$$

Experimentally we can easily implement TD corrected MW pulses with $0 \le \Omega_{1,2}(t) \le \Omega$, which require the parameter ν to be $\nu \le \Omega/2$. If we choose $\nu > \Omega/2$, however, the TD corrected ramps would lead to negative amplitude values, which we cannot realize in our current setup, as flipping the phase of the signal generation fields does not influence the final driving fields' phases (see App. A.1.2). In Fig. A.2a we illustrate an example for such a ramp for $\nu = 3\Omega/4$. For even higher values of ν some amplitudes additionally overshoot the steady state driving amplitude Ω (see Fig. A.2b for $\nu = 5\Omega/4$).

The theoretically derived TD corrections from Eq. (A.17) do not account for the unavoidable experimental uncertainties that cause the residual small oscillations in $P_{|0\rangle}(t)$ after the state transfer (see Fig. 4.3c). Most importantly, our measurements are affected by slow fluctuations in the magnetic environment of the NV caused by nearby nuclear spins (^{14}N or ^{13}C) and by uncertainties in setting the driving field parameters. To estimate the influence of these errors we simulate our measurements. The magnetic fluctuations are characterized by a zero-mean Gaussian distribution of the MW field detunings with a width of $\sigma_{T_2^*}/2\pi = 1/(\sqrt{2}\pi T_2^*) = 107\,\mathrm{kHz}$ [220], where $T_2^* = 2.1(1)\,\mu\mathrm{s}$ is the NV's dephasing time (see Sec. 2.3.3). As the timescale of these fluctuations is typically long compared to a single simulated measurement run, but far shorter than the total measurement time, we keep these detunings constant during a single run but change them between different runs. The uncertainties in setting the driving field parameters mostly affect the MW field strengths. We measure the driving strengths by performing Rabi oscillations on each of the MW transitions of the bare NV states and extract the Rabi frequency by fitting with an exponentially decaying single sinusoid. Due to fluctuations in, for example, the sample-antenna separation, as well as the MW amplifier, the measured Rabi frequencies show, however, relative deviations of up to $2\,\%$ for the same applied MW power ($\approx 4\,\mathrm{dBm}$ from the MW
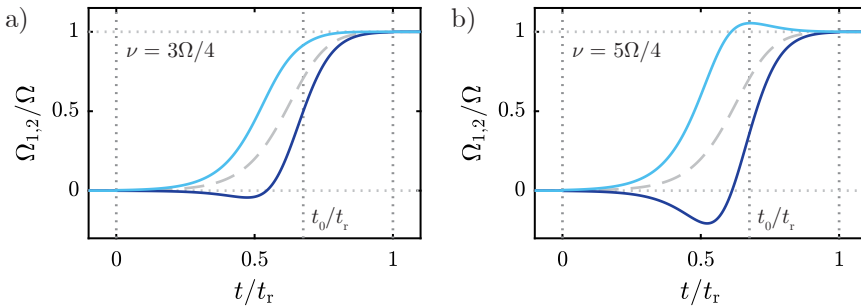

Figure A.2.: Theoretically calculated TD corrected envelopes of the MW driving fields $\nu > \Omega/2$. a) For $\nu = 3\Omega/4$ one of the optimized ramps has negative amplitude values, which we cannot implement in our current setup. b) Increasing ν further additionally leads to overshoots in the other ramp, e.g. here displayed for $\nu = 5\Omega/4$.
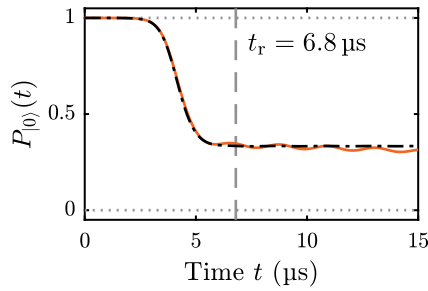
Figure A.3.: Simulated influence of experimental uncertainties on the state preparation process. While the unperturbed system shows no oscillations after the state transfer (black), considering experimental uncertainties in the simulations reveals the experimentally observed oscillations (orange). The choosen parameters are: $\nu = \Omega/2$, $\Omega/2\pi = 510\,\text{kHz}$, $\Omega_1^{\text{max}}/2\pi = 520\,\text{kHz}$, $\Omega_2^{\text{max}}/2\pi = 500\,\text{kHz}$ (i.e. 2 % opposing deviation for both MW fields), $\Phi = 0.495 \cdot \pi/2$. The perturbed simulation is averaged over 100 times, with each iteration using a different MW detuning drawn from a zero-mean Gaussian distribution characterized by $\sigma_{T_2^*}/2\pi = 107\,\text{kHz}$.

generator in our case). Moreover, setting the global phase value exactly to $\Phi = \pi/2$ has experimental limitations. We determine the corresponding phase value by sweeping the mechanical phase with a finite sampling rate while maintaining the MW fields constant and fitting the averaged time traces of the resulting interference pattern (see Fig. 3.2a) for evolution times between $1\,\mu\text{s}$ and $1.7\,\mu\text{s}$. This allows us to determine the value of the global phase with a 2σ uncertainty of 0.9°.

Considering these effects, we simulated the time evolution of $P_{|0\rangle}(t)$ averaged over 100 normally distributed MW detunings (see Fig. A.3). Thereby, we include the mentioned uncertainties in a worst-case scenario, i.e. using the maximum global phase error and the maximum deviation in drive strengths. As a result, the time evolution clearly shows residual oscillations after the state transfer, similar to those observed in the experiment.

We note that there are additional sources for experimental uncertainties that we neglect in our simulation, for example, the feedthrough of the MW signals, which leads to non-vanishing MW amplitudes at the beginning of the state transfer, amplitude and frequency noise of the driving fields, as well as fluctuations in the zero-field splitting of the NV induced by variations in temperature or environmental strain or electric fields (see Sec. 2.2).

A.4. STA for arbitrary global phase values

In Chap. 4, we focused on the global phase of $\Phi = \pi/2$ for demonstrating the initialization of dressed states with STA. This particular phase value allows for a straightforward and analytical calculation of the TD correction, which fulfills our experimental conditions, i.e. no time-dependent phase control of the MW fields and no time-dependent control of the mechanical amplitude. However, for other phase values the TD corrections cannot be calculated analytically anymore and/or does not satisfy
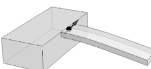
the experimental requirements. In this case, STA can be found by using the dressed state approach introduced in [185]. As presented in [183], the basic idea is to modify the MW fields of the Hamiltonian $\hat{\mathcal{H}}_0(t)$ from Eq. (4.1) in such a way that the state transfer is realized without errors even when the protocol time is not long compared to the instantaneous adiabatic gap. These modifications can be described by an additional control term $\hat{\mathcal{W}}(t)$ added to the initial Hamiltonian, i.e. $\hat{\mathcal{H}}_0(t) \to \hat{\mathcal{H}}_0(t) + \hat{\mathcal{W}}(t)$. We can parametrize $\hat{\mathcal{W}}(t)$ as

$$\hat{\mathcal{W}}(t) = W_1(t)\,|-1\rangle\langle 0| + W_2(t)\,|+1\rangle\langle 0| + \text{H.c.} \ , \tag{A.18}$$

where we require $W_{1,2}(t)$ to be real valued functions in order to ensure no time-dependent phase control of the MW driving fields. We, however, note that if time-dependent phase control is available, then $W_{1,2}(t)$ can also be complex valued. We also note that $\hat{\mathcal{W}}(t)$ does not include couplings of $|-1\rangle$ and $|+1\rangle$, as this would require control of the mechanical driving field. Taking possible time-dependent control of the mechanical field into account, Eq. (A.18) can be generalized even further.

There is an infinite amount of possible $\hat{\mathcal{W}}(t)$, each of them being associated with a specific dressing of the instantaneous eigenstate used to realize the adiabatic state transfer. To keep things simple, we choose $\hat{\mathcal{W}}(t)$ such that in the dressed adiabatic frame the evolution of the dressed state used for state transfer is trivial. In other words, we want to stay in this particular dressed state for the whole duration of the protocol. In our case, the transformation from the adiabatic frame to the dressed adiabatic frame can be generated by the unitary operator

$$\hat{\mathcal{U}}_{\text{dr}}(t) = \prod_j \mathrm{e}^{\mathrm{i}\varphi_j(t)\hat{\Lambda}_j} \ , \tag{A.19}$$

where $\hat{\Lambda}_j$ are the generators of SU(3) and $\varphi_j(t)$ must obey the conditions $\varphi_j(0) = \varphi_j(t_{\text{r}}) = 0$ to ensure that the dressed states correspond to the adiabatic states at the beginning ($|0\rangle$, $|-\rangle$, and $|+\rangle$) and at the end ($|\Psi_{0,\pm 1}\rangle$) of the protocol. This condition ensures that one starts and ends in the desired state.

To be more specific, we explicitly derive the equations to determine $\hat{\mathcal{W}}(t)$ in our case. We start by calculating the instantaneous adiabatic eigenstates $|\psi_k(t)\rangle$ of $\hat{\mathcal{H}}_0(t)$ for a general Φ. To that end, we need to solve the eigenvalue problem

$$\hat{\mathcal{H}}_0(t)\,|\psi_k(t)\rangle = E_k(t)\,|\psi_k(t)\rangle \ , \tag{A.20}$$

with $k = 0, \pm 1$. We find the instantaneous eigenenergies

$$E_k(t)/\hbar = \frac{\Omega}{\sqrt{3}}\sqrt{1 + 2\mathcal{R}(t)^2}\cdot\cos\left[\frac{1}{3}\cos^{-1}\left(3\sqrt{3}\cdot\frac{\cos(\Phi)\,\mathcal{R}(t)^2}{[1 + 2\mathcal{R}(t)^2]^{3/2}}\right) - \frac{2\pi}{3}k\right] \ , \tag{A.21}$$

where $\mathcal{R}(t) = \Omega_{1,2}(t)/\Omega = \sin[\theta(t)]$. The associated adiabatic eigenstates read

$$|\psi_k(t)\rangle = \frac{1}{N_k(t)}\Big(\mathcal{R}(t)\big[\Omega\mathrm{e}^{-\mathrm{i}\Phi} + 2E_k(t)\big]|+1\rangle - \big[\Omega^2 - 4E_k(t)\big]|0\rangle +$$
$$+ \mathcal{R}(t)\big[\Omega\mathrm{e}^{\mathrm{i}\Phi} + 2E_k(t)\big]|-1\rangle\Big) \ , \tag{A.22}$$

where the normalization factor is

$$N_k(t) = \left(\left[\Omega^2 - 4E_k^2(t) \right]^2 + 2\mathcal{R}(t)^2 \left[\Omega^2 + 4E_k(t) \left(\Omega\cos(\Phi) + E_k(t) \right) \right] \right)^{1/2} .$$
(A.23)

As introduced in Eq. (4.9), the unitary transformation to the adiabatic frame is

$$\hat{\mathcal{U}}(t) = \sum_{k=0,\pm 1} |\psi_k\rangle\langle\psi_k(t)| \; ,$$
(A.24)

where $|\psi_k\rangle$ are the time-independent eigenstates in the adiabatic frame. By definition, the transformation $\hat{\mathcal{U}}(t)\,\hat{\mathcal{H}}_0(t)\,\hat{\mathcal{U}}^\dagger(t)$ diagonalizes $\hat{\mathcal{H}}_0(t)$ at each instant in time.

With that, we can express the dressed adiabatic Hamiltonian as

$$\hat{\mathcal{H}}_0^{\mathrm{dr}}(t) = \hat{\mathcal{U}}_{\mathrm{dr}}(t)\Big[\hat{\mathcal{U}}(t)\,\hat{\mathcal{H}}_0(t)\,\hat{\mathcal{U}}^\dagger(t) - i\hbar\hat{\mathcal{U}}(t)\,\partial_t\hat{\mathcal{U}}^\dagger(t) + \hat{\mathcal{U}}(t)\,\hat{\mathcal{W}}(t)\,\hat{\mathcal{U}}^\dagger(t)\Big]\hat{\mathcal{U}}_{\mathrm{dr}}^\dagger(t) +$$
$$- i\hbar\hat{\mathcal{U}}_{\mathrm{dr}}(t)\,\partial_t\hat{\mathcal{U}}_{\mathrm{dr}}^\dagger(t) \; , \quad \text{(A.25)}$$

and the corresponding dressed adiabatic states as

$$|\tilde{\psi}_k\rangle = \hat{\mathcal{U}}_{\mathrm{dr}}(t)\,|\psi_k\rangle \; .$$
(A.26)

In this new dressed adiabatic frame defined by $\hat{\mathcal{U}}_{\mathrm{dr}}(t)$ the dressed states $|\tilde{\psi}_k\rangle$ have no intrinsic time dependence. In our case the adiabatic state transfer is realized through $|\psi_{+1}(t)\rangle$ (see Fig. 4.1b). To ensure the desired trivial dynamics in the dressed adiabatic frame, we, therefore, ask $|\tilde{\psi}_{+1}\rangle$ to be decoupled from the other dressed states. This condition can be written as

$$\langle\tilde{\psi}_{+1}|\hat{\mathcal{H}}_0^{\mathrm{dr}}(t)|\tilde{\psi}_j\rangle = 0 \; ,$$
(A.27)

with $j = 0, -1$. Solving this system of equations for a chosen dressing finally gives the correction $\hat{\mathcal{W}}(t)$.

As an example, we consider the case $\Phi = 0$. For this value of Φ the TD correction only has purely imaginary matrix elements and the SATD correction [185] requires to control the detunings of all states and the amplitude of the mechanical drive. None of these corrections can be implemented with our current setup. However, using the dressed state method presented above, one can find a STA that respects the constraints of our system. We choose a dressing of the form

$$\hat{\mathcal{U}}_{\mathrm{dr},\Phi=0}(t) = e^{-i\beta(t)/2(|\psi_0\rangle\langle\psi_{+1}|+\mathrm{H.c.})} \; .$$
(A.28)

By using Eq. (A.27) we find that the equation $\langle\tilde{\psi}_{+1}|\hat{\mathcal{H}}_0^{\mathrm{dr}}(t)|\tilde{\psi}_{-1}\rangle = 0$ can be fulfilled by choosing $W_1(t) = W_2(t)$, while $\langle\tilde{\psi}_{+1}|\hat{\mathcal{H}}_0^{\mathrm{dr}}(t)|\tilde{\psi}_0\rangle = 0$ can be fulfilled by solving

$$\beta(t) = \tan^{-1}\left[\frac{4\sqrt{2}\cos[\theta(t)]\,\partial_t\theta(t)}{\sqrt{1+8\sin^2[\theta(t)]}\,\left[\Omega\big(1+8\sin^2[\theta(t)]+16W_1(t)\,\sin[\theta(t)]\big)\right]} \right] ,$$
(A.29a)

$$0 = \frac{\sqrt{2}\,W_1(t)}{\sqrt{1+8\sin^2[\theta(t)]}} - \frac{\partial_t\beta(t)}{2} \; .$$
(A.29b)
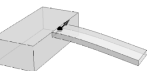
Inserting Eq. (A.29a) into Eq. (A.29b) reveals a differential equation for $W_1(t)$, which can be solved numerically.

As an example, we numerically solved Eq. (A.29a) and Eq. (A.29b) for $\Phi = 0$ and recently performed preliminary measurements employing the resulting STA ramps (see Fig. A.4). To that end, we choose the same values for the discontinuity $\varepsilon = 10^{-3}$ and the slope parameter $\nu = \Omega/2$ as in Chap. 4. In the experiment we set $\Omega/2\pi = 470\,\mathrm{kHz}$, resulting in the ramp time $t_r = 7.4\,\mu\mathrm{s}$. Note that in contrast to the analytic TD approach, which we have chosen at $\Phi = \pi/2$ in Sec. 4.3, the numerical method yields that both MW fields are ramped simultaneously. To benchmark the experimental result we also calculate the expected coherent time evolution of $P_{|0\rangle}(t)$ by solving the time-dependent Schrödinger equation using Hamiltonian (4.1). Importantly, we assume no detunings of the driving fields in our calculations. Under this condition, two dressed states are degenerate at $\Phi = 0$ (compare to Fig. 3.3), so that a perfect state transfer initializes into this degenerate subspace. Based on our calculations we find that in this scenario $P_{|0\rangle}(t)$ theoretically converges to $2/3$ after the ramp time. The experimental time evolution agrees with the theoretical prediction up to $t \lesssim 5\,\mu\mathrm{s}$. However, the measured population then decays from $2/3$ to the time-independent value of $\approx 1/3$, where it stabilizes for $t \gtrsim t_r$. Thereby, the decay rate is slower compared to the decay of the initial evolution for $t \lesssim 5\,\mu\mathrm{s}$. We attribute this discrepancy between experiment and calculation to the presence of detunings, which lift the degeneracy of the dressed states at $\Phi = 0$ (see Fig. 3.3). We, therefore, do no longer prepare the system in the degenerate dressed state subspace, but rather a single dressed state, corresponding to a population of $P_{|0\rangle}(t > t_r) \approx 1/3$ as observed. Due to temperature drifts, the detunings additionally fluctuate during the data acquisition, which results in an effective averaging over different detunings. In this context, we note that the
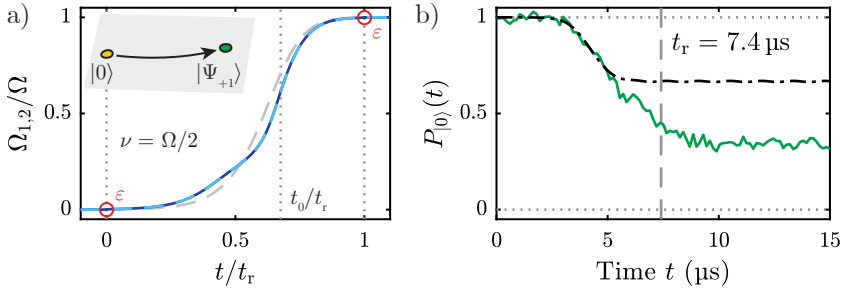

Figure A.4.: Implementation of the STA based on the dressed state approach for $\Phi = 0$. a) Modified MW field amplitudes for $\nu = \Omega/2$, $\Omega/2\pi = 470\,\mathrm{kHz}$, and $\varepsilon = 10^{-3}$. Here, both MW fields are modified similarly with respect to the optimized STIRAP pulse shape (gray dashed). b) Time evolution of measured population $P_{|0\rangle}(t)$ (green) with corresponding calculation (black). The measurement agrees with the simulation up to $t \lesssim 5\,\mu\mathrm{s}$. Then, the measured population drops to $\approx 1/3$, but with a slower rate compared to the initial process. This indicates the preparation of a single dressed state rather than initialization into the degenerate subspace at $\Phi = 0$. Thus, the high vulnerability of the system to environmental noise present at this value of Φ might limit the experiment.

data reveals a kink at $t \approx 5\,\mu s$, which might indicate a successful state transfer to the desired dressed state subspace at the beginning of certain measurements runs. Then, however, fluctuations destabilize the subspace and the system decays into a single dressed state. To successfully realize state transfer at $\Phi = 0$ in future experiments we have to overcome the present experimental limitations, i.e. we need to mitigate unwanted detunings of the driving fields from the transitions and additionally avoid uncertainties in setting the global phase to the desired value. Another approach is to consider possible detunings in the calculation to find STA ramps that are robust against them.

A.5. Derivation of the transition imbalance

To derive the transition imbalance for the $m_I = \pm 1$ hyperfine projections at $\boldsymbol{B} = 0$ (see Eq. (6.8)), we follow [116] and consider the Hamiltonian

$$\hat{\mathcal{H}}/h = (D_0 + \Pi_z)\hat{S}_z^2 \mp |A_{\mathrm{HF}}|\hat{S}_z + \Pi_x\left(\hat{S}_y^2 - \hat{S}_x^2\right) + \Pi_y\left(\hat{S}_x\hat{S}_y + \hat{S}_y\hat{S}_x\right) . \quad (A.30)$$

Note that the sign of the hyperfine interaction is flipped compared to Eq. (6.1) as $A_{\mathrm{HF}} < 0$. Following [115], we use the same procedure as described in Sec. 6.1 and first calculate the corresponding eigenstates

$$\begin{aligned}
|-\rangle &= \frac{1}{\sqrt{1+\lambda^2}}\left(\mathrm{e}^{\mathrm{i}\varphi_\Pi}\,|+1\rangle + \lambda\,|-1\rangle\right) , \\
|+\rangle &= \frac{1}{\sqrt{1+\lambda^2}}\left(\lambda\,\mathrm{e}^{\mathrm{i}\varphi_\Pi}\,|+1\rangle - |-1\rangle\right) ,
\end{aligned} \quad (A.31)$$

where we have defined

$$\lambda = \frac{|A_{\mathrm{HF}}|}{\Pi_\perp}\left[\sqrt{1 + \left(\frac{\Pi_\perp}{|A_{\mathrm{HF}}|}\right)^2} - 1\right] . \quad (A.32)$$

Using Eq. (6.3) and Eq. (6.4), we find for the transition strengths

$$\mathcal{A}_{0,\pm} \sim \frac{1}{\hbar^2}\frac{(2\mu_B B_\perp^{\mathrm{mw}})^2}{2}\frac{1 + \lambda^2 \mp 2\lambda\cos(2\varphi_{\mathrm{mw}} + \varphi_\Pi)}{2(1+\lambda^2)} . \quad (A.33)$$
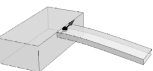
Thus, the transition imbalance $\mathcal{J}$ of the $m_I = \pm 1$ nuclear spin projections at $\boldsymbol{B} = 0$ is given by

$$\mathcal{J} = \frac{\mathcal{A}_{0,+} - \mathcal{A}_{0,-}}{\mathcal{A}_{0,+} + \mathcal{A}_{0,-}} = -\frac{2\lambda}{1+\lambda^2}\cos(2\varphi_{\mathrm{mw}} + \varphi_\Pi) . \quad (A.34)$$

Considering the case $\Pi_\perp \ll |A_{\mathrm{HF}}|$, we can approximate $\lambda \approx \frac{\Pi_\perp}{2|A_{\mathrm{HF}}|}$ and then find to first order that the imbalance reads

$$\mathcal{J} \approx -\frac{\Pi_\perp}{|A_{\mathrm{HF}}|}\cos(2\varphi_{\mathrm{mw}} + \varphi_\Pi) , \quad (A.35)$$

as stated in Eq. (6.8).

A.6. Simulation of ESR spectra

In this section we present the MATLAB code that was used to simulate the ESR
spectra in Chap. 6. In particular, we provide the code to generate the NV ground
state Hamiltonian, to generate the interaction Hamiltonian with a MW magnetic
field, and to calculate the ESR transition strength for a given set of external fields.
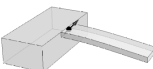
A.6.1. Ground state spin Hamiltonian

```matlab
function [Hgs] = NV_GS_Hamiltonian(BField, EField, Stress)
% NV_GS_Hamiltonian generates the ground state Hamiltonian of the
% NV spin under external perturbations including hyperfine structure
% Refer to Eq. (2.1), (2.3), (2.4), and (2.5)

% Input parameters
%   BField = [Bx, By, Bz] (in G): Magnetic field vector in NV frame
%   EField = [Ex, Ey, Ez] (in V/m): Electric field vector in NV frame
%   Stress = [Mx, My, Mz, Nx, Ny] (in MHz): Spin-stress interaction ...
%       parameters

% Output parameter
%   Hgs (in MHz): NV ground state spin Hamiltonian


%% Constants and definitions

    % NV fine and hyperfine constants
    D0 = 2870; % Zero-field splitting (in MHz)
    Apar = -2.14; % Axial hyperfine parameter (in MHz)
    Aperp = -2.7; % Non-axial hyperfine parameter (in MHz)
    PQ = -4.95; % Electric quadrupole parameter (in MHz)

    % Magnetic coupling constants
    muB = 9.274e-24; % Bohr magneton (in J/T)
    gNV = 2.0028; % Electron-g-factor (scalar)
    muN = 5.051e-27; % Nuclear magneton (in J/T)
    gN = 0.404; % N14 nuclear-g-factor (scalar)
    h = 6.626e-34; % Planck's constant (in Js)

    gammaNV = muB*gNV/h/1e10; % NV gyromagnetic ratio (in MHz/G)
    gammaN = muN*gN/h/1e10; % N14 gyromagnetic ratio (in MHz/G)

    % Electric coupling constants
    dpar = 0.35e-8; % Axial electric field susceptibility (in MHz m/V)
    dperp = 17e-8; % Transverse electric field susceptibility (in MHz ...
        m/V)

    % Spin-1 operators
    Sx = 1./sqrt(2).*[0 1 0; 1 0 1; 0 1 0];
    Sy = 1./sqrt(2)./1i.*[0 1 0; -1 0 1; 0 -1 0];
    Sz = [1 0 0; 0 0 0; 0 0 -1];
    SI = [1 0 0; 0 1 0; 0 0 1];


```

```matlab
45  %% Hamiltonian
46
47      % Fine and hyperfine terms
48      HZFS = D0.*kron(Sz*Sz - 2/3*SI,SI); % Zero-field splitting
49      HHFPar = Apar.*kron(Sz,Sz); % Axial hyperfine interaction
50      HHFPerp = Aperp.*(kron(Sx,Sx) + kron(Sy,Sy)); % Non-axial ...
            hyperfine interaction
51      HNucQ = PQ.*kron(SI,(Sz*Sz - 2/3*SI)); % Nuclear quadrupole ...
            interaction
52
53      % Magnetic field coupling terms
54      HBEl = gammaNV.*kron(BField(1).*Sx + BField(2).*Sy + ...
            BField(3).*Sz,SI); % Electric Zeeman coupling
55      HBNuc = gammaN.*kron(SI,BField(1).*Sx + BField(2).*Sy + ...
            BField(3).*Sz); % Nuclear Zeeman coupling
56
57      % Electric field coupling terms
58      HEl0 = dpar.*EField(3).*kron(Sz*Sz - 2/3*SI,SI); % Axial electric ...
            field coupling
59      HEl2 = dperp.*EField(1).*kron(Sy*Sy - Sx*Sx,SI) + ...
            dperp.*EField(2).*kron(Sx*Sy + Sy*Sx,SI); % Transverse ...
            electric field coupling
60
61      % Spin-stress coupling terms
62      HStrain0 = Stress(3).*kron(Sz*Sz,SI);
63      HStrain1 = Stress(4).*kron(Sx*Sz + Sz*Sx,SI) + ...
            Stress(5).*kron(Sy*Sz + Sz*Sy,SI);
64      HStrain2 = Stress(1).*kron(Sy*Sy - Sx*Sx,SI) + ...
            Stress(2).*kron(Sx*Sy + Sy*Sx,SI);
65
66      % Total NV ground state Hamiltonian
67      Hgs = HZFS + HHFPar + HHFPerp + HNucQ + HBEl + HBNuc + HEl0 + ...
            HEl2 + HStrain0 + HStrain1 + HStrain2;
68
69      % Reference all energies to the energy of |0,0>
70      Hgs = Hgs - eye(9,9).*Hgs(5,5);
71  end
```

A.6.2. Interaction Hamiltonian with a MW magnetic field

```matlab
1  function [Hint] = NV_GS_Hamiltonian_MWprobe(Bmw)
2  % NV_GS_Hamiltonian_MWprobe generates the interaction Hamiltonian of
3  % the NV ground state with a MW magnetic field
4  % Refer to Eq. (2.3)
5
6  % Input parameter
7  %   Bmw = [Bmwx, Bmwy, Bmwz] (in G): MW field amplitude vector in NV ...
        frame
8
9  % Output parameter
10 %   Hint (in MHz): Interaction Hamiltonian between NV spin and MW field
11
12
13 %% Constants and definitions
14
15     % Magnetic coupling constants
16     muB = 9.274e-24; % Bohr magneton (in J/T)
17     gNV = 2.0028; % Electron-g-factor (scalar)
18     muN = 5.051e-27; % Nuclear magneton (in J/T)
19     gN = 0.404; % N14 nuclear-g-factor (scalar)
20     h = 6.626e-34; % Planck's constant (in Js)
21
22     gammaNV = muB*gNV/h/1e10; % NV gyromagnetic ratio (in MHz/G)
23     gammaN = muN*gN/h/1e10; % N14 gyromagnetic ratio (in MHz/G)
24
25     % Spin-1 operators
26     Sx = 1./sqrt(2).*[0 1 0; 1 0 1; 0 1 0];
27     Sy = 1./sqrt(2)./1i.*[0 1 0; -1 0 1; 0 -1 0];
28     Sz = [1 0 0; 0 0 0; 0 0 -1];
29     SI = [1 0 0; 0 1 0; 0 0 1];
30
31
32 %% Interaction Hamiltonian
33
34     % Magnetic field coupling terms
35     HintEl = gammaNV.*kron(Bmw(1).*Sx + Bmw(2).*Sy + Bmw(2).*Sz,SI); ...
            % To electric spin
36     HintNuc = gammaN.*kron(SI,Bmw(1).*Sx + Bmw(2).*Sy + Bmw(3).*Sz); ...
            % To nuclear spin
37
38     % Total interation Hamiltonian
39     Hint = HintEl + HintNuc;
40 end
```

A.6.3. Simulation of ESR spectra

```matlab
1  function [Tstrength] = Simulate_ESR(MWfreq, MWangle, BField, EField, ...
       Stress, Linewidth)
2  % Simulate_ESR calculates the ESR transitions strengths in the NV ground
3  % state under external perturbations
4
5  % Input parameters
6  %    MWfreq (in MHz): Frequency range of MW probe field
7  %    MWangle (in deg): MW polarization angle in xy-plane
8  %    BField = [Bx, By, Bz] (in G): Magnetic field vector in NV frame
9  %    EField = [Ex, Ey, Ez] (in V/m): Electric field vector in NV frame
10 %    Stress = [Mx, My, Mz, Nx, Ny] (in MHz): Spin-stress interaction ...
       parameters
11 %    Linewidth (in MHz): Transition linewidths
12
13 % Output parameter
14 %    Tstrength (scalar): Transition strengths (to be normalized)
15
16     % MW interaction Hamiltonian
17     Bmw = [cosd(MWangle), sind(MWangle), 0]; % Normalized MW field ...
           amplitude
18     Hint = NV_GS_Hamiltonian_MWprobe(Bmw); % Interaction Hamiltonian
19     nMW = length(MWfreq); % Number of frequency points
20
21     % NV ground state Hamiltonian
22     Hgs = NV_GS_Hamiltonian(BField,EField,Stress);
23     [eVecs,eVals] = eig(Hgs);
24     eVals = diag(eVals);
25
26     % Calculate transition strengths
27     TS = zeros(nMW,9,9); % Initialize state resolved transition ...
           strength parameter
28     for initS = 1:9 % Sweep over all initial states
29         initFreq = eVals(initS); % frequency
30         initVec = eVecs(:,initS)./norm(eVecs(:,initS)); % state
31
32         for finS = initS:9 % Sweep over all final states
33             finFreq = eVals(finS); % frequency
34             finVec = eVecs(:,finS)./norm(eVecs(:,finS)); % state
35
36             % Transition matrix element and transition amplitude
37             TME = conj(finVec)'*Hint*initVec;
38             TA = conj(TME)*TME;
39
40             for aMW = 1:nMW % Sweep MW field
41                 TS(aMW,initS,finS) = ...
                       TA.*Linewidth.^2./4./((MWfreq(aMW) - ...
                       abs(finFreq-initFreq)).^2 + Linewidth.^2./4);
42             end
43         end
44     end
45     % Sum over all final states per initial state
46     TSinit = sum(TS,3);
47     % Sum over all initial states
48     Tstrength = sum(TSinit,2);
49 end
```
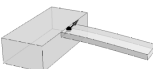
B. Bibliography

[1] M. A. Eriksson, S. N. Coppersmith, and M. G. Lagally, *Semiconductor quantum dot qubits*, MRS Bulletin **38**, 794 (2013).

[2] F. A. Zwanenburg, A. S. Dzurak, A. Morello, M. Y. Simmons, L. C. L. Hollenberg, G. Klimeck, S. Rogge, S. N. Coppersmith, and M. A. Eriksson, *Silicon quantum electronics*, Review of Modern Physics **85**, 961 (2013).

[3] X. Zhang, H.-O. Li, K. Wang, G. Cao, M. Xiao, and G.-P. Guo, *Qubits based on semiconductor quantum dots*, Chinese Physics B **27**, 020305 (2018).

[4] J. Clarke and F. K. Wilhelm, *Superconducting quantum bits*, Nature **453**, 1031 (2008).

[5] W. D. Oliver and P. B. Welander, *Materials in superconducting quantum bits*, MRS Bulletin **38**, 816 (2013).

[6] M. Kjaergaard, M. E. Schwartz, J. Braumüller, P. Krantz, J. I.-J. Wang, S. Gustavsson, and W. D. Oliver, *Superconducting qubits: Current state of play*, Annual Review of Condensed Matter Physics **11**, 369 (2020).

[7] I. Bloch, *Quantum coherence and entanglement with ultracold atoms in optical lattices*, Nature **453**, 1016 (2008).

[8] S. Camerer, M. Korppi, A. Jöckel, D. Hunger, T. W. Hänsch, and P. Treutlein, *Realization of an optomechanical interface between ultracold atoms and a membrane*, Physical Review Letters **107**, 223001 (2011).

[9] M. Saffman, *Quantum computing with atomic qubits and Rydberg interactions: Progress and challenges*, Journal of Physics B: Atomic, Molecular and Optical Physics **49**, 202001 (2016).

[10] D. Rugar, R. Budakian, H. J. Mamin, and B. W. Chui, *Single spin detection by magnetic resonance force microscopy*, Nature **430**, 329 (2004).

[11] L. Gordon, J. R. Weber, J. B. Varley, A. Janotti, D. D. Awschalom, and C. G. Van de Walle, *Quantum computing with defects*, MRS Bulletin **38**, 802 (2013).

[12] D. D. Awschalom, R. Hanson, J. Wrachtrup, and B. B. Zhou, *Quantum technologies with optically interfaced solid-state spins*, Nature Photonics **12**, 516 (2018).

[13] A. B. Klimov, R. Guzmán, J. C. Retamal, and C. Saavedra, *Qutrit quantum computer with trapped ions*, Physical Review A **67**, 062313 (2003).
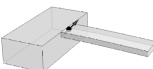
[14] T. C. Ralph, K. J. Resch, and A. Gilchrist, *Efficient Toffoli gates using qudits*, Physical Review A **75**, 022313 (2007).

[15] B. P. Lanyon, M. Barbieri, M. P. Almeida, T. Jennewein, T. C. Ralph, K. J. Resch, G. J. Pryde, J. L. O'Brien, A. Gilchrist, and A. G. White, *Simplifying quantum logic using higher-dimensional Hilbert spaces*, Nature Physics **5**, 134 (2009).

[16] D. Collins, N. Gisin, N. Linden, S. Massar, and S. Popescu, *Bell inequalities for arbitrarily high-dimensional systems*, Physical Review Letters **88**, 040404 (2002).

[17] D. Kaszlikowski, L. C. Kwek, J.-L. Chen, M. Żukowski, and C. H. Oh, *Clauser-Horne inequality for three-state systems*, Physical Review A **65**, 032118 (2002).

[18] D. Bruß and C. Macchiavello, *Optimal eavesdropping in cryptography with three-dimensional quantum states*, Physical Review Letters **88**, 127901 (2002).

[19] N. J. Cerf, M. Bourennane, A. Karlsson, and N. Gisin, *Security of quantum key distribution using d-level systems*, Physical Review Letters **88**, 127902 (2002).

[20] S. H. Autler and C. H. Townes, *Stark effect in rapidly varying fields*, Physical Review **100**, 703 (1955).

[21] H. R. Gray, R. M. Whitley, and C. R. Stroud, *Coherent trapping of atomic populations*, Optics Letters **3**, 218 (1978).

[22] B. D. Agap'ev, M. B. Gornyĭ, B. G. Matisov, and Y. V. Rozhdestvenskiĭ, *Coherent population trapping in quantum systems*, Physics-Uspekhi **36**, 763 (1993).

[23] M. Fleischhauer, A. Imamoglu, and J. P. Marangos, *Electromagnetically induced transparency: Optics in coherent media*, Review of Modern Physics **77**, 633 (2005).

[24] K. Bergmann, N. V. Vitanov, and B. W. Shore, *Perspective: Stimulated Raman adiabatic passage: The status after 25 years*, The Journal of Chemical Physics **142**, 170901 (2015).

[25] N. V. Vitanov, A. A. Rangelov, B. W. Shore, and K. Bergmann, *Stimulated Raman adiabatic passage in physics, chemistry, and beyond*, Reviews of Modern Physics **89**, 015006 (2017).

[26] L. Viola and S. Lloyd, *Dynamical suppression of decoherence in two-state quantum systems*, Physical Review A **58**, 2733 (1998).

[27] L. Viola, E. Knill, and S. Lloyd, *Dynamical decoupling of open quantum systems*, Physical Review Letters **82**, 2417 (1999).

[28] P. Facchi, S. Tasaki, S. Pascazio, H. Nakazato, A. Tokuse, and D. A. Lidar, *Control of decoherence: Analysis and comparison of three different strategies*, Physical Review A **71**, 022302 (2005).

[29] G. S. Uhrig, *Keeping a quantum bit alive by optimized pi-pulse sequences*, Physical Review Letters **98**, 100504 (2007).

[30] Z.-H. Wang, G. de Lange, D. Ristè, R. Hanson, and V. V. Dobrovitski, *Comparison of dynamical decoupling protocols for a nitrogen-vacancy center in diamond*, Physical Review B **85**, 155204 (2012).

[31] J. Du, X. Rong, N. Zhao, Y. Wang, J. Yang, and R. B. Liu, *Preserving electron spin coherence in solids by optimal dynamical decoupling*, Nature **461**, 1265 (2009).

[32] G. de Lange, Z. H. Wang, D. Ristè, V. V. Dobrovitski, and R. Hanson, *Universal dynamical decoupling of a single solid-state spin from a spin bath*, Science **330**, 60 (2010).

[33] C. A. Ryan, J. S. Hodges, and D. G. Cory, *Robust decoupling techniques to extend quantum coherence in diamond*, Physical Review Letters **105**, 200402 (2010).

[34] B. Naydenov, F. Dolde, L. T. Hall, C. Shin, H. Fedder, L. C. L. Hollenberg, F. Jelezko, and J. Wrachtrup, *Dynamical decoupling of a single-electron spin at room temperature*, Physical Review B **83**, 081201 (2011).

[35] N. Bar-Gill, L. Pham, A. Jarmola, D. Budker, and R. Walsworth, *Solid-state electronic spin coherence time approaching one second*, Nature Communications **4**, 1743 (2013).

[36] F. F. Fanchini, J. E. M. Hornos, and R. d. J. Napolitano, *Continuously decoupling single-qubit operations from a perturbing thermal bath of scalar bosons*, Physical Review A **75**, 022329 (2007).

[37] P. Rabl, P. Cappellaro, M. V. G. Dutt, L. Jiang, J. R. Maze, and M. D. Lukin, *Strong magnetic coupling between an electronic spin qubit and a mechanical resonator*, Physical Review B **79**, 041302 (2009).

[38] A. Z. Chaudhry and J. Gong, *Decoherence control: Universal protection of two-qubit states and two-qubit gates using continuous driving fields*, Physical Review A **85**, 012315 (2012).

[39] D. A. Golter, T. K. Baldwin, and H. Wang, *Protecting a solid-state spin from decoherence using dressed spin states*, Physical Review Letter **113**, 237601 (2014).

[40] İ. Yalçınkaya, B. Çakmak, G. Karpat, and F. F. Fanchini, *Continuous dynamical decoupling and decoherence-free subspaces for qubits with tunable interaction*, Quantum Information Processing **18**, 156 (2019).

[41] N. Timoney, I. Baumgart, M. Johanning, A. F. Varón, M. B. Plenio, A. Retzker, and C. Wunderlich, *Quantum gates and memory using microwave-dressed states*, Nature **476**, 185 (2011).
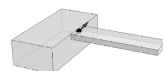
[42] A. Bermudez, P. O. Schmidt, M. B. Plenio, and A. Retzker, *Robust trapped-ion quantum logic gates by continuous dynamical decoupling*, Physical Review A **85**, 040302 (2012).

[43] X. Xu, Z. Wang, C. Duan, P. Huang, P. Wang, Y. Wang, N. Xu, X. Kong, F. Shi, X. Rong, and J. Du, *Coherence-protected quantum gate by continuous dynamical decoupling in diamond*, Physical Review Letters **109**, 070502 (2012).

[44] J.-M. Cai, B. Naydenov, R. Pfeiffer, L. P. McGuinness, K. D. Jahnke, F. Jelezko, M. B. Plenio, and A. Retzker, *Robust dynamical decoupling with concatenated continuous driving*, New Journal of Physics **14**, 113023 (2012).

[45] I. Cohen, N. Aharon, and A. Retzker, *Continuous dynamical decoupling utilizing time-dependent detuning*, Fortschritte der Physik **65**, 1600071 (2017).

[46] J. Teissier, A. Barfuss, and P. Maletinsky, *Hybrid continuous dynamical decoupling: A photon-phonon doubly dressed spin*, Journal of Optics **19**, 044003 (2017).

[47] A. Stark, N. Aharon, T. Unden, D. Louzon, A. Huck, A. Retzker, U. L. Andersen, and F. Jelezko, *Narrow-bandwidth sensing of high-frequency fields with continuous dynamical decoupling*, Nature Communications **8**, 1 (2017).

[48] G. T. Genov, N. Aharon, F. Jelezko, and A. Retzker, *Mixed dynamical decoupling*, Quantum Science and Technology **4**, 035010 (2019).

[49] D. V. Kosachiov, B. G. Matisov, and Y. V. Rozhdestvensky, *Coherent phenomena in multilevel systems with closed interaction contour*, Journal of Physics B: Atomic, Molecular and Optical Physics **25**, 2473 (1992).

[50] M. W. Doherty, N. B. Manson, P. Delaney, F. Jelezko, J. Wrachtrup, and L. C. Hollenberg, *The nitrogen-vacancy colour centre in diamond*, Physics Reports **528**, 1 (2013).

[51] G. D. Fuchs, V. V. Dobrovitski, D. M. Toyli, F. J. Heremans, and D. D. Awschalom, *Gigahertz dynamics of a strongly driven single quantum spin*, Science **326**, 1520 (2009).

[52] A. Barfuss, J. Teissier, E. Neu, A. Nunnenkamp, and P. Maletinsky, *Strong mechanical driving of a single electron spin*, Nature Physics **11**, 820 (2015).

[53] G. Balasubramanian, P. Neumann, D. Twitchen, M. Markham, R. Kolesov, N. Mizuochi, J. Isoya, J. Achard, J. Beck, J. Tissler, V. Jacques, P. R. Hemmer, F. Jelezko, and J. Wrachtrup, *Ultralong spin coherence time in isotopically engineered diamond*, Nature Materials **8**, 383 (2009).

[54] L. M. Pham, N. Bar-Gill, D. Le Sage, C. Belthangady, A. Stacey, M. Markham, D. J. Twitchen, M. D. Lukin, and R. L. Walsworth, *Enhanced metrology using preferential orientation of nitrogen-vacancy centers in diamond*, Physical Review B **86**, 121202 (2012).

[55] A. Gruber, A. Dräbenstedt, C. Tietz, L. Fleury, J. Wrachtrup, and C. von Borczyskowski, *Scanning confocal optical microscopy and magnetic resonance on single defect centers*, Science **276**, 2012 (1997).

[56] J. Harrison, M. J. Sellars, and N. B. Manson, *Optical spin polarisation of the N-V centre in diamond*, Journal of Luminescence **107**, 245 (2004).

[57] F. Jelezko and J. Wrachtrup, *Single defect centres in diamond: A review*, physica status solidi (a) **203**, 3207 (2006).

[58] V. Acosta and P. Hemmer, *Nitrogen-vacancy centers: Physics and applications*, MRS Bulletin **38**, 127 (2013).

[59] L. Childress and R. Hanson, *Diamond NV centers for quantum computing and quantum networks*, MRS Bulletin **38**, 134 (2013).

[60] L. Childress, R. Walsworth, and M. Lukin, *Atom-like crystal defects: From quantum computers to biological sensors*, Physics Today **67**, 38 (2014).

[61] R. Schirhagl, K. Chang, M. Loretz, and C. L. Degen, *Nitrogen-Vacancy centers in diamond: Nanoscale sensors for physics and biology*, Annual Review of Physical Chemistry **65**, 83 (2014).

[62] F. Casola, T. van der Sar, and A. Yacoby, *Probing condensed matter physics with magnetometry based on nitrogen-vacancy centres in diamond*, Nature Reviews Materials **3**, 1 (2018).

[63] F. Jelezko, T. Gaebel, I. Popa, A. Gruber, and J. Wrachtrup, *Observation of coherent oscillations in a single electron spin*, Physical Review Letters **92**, 076401 (2004).

[64] V. Dobrovitski, G. Fuchs, A. Falk, C. Santori, and D. Awschalom, *Quantum control over single spins in diamond*, Annual Review of Condensed Matter Physics **4**, 23 (2013).

[65] Z. Yin, N. Zhao, and T. Li, *Hybrid opto-mechanical systems with nitrogen-vacancy centers*, Science China Physics, Mechanics & Astronomy **58**, 1 (2015).

[66] D. Lee, K. W. Lee, J. V. Cady, P. Ovartchaiyapong, and A. C. Bleszynski Jayich, *Topical review: Spins and mechanics in diamond*, Journal of Optics **19**, 033001 (2017).

[67] P. Ovartchaiyapong, L. M. A. Pascal, B. A. Myers, P. Lauria, and A. C. Bleszynski Jayich, *High quality factor single-crystal diamond mechanical resonators*, Applied Physics Letters **101**, 163505 (2012).

[68] Y. Tao, J. M. Boss, B. A. Moores, and C. L. Degen, *Single-crystal diamond nanomechanical resonators with quality factors exceeding one million*, Nature Communications **5**, 3638 (2014).
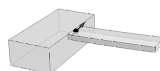
[69] A. Batalov, C. Zierl, T. Gaebel, P. Neumann, I.-Y. Chan, G. Balasubramanian, P. R. Hemmer, F. Jelezko, and J. Wrachtrup, *Temporal coherence of photons emitted by single Nitrogen-Vacancy defect centers in diamond using optical Rabi-oscillations*, Physical Review Letters **100**, 077401 (2008).

[70] L. Robledo, H. Bernien, T. van der Sar, and R. Hanson, *Spin dynamics in the optical cycle of single nitrogen-vacancy centres in diamond*, New Journal of Physics **13**, 025013 (2011).

[71] J. H. N. Loubser and J. A. van Wyk, *Electron spin resonance in the study of diamond*, Reports on Progress in Physics **41**, 1201 (1978).

[72] A. Gali, M. Fyta, and E. Kaxiras, *Ab initio supercell calculations on nitrogen-vacancy center in diamond: Electronic structure and hyperfine tensors*, Physical Review B **77**, 155206 (2008).

[73] Á. Gali, *Ab initio theory of the nitrogen-vacancy center in diamond*, Nanophotonics **8**, 1907 (2019).

[74] J. R. Maze, A. Gali, E. Togan, Y. Chu, A. Trifonov, E. Kaxiras, and M. D. Lukin, *Properties of nitrogen-vacancy centers in diamond: The group theoretic approach*, New Journal of Physics **13**, 025025 (2011).

[75] L. J. Rogers, R. L. McMurtrie, M. J. Sellars, and N. B. Manson, *Time-averaging within the excited state of the nitrogen-vacancy centre in diamond*, New Journal of Physics **11**, 063007 (2009).

[76] G. D. Fuchs, V. V. Dobrovitski, R. Hanson, A. Batra, C. D. Weis, T. Schenkel, and D. D. Awschalom, *Excited-state spectroscopy using single spin manipulation in diamond*, Physical Review Letters **101**, 117601 (2008).

[77] P. Neumann, R. Kolesov, V. Jacques, J. Beck, J. Tisler, A. Batalov, L. Rogers, N. B. Manson, G. Balasubramanian, F. Jelezko, and J. Wrachtrup, *Excited-state spectroscopy of single NV defects in diamond using optically detected magnetic resonance*, New Journal of Physics **11**, 013017 (2009).

[78] L. Du Preez, *Electron Paramagnetic Resonance and Optical Investigations of Defect Centre in Diamond*, Ph.D. thesis, University of Witwatersrand, Johannesburg (1965).

[79] G. Davies and M. F. Hamer, *Optical studies of the 1.945 eV vibronic band in diamond*, Proceedings of the Royal Society of London A: Mathematical, Physical and Engineering Sciences **348**, 285 (1976).

[80] L. J. Rogers, S. Armstrong, M. J. Sellars, and N. B. Manson, *Infrared emission of the NV centre in diamond: Zeeman and uniaxial stress studies*, New Journal of Physics **10**, 103024 (2008).

[81] L. Rondin, J.-P. Tetienne, T. Hingant, J.-F. Roch, P. Maletinsky, and V. Jacques, *Magnetometry with nitrogen-vacancy defects in diamond*, Reports on Progress in Physics **77**, 056503 (2014).

[82] M. W. Doherty, F. Dolde, H. Fedder, F. Jelezko, J. Wrachtrup, N. B. Manson, and L. C. L. Hollenberg, *Theory of the ground-state spin of the NV center in diamond*, Physical Review B **85**, 205203 (2012).

[83] X.-F. He, N. B. Manson, and P. T. H. Fisk, *Paramagnetic resonance of photoexcited N-V defects in diamond. II. Hyperfine interaction with the 14N nucleus*, Physical Review B **47**, 8816 (1993).

[84] M. Pfender, N. Aslam, P. Simon, D. Antonov, G. Thiering, S. Burk, F. Fávaro de Oliveira, A. Denisenko, H. Fedder, J. Meijer, J. A. Garrido, A. Gali, T. Teraji, J. Isoya, M. W. Doherty, A. Alkauskas, A. Gallo, A. Grüneis, P. Neumann, and J. Wrachtrup, *Protecting a diamond quantum memory by charge state control*, Nano Letters **17**, 5931 (2017).

[85] S. Felton, A. M. Edmonds, M. E. Newton, P. M. Martineau, D. Fisher, D. J. Twitchen, and J. M. Baker, *Hyperfine interaction in the ground state of the negatively charged nitrogen vacancy center in diamond*, Physical Review B **79**, 075203 (2009).

[86] V. V. Dobrovitski, A. E. Feiguin, D. D. Awschalom, and R. Hanson, *Decoherence dynamics of a single spin versus spin ensemble*, Physical Review B **77**, 245212 (2008).

[87] N. Bar-Gill, L. Pham, C. Belthangady, D. Le Sage, P. Cappellaro, J. Maze, M. Lukin, A. Yacoby, and R. Walsworth, *Suppression of spin-bath dynamics for improved coherence of multi-spin-qubit systems*, Nature Communications **3**, 858 (2012).

[88] B. Smeltzer, L. Childress, and A. Gali, *13C hyperfine interactions in the nitrogen-vacancy centre in diamond*, New Journal of Physics **13**, 025021 (2011).

[89] A. Dréau, J.-R. Maze, M. Lesik, J.-F. Roch, and V. Jacques, *High-resolution spectroscopy of single NV defects coupled with nearby 13C nuclear spins in diamond*, Physical Review B **85**, 134107 (2012).

[90] N. B. Manson, J. P. Harrison, and M. J. Sellars, *Nitrogen-vacancy center in diamond: Model of the electronic structure and associated dynamics*, Physical Review B **74**, 104303 (2006).

[91] G. Thiering and A. Gali, *Theory of the optical spin-polarization loop of the nitrogen-vacancy center in diamond*, Physical Review B **98**, 085207 (2018).

[92] M. L. Goldman, A. Sipahigil, M. W. Doherty, N. Y. Yao, S. D. Bennett, M. Markham, D. J. Twitchen, N. B. Manson, A. Kubanek, and M. D. Lukin, *Phonon-induced population dynamics and intersystem crossing in Nitrogen-Vacancy centers*, Physical Review Letters **114**, 145502 (2015).

[93] M. L. Goldman, M. W. Doherty, A. Sipahigil, N. Y. Yao, S. D. Bennett, N. B. Manson, A. Kubanek, and M. D. Lukin, *State-selective intersystem crossing in nitrogen-vacancy centers*, Physical Review B **91**, 165201 (2015).
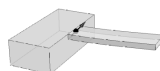
[94] V. M. Acosta, A. Jarmola, E. Bauch, and D. Budker, *Optical properties of the nitrogen-vacancy singlet levels in diamond*, Physical Review B **82**, 201202 (2010).

[95] B. J. Shields, Q. P. Unterreithmeier, N. P. de Leon, H. Park, and M. D. Lukin, *Efficient readout of a single spin state in diamond via spin-to-charge conversion*, Physical Review Letters **114**, 136402 (2015).

[96] J. M. Taylor, P. Cappellaro, L. Childress, L. Jiang, D. Budker, P. R. Hemmer, A. Yacoby, R. Walsworth, and M. D. Lukin, *High-sensitivity diamond magnetometer with nanoscale resolution*, Nature Physics **4**, 810 (2008).

[97] J. R. Maze, P. L. Stanwix, J. S. Hodges, S. Hong, J. M. Taylor, P. Cappellaro, L. Jiang, M. V. G. Dutt, E. Togan, A. S. Zibrov, A. Yacoby, R. L. Walsworth, and M. D. Lukin, *Nanoscale magnetic sensing with an individual electronic spin in diamond*, Nature **455**, 644 (2008).

[98] P. Maletinsky, S. Hong, M. S. Grinolds, B. Hausmann, M. D. Lukin, R. L. Walsworth, M. Lončar, and A. Yacoby, *A robust scanning diamond sensor for nanoscale imaging with single nitrogen-vacancy centres*, Nature Nanotechnology **7**, 320 (2012).

[99] T. Wolf, P. Neumann, K. Nakamura, H. Sumiya, T. Ohshima, J. Isoya, and J. Wrachtrup, *Subpicotesla diamond magnetometry*, Physical Review X **5**, 041001 (2015).

[100] F. Dolde, H. Fedder, M. W. Doherty, T. Nöbauer, F. Rempp, G. Balasubramanian, T. Wolf, F. Reinhard, L. C. L. Hollenberg, F. Jelezko, and J. Wrachtrup, *Electric-field sensing using single diamond spins*, Nature Physics **7**, 459 (2011).

[101] F. Dolde, M. W. Doherty, J. Michl, I. Jakobi, B. Naydenov, S. Pezzagna, J. Meijer, P. Neumann, F. Jelezko, N. B. Manson, and J. Wrachtrup, *Nanoscale detection of a single fundamental charge in ambient conditions using the NV- center in diamond*, Physical Review Letters **112**, 097603 (2014).

[102] P. Ovartchaiyapong, K. W. Lee, B. A. Myers, and A. C. Bleszynski Jayich, *Dynamic strain-mediated coupling of a single diamond spin to a mechanical resonator*, Nature Communications **5**, 4429 (2014).

[103] J. Teissier, A. Barfuss, P. Appel, E. Neu, and P. Maletinsky, *Strain coupling of a Nitrogen-Vacancy center spin to a diamond mechanical oscillator*, Physical Review Letters **113**, 020503 (2014).

[104] M. S. J. Barson, P. Peddibhotla, P. Ovartchaiyapong, K. Ganesan, R. L. Taylor, M. Gebert, Z. Mielens, B. Koslowski, D. A. Simpson, L. P. McGuinness, J. McCallum, S. Prawer, S. Onoda, T. Ohshima, A. C. Bleszynski Jayich, F. Jelezko, N. B. Manson, and M. W. Doherty, *Nanomechanical sensing using spins in diamond*, Nano Letters **17**, 1496 (2017).

[105] P. Udvarhelyi, V. O. Shkolnikov, A. Gali, G. Burkard, and A. Pályi, *Spin-strain interaction in nitrogen-vacancy centers in diamond*, Physical Review B **98**, 075201 (2018).

[106] A. Barfuss, M. Kasperczyk, J. Kölbl, and P. Maletinsky, *Spin-stress and spin-strain coupling in diamond-based hybrid spin oscillator systems*, Physical Review B **99**, 174102 (2019).

[107] V. M. Acosta, E. Bauch, M. P. Ledbetter, A. Waxman, L.-S. Bouchard, and D. Budker, *Temperature dependence of the nitrogen-vacancy magnetic resonance in diamond*, Physical Review Letters **104**, 070801 (2010).

[108] D. M. Toyli, C. F. de las Casas, D. J. Christle, V. V. Dobrovitski, and D. D. Awschalom, *Fluorescence thermometry enhanced by the quantum coherence of single spins in diamond*, Proceedings of the National Academy of Sciences **110**, 8417 (2013).

[109] P. Neumann, I. Jakobi, F. Dolde, C. Burk, R. Reuter, G. Waldherr, J. Honert, T. Wolf, A. Brunner, J. H. Shim, D. Suter, H. Sumiya, J. Isoya, and J. Wrachtrup, *High-precision nanoscale temperature sensing using single defects in diamond*, Nano Letters **13**, 2738 (2013).

[110] G. Kucsko, P. C. Maurer, N. Y. Yao, M. Kubo, H. J. Noh, P. K. Lo, H. Park, and M. D. Lukin, *Nanometre-scale thermometry in a living cell*, Nature **500**, 54 (2013).

[111] M. W. Doherty, N. B. Manson, P. Delaney, and L. C. L. Hollenberg, *The negatively charged nitrogen-vacancy centre in diamond: The electronic solution*, New Journal of Physics **13**, 025019 (2011).

[112] E. V. Oort and M. Glasbeek, *Electric-field-induced modulation of spin echoes of N-V centers in diamond*, Chemical Physics Letters **168**, 529 (1990).

[113] A. N. Cleland, *Foundations of Nanomechanics - from Solid-State Theory to Device Applications* (Springer, Berlin) (2003).

[114] A. Barfuss, *Hybrid Spin-Nanomechanics with Single Spins in Diamond Mechanical Oscillators*, Ph.D. thesis, University of Basel, Basel (2017).

[115] T. Mittiga, S. Hsieh, C. Zu, B. Kobrin, F. Machado, P. Bhattacharyya, N. Z. Rui, A. Jarmola, S. Choi, D. Budker, and N. Y. Yao, *Imaging the local charge environment of Nitrogen-Vacancy centers in diamond*, Physical Review Letters **121**, 246402 (2018).

[116] J. Kölbl, M. Kasperczyk, B. Bürgler, A. Barfuss, and P. Maletinsky, *Determination of intrinsic effective fields and microwave polarizations by high-resolution spectroscopy of single nitrogen-vacancy center spins*, New Journal of Physics **21**, 113039 (2019).

[117] L. Childress, M. V. Gurudev Dutt, J. M. Taylor, A. S. Zibrov, F. Jelezko, J. Wrachtrup, P. R. Hemmer, and M. D. Lukin, *Coherent dynamics of coupled electron and nuclear spin qubits in diamond*, Science **314**, 281 (2006).

[118] A. P. Nizovtsev, S. Y. Kilin, A. L. Pushkarchuk, V. A. Pushkarchuk, S. A. Kuten, O. A. Zhikol, S. Schmitt, T. Unden, and F. Jelezko, *Non-flipping 13C*
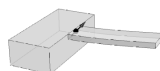
spins near an NV center in diamond: Hyperfine and spatial characteristics by density functional theory simulation of the C510[NV]H252cluster, New Journal of Physics **20**, 023022 (2018).

[119] O. Arcizet, V. Jacques, A. Siria, P. Poncharal, P. Vincent, and S. Seidelin, *A single nitrogen-vacancy defect coupled to a nanomechanical oscillator*, Nature Physics **7**, 879 (2011).

[120] S. Meesala, Y.-I. Sohn, H. A. Atikian, S. Kim, M. J. Burek, J. T. Choy, and M. Lončar, *Enhanced strain coupling of Nitrogen-Vacancy spins to nanoscale diamond cantilevers*, Physical Review Applied **5**, 034010 (2016).

[121] B. Saleh and M. Teich, *Fundamentals of Photonics* (Wiley, New York) (2007).

[122] A. Dréau, M. Lesik, L. Rondin, P. Spinicelli, O. Arcizet, J.-F. Roch, and V. Jacques, *Avoiding power broadening in optically detected magnetic resonance of single NV defects for enhanced dc magnetic field sensitivity*, Physical Review B **84**, 195204 (2011).

[123] E. L. Hahn, *Spin echoes*, Physical Review **80**, 580 (1950).

[124] H. Y. Carr and E. M. Purcell, *Effects of diffusion on free precession in nuclear magnetic resonance experiments*, Physical Review **94**, 630 (1954).

[125] S. R. Hartmann and E. L. Hahn, *Nuclear double resonance in the rotating frame*, Physical Review **128**, 2042 (1962).

[126] I. I. Rabi, *Space quantization in a gyrating magnetic field*, Physical Review **51**, 652 (1937).

[127] B. K. Ofori-Okai, S. Pezzagna, K. Chang, M. Loretz, R. Schirhagl, Y. Tao, B. A. Moores, K. Groot-Berning, J. Meijer, and C. L. Degen, *Spin properties of very shallow nitrogen vacancy defects in diamond*, Physical Review B **86**, 081406 (2012).

[128] J. R. Maze, A. Dréau, V. Waselowski, H. Duarte, J.-F. Roch, and V. Jacques, *Free induction decay of single spins in diamond*, New Journal of Physics **14**, 103041 (2012).

[129] T. Ishikawa, K.-M. C. Fu, C. Santori, V. M. Acosta, R. G. Beausoleil, H. Watanabe, S. Shikata, and K. M. Itoh, *Optical and spin coherence properties of Nitrogen-Vacancy centers placed in a 100 nm thick isotopically purified diamond layer*, Nano Letters **12**, 2083 (2012).

[130] P. C. Maurer, G. Kucsko, C. Latta, L. Jiang, N. Y. Yao, S. D. Bennett, F. Pastawski, D. Hunger, N. Chisholm, M. Markham, D. J. Twitchen, J. I. Cirac, and M. D. Lukin, *Room-temperature quantum bit memory exceeding one second*, Science **336**, 1283 (2012).

[131] B. A. Myers, A. Ariyaratne, and A. C. Bleszynski Jayich, *Double-quantum spin-relaxation limits to coherence of near-surface Nitrogen-Vacancy centers*, Physical Review Letters **118**, 197201 (2017).

[132] A. Jarmola, V. M. Acosta, K. Jensen, S. Chemerisov, and D. Budker, *Temperature- and magnetic-field-dependent longitudinal spin relaxation in Nitrogen-Vacancy ensembles in diamond*, Physical Review Letters **108**, 197601 (2012).

[133] E. R. MacQuarrie, T. A. Gosavi, N. R. Jungwirth, S. A. Bhave, and G. D. Fuchs, *Mechanical spin control of Nitrogen-Vacancy centers in diamond*, Physical Review Letters **111**, 227602 (2013).

[134] E. R. MacQuarrie, T. A. Gosavi, A. M. Moehle, N. R. Jungwirth, S. A. Bhave, and G. D. Fuchs, *Coherent control of a nitrogen-vacancy center spin ensemble with a diamond mechanical resonator*, Optica **2**, 233 (2015).

[135] K. Fang, V. M. Acosta, C. Santori, Z. Huang, K. M. Itoh, H. Watanabe, S. Shikata, and R. G. Beausoleil, *High-sensitivity magnetometry based on quantum beats in diamond Nitrogen-Vacancy centers*, Physical Review Letters **110**, 130802 (2013).

[136] H. J. Mamin, M. H. Sherwood, M. Kim, C. T. Rettner, K. Ohno, D. D. Awschalom, and D. Rugar, *Multipulse double-quantum magnetometry with near-surface Nitrogen-Vacancy centers*, Physical Review Letters **113**, 030803 (2014).

[137] K. Bergmann, H. Theuer, and B. W. Shore, *Coherent population transfer among quantum states of atoms and molecules*, Reviev of Modern Physics **70**, 1003 (1998).

[138] B. W. Shore, *Manipulating Quantum Structures Using Laser Pulses* (Cambridge University Press, Cambridge) (2011).

[139] S. J. Buckle, S. M. Barnett, P. L. Knight, M. A. Lauder, and D. T. Pegg, *Atomic interferometers*, Optica Acta: International Journal of Optics **33**, 1129 (1986).

[140] D. Kosachiov, B. Matisov, and Y. Rozhdestvensky, *Coherent population trapping: Sensitivity of an atomic system to the relative phase of exciting fields*, Optics Communications **85**, 209 (1991).

[141] L. Windholz, *Coherent population trapping in multi-level atomic systems*, Physica Scripta **2001**, 81 (2001).

[142] W. Maichen, R. Gaggl, E. Korsunsky, and L. Windholz, *Observation of phase-dependent coherent population trapping in optically closed atomic systems*, Europhysics Letters **31**, 189 (1995).

[143] K. Yamamoto, K. Ichimura, and N. Gemma, *Enhanced and reduced absorptions via quantum interference: Solid system driven by a rf field*, Physical Review A **58**, 2460 (1998).

[144] E. A. Korsunsky, N. Leinfellner, A. Huss, S. Baluschev, and L. Windholz, *Phase-dependent electromagnetically induced transparency*, Physical Review A **59**, 2302 (1999).
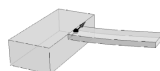
[145] H. Li, V. A. Sautenkov, Y. V. Rostovtsev, G. R. Welch, P. R. Hemmer, and M. O. Scully, *Electromagnetically induced transparency controlled by a microwave field*, Physical Review A **80**, 023820 (2009).

[146] T. M. Preethi, M. Manukumara, K. Asha, J. Vijay, D. A. Roshi, and A. Narayanan, *Phase-sensitive microwave optical double resonance in an N system*, EPL (Europhysics Letters) **95**, 34005 (2011).

[147] P. Roushan, C. Neill, A. Megrant, Y. Chen, R. Babbush, R. Barends, B. Campbell, Z. Chen, B. Chiaro, A. Dunsworth, A. Fowler, E. Jeffrey, J. Kelly, E. Lucero, J. Mutus, P. J. J. O'Malley, M. Neeley, C. Quintana, D. Sank, A. Vainsencher, J. Wenner, T. White, E. Kapit, H. Neven, and J. Martinis, *Chiral ground-state currents of interacting photons in a synthetic magnetic field*, Nature Physics **13**, 146 (2017).

[148] A. Barfuss, J. Kölbl, L. Thiel, J. Teissier, M. Kasperczyk, and P. Maletinsky, *Phase-controlled coherent dynamics of a single spin under closed-contour interaction*, Nature Physics **14**, 1087 (2018).

[149] Y. Chu, N. de Leon, B. Shields, B. Hausmann, R. Evans, E. Togan, M. J. Burek, M. Markham, A. Stacey, A. Zibrov, A. Yacoby, D. Twitchen, M. Lončar, H. Park, P. Maletinsky, and M. Lukin, *Coherent optical transitions in implanted Nitrogen Vacancy centers*, Nano Letters **14**, 1982 (2014).

[150] J. F. Ziegler, M. D. Ziegler, and J. P. Biersack, *SRIM – The stopping and range of ions in matter*, Nuclear Instruments and Methods in Physics Research Section B: Beam Interactions with Materials and Atoms **268**, 1818 (2010).

[151] P. Appel, E. Neu, M. Ganzhorn, A. Barfuss, M. Batzer, M. Gratz, A. Tschöpe, and P. Maletinsky, *Fabrication of all diamond scanning probes for nanoscale magnetometry*, Review of Scientific Instruments **87**, 063703 (2016).

[152] M. Minsky, *Memoir on inventing the confocal scanning microscope*, Scanning **10**, 128 (1988).

[153] D. Pegg, *Two-photon resonance with combined amplitude and frequency modulation*, Optics Communications **57**, 185 (1986).

[154] E. R. MacQuarrie, T. A. Gosavi, S. A. Bhave, and G. D. Fuchs, *Continuous dynamical decoupling of a single diamond nitrogen-vacancy center spin with a mechanical resonator*, Physical Review B **92**, 224419 (2015).

[155] A. Stark, N. Aharon, A. Huck, H. A. R. El-Ella, A. Retzker, F. Jelezko, and U. L. Andersen, *Clock transition by continuous dynamical decoupling of a three-level system*, Scientific Reports **8**, 1 (2018).

[156] T. Joas, A. M. Waeber, G. Braunbeck, and F. Reinhard, *Quantum sensing of weak radio-frequency signals by pulsed Mollow absorption spectroscopy*, Nature Communications **8**, 1 (2017).

[157] K. Fang, J. Luo, A. Metelmann, M. H. Matheny, F. Marquardt, A. A. Clerk, and O. Painter, *Generalized non-reciprocity in an optomechanical circuit via synthetic magnetism and reservoir engineering*, Nature Physics **13**, 465 (2017).

[158] M. H. Abobeih, J. Cramer, M. A. Bakker, N. Kalb, M. Markham, D. J. Twitchen, and T. H. Taminiau, *One-second coherence for a single electron spin coupled to a multi-qubit nuclear-spin environment*, Nature Communications **9**, 1 (2018).

[159] Y.-X. Du, B.-J. Liu, Q.-X. Lv, X.-D. Zhang, H. Yan, and S.-L. Zhu, *Degenerate eigensubspace in a triangle-level system and its geometric quantum control*, Physical Review A **96**, 012333 (2017).

[160] C. L. Degen, F. Reinhard, and P. Cappellaro, *Quantum sensing*, Reviews of Modern Physics **89**, 035002 (2017).

[161] D. Loss and D. P. DiVincenzo, *Quantum computation with quantum dots*, Physical Review A **57**, 120 (1998).

[162] B. E. Kane, *A silicon-based nuclear spin quantum computer*, Nature **393**, 133 (1998).

[163] M. Nielsen and I. Chuang, *Quantum Computation and Quantum Information* (Cambridge University Press, Cambridge) (2010).

[164] T. D. Ladd, F. Jelezko, R. Laflamme, Y. Nakamura, C. Monroe, and J. L. O'Brien, *Quantum computers*, Nature **464**, 45 (2010).

[165] T. van der Sar, Z. H. Wang, M. S. Blok, H. Bernien, T. H. Taminiau, D. M. Toyli, D. A. Lidar, D. D. Awschalom, R. Hanson, and V. V. Dobrovitski, *Decoherence-protected quantum gates for a hybrid solid-state spin register*, Nature **484**, 82 (2012).

[166] C. M. Wilson, T. Duty, F. Persson, M. Sandberg, G. Johansson, and P. Delsing, *Coherence times of dressed states superconducting qubit under extreme driving*, Physical Review Letters **98**, 257003 (2007).

[167] P. London, J. Scheuer, J.-M. Cai, I. Schwarz, A. Retzker, M. B. Plenio, M. Katagiri, T. Teraji, S. Koizumi, J. Isoya, R. Fischer, L. P. McGuinness, B. Naydenov, and F. Jelezko, *Detecting and polarizing nuclear spins with double resonance on a single electron spin*, Physical Review Letters **111**, 067601 (2013).

[168] M. Demirplak and S. A. Rice, *Adiabatic population transfer with control fields*, The Journal of Physical Chemistry A **107**, 9937 (2003).

[169] M. V. Berry, *Transitionless quantum driving*, Journal of Physics A: Mathematical and Theoretical **42**, 365303 (2009).

[170] X. Chen, I. Lizuain, A. Ruschhaupt, D. Guéry-Odelin, and J. G. Muga, *Shortcut to adiabatic passage in two- and three level atoms*, Physical Review Letters **105**, 123003 (2010).
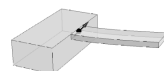
[171] A. del Campo, *Shortcuts to adiabaticity by counterdiabatic driving*, Physical Review Letters **111**, 100502 (2013).

[172] E. Torrontegui, S. Ibáñez, S. Martínez-Garaot, M. Modugno, A. del Campo, D. Guéry-Odelin, A. Ruschhaupt, X. Chen, and J. G. Muga, *Chapter 2 - Shortcuts to adiabaticity*, in E. Arimondo, P. R. Berman, and C. C. Lin (editors), *Advances in Atomic, Molecular, and Optical Physics*, *Advances in Atomic, Molecular, and Optical Physics*, volume 62, pp. 117–169 (Academic Press) (2013).

[173] D. Guéry-Odelin, A. Ruschhaupt, A. Kiely, E. Torrontegui, S. Martínez-Garaot, and J. G. Muga, *Shortcuts to adiabaticity: Concepts, methods, and applications*, Reviews of Modern Physics **91**, 045001 (2019).

[174] Z.-T. Liang, X. Yue, Q. Lv, Y.-X. Du, W. Huang, H. Yan, and S.-L. Zhu, *Proposal for implementing universal superadiabatic geometric quantum gates in nitrogen-vacancy centers*, Physical Review A **93**, 040305 (2016).

[175] X.-K. Song, H. Zhang, Q. Ai, J. Qiu, and F.-G. Deng, *Shortcuts to adiabatic holonomic quantum computation in decoherence-free subspace with transitionless quantum driving algorithm*, New Journal of Physics **18**, 023001 (2016).

[176] B.-J. Liu, X.-K. Song, Z.-Y. Xue, X. Wang, and M.-H. Yung, *Plug-and-play approach to nonadiabatic geometric quantum gates*, Physical Review Letters **123**, 100501 (2019).

[177] J. Tian, T. Du, Y. Liu, H. Liu, F. Jin, R. S. Said, and J. Cai, *Optimal quantum optical control of spin in diamond*, Physical Review A **100**, 012110 (2019).

[178] S.-H. Wu, M. Amezcua, and H. Wang, *Adiabatic population transfer of dressed spin states with quantum optimal control*, Physical Review A **99**, 063812 (2019).

[179] J. Zhang, J. H. Shim, I. Niemeyer, T. Taniguchi, T. Teraji, H. Abe, S. Onoda, T. Yamamoto, T. Ohshima, J. Isoya, and D. Suter, *Experimental implementation of assisted quantum adiabatic passage in a single spin*, Physical Review Letters **110**, 240501 (2013).

[180] B. B. Zhou, A. Baksic, H. Ribeiro, C. G. Yale, F. J. Heremans, P. C. Jerger, A. Auer, G. Burkard, A. A. Clerk, and D. D. Awschalom, *Accelerated quantum control using superadiabatic dynamics in a solid-state lambda system*, Nature Physics **13**, 330 (2016).

[181] F. Kleißler, A. Lazariev, and S. Arroyo-Camejo, *Universal, high-fidelity quantum gates based on superadiabatic, geometric phases on a solid-state spin-qubit at room temperature*, npj Quantum Information **4**, 1 (2018).

[182] E. Boyers, M. Pandey, D. K. Campbell, A. Polkovnikov, D. Sels, and A. O. Sushkov, *Floquet-engineered quantum state manipulation in a noisy qubit*, Physical Review A **100**, 012341 (2019).

[183] J. Kölbl, A. Barfuss, M. S. Kasperczyk, L. Thiel, A. A. Clerk, H. Ribeiro, and P. Maletinsky, *Initialization of single spin dressed states using shortcuts to ddiabaticity*, Physical Review Letters **122**, 090502 (2019).

[184] S. Shevchenko, S. Ashhab, and F. Nori, *Landau-Zener-Stückelberg interferometry*, Physics Reports **492**, 1 (2010).

[185] A. Baksic, H. Ribeiro, and A. A. Clerk, *Speeding up adiabatic quantum state transfer by using dressed states*, Physical Review Letters **116**, 230503 (2016).

[186] G. S. Vasilev, A. Kuhn, and N. V. Vitanov, *Optimum pulse shapes for stimulated Raman adiabatic passage*, Physical Review A **80**, 013417 (2009).

[187] M. Demirplak and S. A. Rice, *Assisted adiabatic passage revisited*, The Journal of Physical Chemistry B **109**, 6838 (2005).

[188] C. Simon, M. Afzelius, J. Appel, A. Boyer de la Giroday, S. J. Dewhurst, N. Gisin, C. Y. Hu, F. Jelezko, S. Kröll, J. H. Müller, J. Nunn, E. S. Polzik, J. G. Rarity, H. De Riedmatten, W. Rosenfeld, A. J. Shields, N. Sköld, R. M. Stevenson, R. Thew, I. A. Walmsley, M. C. Weber, H. Weinfurter, J. Wrachtrup, and R. J. Young, *Quantum memories*, The European Physical Journal D **58**, 1 (2010).

[189] G. D. Fuchs, G. Burkard, P. V. Klimov, and D. D. Awschalom, *A quantum memory intrinsic to single nitrogen–vacancy centres in diamond*, Nature Physics **7**, 789 (2011).

[190] H. P. Specht, C. Nölleke, A. Reiserer, M. Uphoff, E. Figueroa, S. Ritter, and G. Rempe, *A single-atom quantum memory*, Nature **473**, 190 (2011).

[191] N. V. Vitanov and M. Drewsen, *Highly efficient detection and separation of chiral molecules through shortcuts to adiabaticity*, Physical Review Letters **122**, 173202 (2019).

[192] M. J. Burek, J. D. Cohen, S. M. Meenehan, N. El-Sawah, C. Chia, T. Ruelle, S. Meesala, J. Rochman, H. A. Atikian, M. Markham, D. J. Twitchen, M. D. Lukin, O. Painter, and M. Lončar, *Diamond optomechanical crystals*, Optica **3**, 1404 (2016).

[193] M. Mitchell, B. Khanaliloo, D. P. Lake, T. Masuda, J. P. Hadden, and P. E. Barclay, *Single-crystal diamond low-dissipation cavity optomechanics*, Optica **3**, 963 (2016).

[194] J. V. Cady, O. Michel, K. W. Lee, R. N. Patel, C. J. Sarabalis, A. H. Safavi-Naeini, and A. C. B. Jayich, *Diamond optomechanical crystals with embedded nitrogen-vacancy centers*, Quantum Science and Technology **4**, 024009 (2019).

[195] D. A. Golter, T. Oo, M. Amezcua, K. A. Stewart, and H. Wang, *Optomechanical quantum control of a Nitrogen-Vacancy center in diamond*, Physical Review Letters **116**, 143602 (2016).

[196] H. Y. Chen, E. R. MacQuarrie, and G. D. Fuchs, *Orbital state manipulation of a diamond Nitrogen-Vacancy center using a mechanical resonator*, Physical Review Letters **120**, 167401 (2018).
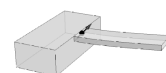
[197] H. Chen, N. F. Opondo, B. Jiang, E. R. MacQuarrie, R. S. Daveau, S. A. Bhave, and G. D. Fuchs, *Engineering electron–phonon coupling of quantum defects to a semiconfocal acoustic resonator*, Nano Letters **19**, 7021 (2019).

[198] D. P. DiVincenzo, *The physical implementation of quantum computation*, Fortschritte der Physik **48**, 771 (2000).

[199] D. P. Weitekamp, A. Bielecki, D. Zax, K. Zilm, and A. Pines, *Zero-field nuclear magnetic resonance*, Physical Review Letters **50**, 1807 (1983).

[200] A. M. Thayer and A. Pines, *Zero-field NMR*, Accounts of Chemical Research **20**, 47 (1987).

[201] H. Zheng, J. Xu, G. Z. Iwata, T. Lenz, J. Michl, B. Yavkin, K. Nakamura, H. Sumiya, T. Ohshima, J. Isoya, J. Wrachtrup, A. Wickenbrock, and D. Budker, *Zero-field magnetometry based on Nitrogen-Vacancy ensembles in diamond*, Physical Review Applied **11**, 064068 (2019).

[202] M. W. Doherty, J. Michl, F. Dolde, I. Jakobi, P. Neumann, N. B. Manson, and J. Wrachtrup, *Measuring the defect structure orientation of a single NV- centre in diamond*, New Journal of Physics **16**, 063067 (2014).

[203] J.-P. Tetienne, T. Hingant, J.-V. Kim, L. H. Diez, J.-P. Adam, K. Garcia, J.-F. Roch, S. Rohart, A. Thiaville, D. Ravelosona, and V. Jacques, *Nanoscale imaging and control of domain-wall hopping with a nitrogen-vacancy center microscope*, Science **344**, 1366 (2014).

[204] M. Jiang, R. P. Frutos, T. Wu, J. W. Blanchard, X. Peng, and D. Budker, *Magnetic gradiometer for the detection of zero- to ultralow-field nuclear magnetic resonance*, Physical Review Applied **11**, 024005 (2019).

[205] P. Appel, M. Ganzhorn, E. Neu, and P. Maletinsky, *Nanoscale microwave imaging with a single electron spin in diamond*, New Journal of Physics **17**, 112001 (2015).

[206] A. Horsley, P. Appel, J. Wolters, J. Achard, A. Tallaire, P. Maletinsky, and P. Treutlein, *Microwave device characterization using a widefield diamond microscope*, Physical Review Applied **10**, 044039 (2018).

[207] P. Wang, Z. Yuan, P. Huang, X. Rong, M. Wang, X. Xu, C. Duan, C. Ju, F. Shi, and J. Du, *High-resolution vector microwave magnetometry based on solid-state spins in diamond*, Nature Communications **6**, 6631 (2015).

[208] B. T. Rosner and D. W. van der Weide, *High-frequency near-field microscopy*, Review of Scientific Instruments **73**, 2505 (2002).

[209] P. Andrich, C. F. de las Casas, X. Liu, H. L. Bretscher, J. R. Berman, F. J. Heremans, P. F. Nealey, and D. D. Awschalom, *Long-range spin wave mediated control of defect qubits in nanodiamonds*, npj Quantum Information **3**, 1 (2017).

[210] C. Zu, W.-B. Wang, L. He, W.-G. Zhang, C.-Y. Dai, F. Wang, and L.-M. Duan, *Experimental realization of universal geometric quantum gates with solid-state spins*, Nature **514**, 72 (2014).

[211] A. Roulet and C. Bruder, *Synchronizing the smallest possible system*, Physical Review Letters **121**, 053601 (2018).

[212] A. W. Laskar, P. Adhikary, S. Mondal, P. Katiyar, S. Vinjanampathy, and S. Ghosh, *Observation of quantum phase synchronization in spin-1 atoms*, arXiv **1910.11832**, 1 (2019).

[213] S. D. Bennett, N. Y. Yao, J. Otterbach, P. Zoller, P. Rabl, and M. D. Lukin, *Phonon-induced spin-spin interactions in diamond nanostructures: Application to spin squeezing*, Physical Review Letters **110**, 156402 (2013).

[214] I. Wilson-Rae, P. Zoller, and A. Imamoglu, *Laser cooling of a nanomechanical resonator mode to its quantum ground state*, Physical Review Letters **92**, 075507 (2004).

[215] K. V. Kepesidis, S. D. Bennett, S. Portolan, M. D. Lukin, and P. Rabl, *Phonon cooling and lasing with nitrogen-vacancy centers in diamond*, Physical Review B **88**, 064105 (2013).

[216] E. R. MacQuarrie, M. Otten, S. K. Gray, and G. D. Fuchs, *Cooling a mechanical resonator with nitrogen-vacancy centres using a room temperature excited state spin-strain interaction*, Nature Communications **8**, 14358 (2017).

[217] P. Rabl, S. J. Kolkowitz, F. H. L. Koppens, J. G. E. Harris, P. Zoller, and M. D. Lukin, *A quantum spin transducer based on nanoelectromechanical resonator arrays*, Nature Physics **6**, 602 (2010).

[218] K. W. Lee, D. Lee, P. Ovartchaiyapong, J. Minguzzi, J. R. Maze, and A. C. Bleszynski Jayich, *Strain coupling of a mechanical resonator to a single quantum emitter in diamond*, Physical Review Applied **6**, 034005 (2016).

[219] L. Thiel, D. Rohner, M. Ganzhorn, P. Appel, E. Neu, B. Müller, R. Kleiner, D. Koelle, and P. Maletinsky, *Quantitative nanoscale vortex imaging using a cryogenic quantum magnetometer*, Nature Nanotechnology **11**, 677 (2016).

[220] P. Jamonneau, M. Lesik, J. P. Tetienne, I. Alvizu, L. Mayer, A. Dréau, S. Kosen, J.-F. Roch, S. Pezzagna, J. Meijer, T. Teraji, Y. Kubo, P. Bertet, J. R. Maze, and V. Jacques, *Competition between electric field and magnetic field noise in the decoherence of a single spin in diamond*, Physical Review B **93**, 024305 (2016).
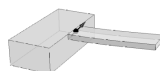
Acknowledgement

Although I had to write my PhD thesis on my own, many people contributed to its success. At this point, I would like to express my gratitude to all of them.

Foremost I am deeply indebted to my PhD supervisor. Dear Patrick, thank you very much for giving me the chance to make my PhD in your group. Even if the four years were characterized by ups and downs, it was an unforgettable and very exciting time. You always gave me your tireless support and supervision, especially during the difficult phases. Your fascination in physics in combination with your irrepressible motivation has managed time and time again to awake enthusiasm for my work. It was a pleasure to work for and with you! Thank you for the wonderful time with you and your group!

I also owe special thanks to my second supervisor, Guido Burkard. Thanks for your willingness to (once more) take over the expert opinion on my work. From your personal experience, you know that a PhD in Basel is an attractive opportunity, although leaving Konstanz was not easy.

Several people have worked closely with me and deserve my special gratitude, in particular Arne, Mark, and Lucas. Dear Arne, I am unlimited thankful for all the things you taught me during our time together. You always were on hand with help and advice for me and my PhD would not have been so successful without you. Dear Mark, your support was not just work-related – thanks for sometimes taking over the optics-related tasks, your theoretical calculations and simulations, and your endless corrections on my writing – it went far beyond that, including your motivation in difficult situations and your special empathy. Dear Lucas, you had a major impact on my work, too. Not only in terms of your software skills that ultimately made the experiments possible but also your cheerful, encouraging character made everyday life in the office easier. I further appreciated our numerous private conversations. A 'little' thanks also to you, dear Märta, for always spreading happiness and a good mood when entering the office. I also yield Alex, Brendan, David, Jodok, Marcel.li, and Tomek thanks for their feedback on my thesis and all the other members of the quantum sensing group for the great group atmosphere. Finally, I want to thank Michael Steinacher for his help in my numerous electronic questions and all the support of the department's administrative and technical staff.

Outside the university, Susanne and Konstantin had a crucial, though inconspicuous contribution to the success. Thanks both of you for your open ear, your always honest opinion, and for being real friends. Last but not least, my family deserves a special thank-you for the inexhaustible support they gave me all the while!
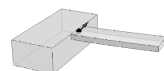
Curriculum Vitae

Personal Details

Name	Johannes Kölbl
Date of Birth	20 of May 1991
Place of Birth	Memmingen, Germany
Email	johannes.koelbl@unibas.ch

Education

2016 – 2020	University of Basel, PhD in Experimental Physics
2013 – 2015	University of Konstanz, Master of Science in Physics
	Master thesis in the group of Prof. E. M. Weig
	Kohärente Dynamik von gekoppelten nanomechanischen Resonatormoden
2010 – 2013	University of Konstanz, Bachelor of Science in Physics
	Bachelor thesis in the group of Prof. G. Burkard
	Kopplung von Spin- und Valleyfreiheitsgraden an einen nanomechanischen Resonator
2001 – 2010	Allgäu Gymnasium Kempten, Abitur

Publications

[221] J. Kölbl, M. S. Kaspercyzk, B. Bürgler, A. Barfuss P. Maletinsky, *Determination of intrinsic effective fields and microwave polarizations by high-resolution spectroscopy of single NV center spins*, New Journal of Physics **21**, 113039 (2019)

[222] J. S. Huber, G. Rastelli, M. J. Seitner, J. Kölbl, W. Belzig, M. I. Dykman, E. M. Weig, *Detecting squeezing from the fluctuation spectrum of a driven nanomechanical mode*, arXiv **1903.07601**, 1 (2019)

[223] J. Kölbl, A. Barfuss, M. S. Kaspercyzk, L. Thiel, A. A. Clerk, H. Ribeiro, P. Maletinsky, *Initialization of single spin dressed states using shortcuts to adiabaticity*, Physical Review Letters **122**, 090502 (2019)

[224] A. Barfuss, M. S. Kaspercyzk, J. Kölbl, P. Maletinsky, *Spin-stress and spin-strain coupling in diamond-based hybrid spin oscillator systems*, Physical Review B **99**, 174102 (2019)
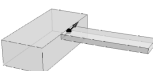
[225] A. Barfuss, J. Kölbl, L. Thiel, J. Teissier, M. S. Kaspercyzk, P. Maletinsky, *Phase-controlled coherent dynamics of a single spin under closed-contour interaction*, Nature Physics **14**, 1087 (2018)

[226] M. Challier, S. Sonusen, A. Barfuss, D. Rohner, D. Riedel, J. Kölbl, M. Ganzhorn, P. Appel, P. Maletinsky, E. Neu, *Advanced fabrication of single-crystal diamond membranes for quantum technologies*, Micromachines **9**, 148 (2017)

[227] M. J. Seitner, H. Ribeiro, J. Kölbl, T. Faust, E. M. Weig, *Finite-time Stückelberg interferometry with nanomechanical modes*, New Journal of Physics **19**, 033011 (2017)

[228] M. J. Seitner, H. Ribeiro, J. Kölbl, T. Faust, J. P. Kotthaus, E. M. Weig, *Classical Stueckelberg interferometry of a nanomechanical two-mode system*, Physical Review B **94**, 245406 (2016)

April 1, 2020